The Effect of Residual Stress Induced by Cold Spray Coating on Fatigue Life of Magnesium Alloy, AZ31B

by

Hassan Mahmoudi-Asl

A thesis
presented to the University of Waterloo
in fulfillment of the
thesis requirement for the degree of
Master of Applied Science
in
Mechanical Engineering

Waterloo, Ontario, Canada, 2011

AUTHOR'S DECLARATION

I hereby declare that I am the sole author of this thesis. This is a true copy of the thesis, including any required final revisions, as accepted by my examiners.

I understand that my thesis may be made electronically available to the public.

Abstract

Wrought magnesium alloys are considered attractive candidates for structural members in automotive and aerospace industries due to their high specific strength. Although new processes have helped to produce high purity magnesium alloys with higher resistance to corrosion, these alloys still need protection against corrosion when they are used in aggressive environments. Cold spray coating is one of the protective methods that are employed for this purpose. The similarity between cold spray coating and shot peening process poses the question whether cold spray coating can improve the fatigue strength in addition to providing corrosion protection. The objective of this research is to answer this question for the specific case of the coating of wrought magnesium alloy AZ31B with aluminum powder. This study comprises two parts. The first part characterises the residual stress induced by cold spray coating. This investigation employs both numerical and experimental methods. For the numerical study, the cold spray coating process has been simulated via ANSYS software classic package. The numerical results have been compared to experimental results from X-Ray Diffraction (XRD) stress measurement of a coated sample. For the second part of this research, the fatigue strength of as received, stress relieved, and stress relieved/coated specimens have been compared. Three groups of AZ31B specimens have been prepared and tested by rotating bending machine and their S-N curves have been prepared. Comparison of the results reveals that there is a considerable loss in fatigue strength of as received specimens after stress relief. This is due to the removal of compressive residual stress in the raw material induced by the extrusion process. Also, comparison of S-N curves of stress relieved and stress relieved/coated specimens shows fatigue life improvement after cold spray coating. The maximum improvement is 49 percent in the load of 120 MPa and the endurance limit has improved 9 percent.

Acknowledgements

It is a pleasure to thank those who helped me on this research. First of all, I would like to express my sincere gratitude to my supervisor Professor Hamid Jahed for his patience, great supports and helpful advices.

The financial support of Initiative for Automotive Manufacturing Innovation (IAMI) is gratefully acknowledged.

I would also like to express my sincere gratitude to CenterLine Ltd. and in particular Dr. Julio Villafuerte and Dr. Jianfeng Wang for providing technical support during this research.

I wish to offer my sincere thanks to my friends Behzad Behravesh, Jafar Albinmousa, Ramin Ghelichi and Dr. Amin Eshraghi who helped me with my work.

I would also like to express my sincere thanks to Zeinab Jahed who helped on preparing SEM images of the fracture surfaces.

I also wish to thank Ted Vinieris who offered his valuable help on proofreading this thesis.

Special thanks to my friend Zohreh for her kind supports and advices during my studies and this research.

Finally, I would like to express my extreme gratitude to my family for their support and encouragement through my studies.

Dedication

To my parents who gave me life and love

Table of Contents

AUTHOR'S DECLARATION ii

Abstract iii

Acknowledgements iv

Dedication v

List of Figures viii

List of Tables xii

Chapter 1 Introduction 1

Chapter 2 Background and Literature review 4

- 2.1 Magnesium Alloys 4
  - 2.1.1 Magnesium Alloys Characteristics and Applications 4
  - 2.1.2 Casting Alloys 6
  - 2.1.3 Wrought Alloys 6
  - 2.1.4 Mechanical Properties 7
  - 2.1.5 AZ Wrought Alloys 8
  - 2.1.6 AZ31B Mechanical Properties 9
  - 2.1.7 Corrosion Resistance of Magnesium Alloys 10
- 2.2 Cold Gas Spray Coating Process 13
  - 2.2.1 Cold Spray Process 13
  - 2.2.2 Research Trends 15
- 2.3 Evaluation of Residual Stress Induced by Cold Spray Coating 18
- 2.4 Residual Stress Induced by Cold Spray Coating and Fatigue Life 26
  - 2.4.1 Shot Peening and Fatigue Performance 26
  - 2.4.2 Cold Spray Coating and Fatigue Performance 33

Chapter 3 Residual Stress Evaluation 36

- 3.1 Simulation of the Residual Stress Induced by Cold Spray Coating 36
  - 3.1.1 Selection of FEA Software 36
  - 3.1.2 Material Model 38
  - 3.1.3 Simulation Models and Solution Parameters 45
  - 3.1.4 Simulation Results 51

3.1.4.1 Single Particle Simulation Results 52
3.1.4.2 Multiple Particle Simulation Results 57
3.1.5 Effect of Material Properties and Velocity of Particles on Residual Stress 62
3.2 Stress Measurement Using X-Ray Diffraction (XRD) 64
Chapter 4 Effect of Cold Spray Coating on Fatigue Strength 69
4.1 Test Specimens 69
4.2 Rotating Bending Machine 72
4.3 Fatigue Tests 73
4.3.1 As Received Specimens 73
4.3.2 Stress Relieved Specimens 73
4.3.3 Stress Relieved/Coated Specimens 73
4.3.4 Test Results 73
4.3.5 Fracture Surfaces 75
4.3.6 Test Conclusions 80
Chapter 5 Conclusion 82
5.1 Residual Stress Evaluation 82
5.2 Effect of Cold Spray Coating on Fatigue Strength 84
Chapter 6 Future Work 85
6.1 FEA Simulation Studies 85
6.2 Experimental Studies 86
References 87

List of Figures

Figure 1 Densities and Specific Strengths of Selected Materials…………………..……….5

Figure 2 Elongation and Tensile Strength of Magnesium Casting and Wrought Alloys……7

Figure 3 Elongation and Tensile Strength of Wrought Magnesium Alloys……………...….8

Figure 4 AZ31B Extrusion Used for Experiments. All Dimensions In mm……………..….9

Figure 5 Monotonic Tensile, Compressive and Shear Behaviour of AZ31B Extrusion…...10

Figure 6 Corrosion Tests on Magnesium Die-Casting Alloys……………………….....….11

Figure 7 Comparison of Different Alloying Elements On Corrosion of Magnesium Alloys…….……………………………………………………………………12

Figure 8 Schematic of a Typical Cold-Spray System……………………………………...13

Figure 9 Morphology of Different Feedstock Powders; a)Al-10Sn, b)Al-20Sn, c)Copper and d)Titanium……………………….…………………………………………14

Figure 10 Scanning Electron Micrographs (Secondary Electron Mode) of Wipe Test Samples of Copper Particles on a Copper Substrate………………………………….….…14

Figure 11 Comparison of Two Copper Coatings Produced From the Same Feedstock Powder……………………………………………………………………...15

Figure 12 Subsurface Fatigue Crack Nucleation; a) Rotating Bending Specimen, Titanium Alloy b) Schematic of Residual Stress Distribution and Crack Nucleation Point...19

Figure 13 (a) Gas Velocity Contour Plot of the Helium Gas Jet, and (b) FEM Calculated Stresses Contours……………………………………...……………………23

Figure 14 Residual Stress Before and After Cold Spray Coating of Aluminum Powder on Aluminum Substrate……………………………………………………………..24

Figure 15 Comparison of Residual Stress Distributions of Gas Atomized and Direct Reduction Copper Powders ………………………………….………………25

Figure 16 S-N Curves of AZ31hp, AZ61hp and AlMgSi1..27

Figure 17 Induced Residual Stress by Shot Peening in AZ80 in Different Almen Intensities Ranging from 0.04 mmN to 0.4 mmN……………………………..27

Figure 18 S-N Curves of Original Electro Polished (EP) and Shot Peened (SP) Specimens of AZ80…………………………………………………………………………..28

Figure 19 Influence of Almen Intensity on Fatigue Performance of Al2024 and AZ31…....28

Figure 20 Influence of Surface Removal on Fatigue Performance of Heavily Peened Specimens of AL2024 and AZ80……….……………………………………….….29
Figure 21 Response of Fatigue Life to Almen Intensity in AZ80...29
Figure 22 Crack Growth Rate for Electro Polished and Shot Peened AZ80………………..30
Figure 23 Effect of Shot Peening and Roller Burnishing on Fatigue S-N Curve of AZ80…30
Figure 24 Residual Stress Distribution of Shot Peened AZ31 for Different Shot Peening Treatments…………………………………………………………………..31
Figure 25 Stress Relaxation in Bending Fatigue Test of AlZn4.5Mg1 and AZ31………….32
Figure 26 Fatigue Performance of Corroded and Uncorroded Shot Peened Specimens of AZ91 hp...33
Figure 27 High Cycle Fatigue Performance of Coated and Uncoated A356……………..…34
Figure 28 Fatigue Performance of the Bare, Alclad, and Cold sprayed Al-13Co-26Ce Coating on AA 2024-T3 Specimens……………………………………..…35
Figure 29 Linear Orthotropic Material Properties of AZ31B………………………………38
Figure 30 Material Constants of ANSYS Anisotropic Material Models………………….…..39
Figure 31 Extrusion Piece (left) and Compression Test Specimen Compression Test Specimen, AZ31, THD……………………………………………………….40
Figure 32 Compression Test Result, AZ31, THD……………………………….….….40
Figure 33 Torsion Specimen, AZ31, TD………………………………..…….………….41
Figure 34 Torsion Test Result, AZ31, TD………………………………………………..41
Figure 35 Plastic Anisotropic Material Parameters………………………………………43
Figure 36 Model Used for Material Model Verification (All Values in Pa)………………..43
Figure 37 Comparison of Material Properties and FEA Results, Uniaxial Tensile Load for a) TD, b) ED………………………… ……………………………………….44
Figure 38 A Quarter of Single Particle Model……………………………………...………46
Figure 39 A Quarter of Thirteen Particle Model……………………………………………47
Figure 40 A Quarter of Forty One Particle Model……………………………….….…….48
Figure 41 Forty One Particle Model with Five Group of Particles in Different Layers…….48
Figure 42 Level Difference of the Particle Layers Equals to Particle Diameter………...…49
Figure 43 Dissipation of Stress Wave through Time Measured for One Element……….....50
Figure 44 Residual Stress Distribution in a Shot Peened Specimen……………..……….51

Figure 45 Residual Stress SX, ED, Single Particle……………………………………….………52
Figure 46 Residual Stress SZ, TD, Single Particle………………………………….…………53
Figure 47 Top View of Measurement Paths…………………………..…………….……54
Figure 48 SX and SZ Under Impact Point, Point A…………………………......……54
Figure 49 SX and SZ at Path Passing Through Point B, X= 8 µm, Z=0………………...…55
Figure 50 SX and SZ at Path Passing Through Point C, X= 0, Z=8 µm……………………55
Figure 51 SX and SZ at Path Passing Through Point D, X= 8 µm, Z=8 µm……………..…56
Figure 52 SX and SZ Residual Stress Through Depth by Calculating the Average, Single Particle …………………………………………………………………….57
Figure 53 SX and SZ in the Centre of the Model, 13 Particle Model...................................58
Figure 54 Average SX and SZ on 50µmx50µm Area Through Depth, 13 Particle Model…59
Figure 55 Average SX and SZ on 25µmx25µm Area Through Depth, 13 Particle Model…59
Figure 56 SX and SZ in the Centre of the Model, 41 Particle Model……..……………..…60
Figure 57 Average SX and SZ on 100µmx100µm Area Through Depth, 41 Particle Model ……………………………………………………………………………..…60
Figure 58 Average SX and SZ on 50µmx50µm Area Through Depth, 41 Particle Model....61
Figure 59 Effect of Particle Material Properties on Induced Residual Stress, SX……….….62
Figure 60 Effect of Particle Material Properties on Induced Residual Stress, SZ……..…...63
Figure 61 Effect of Particle Velocity on Induced Residual Stress, SX…………………..…..63
Figure 62 Effect of Particle Velocity on Induced Residual Stress, SZ…………………..….64
Figure 63 Flat Sample of AZ31B for Stress Relief Process; a) Drawing, b) Uncoated Sample, c) Coated Sample…………………………………….………………65
Figure 64 XRD Results for In Depth Measurement of Stress Relieved/Coated Samples, a) Profile of Residual Stress through depth, b) Peak Width Distribution………..67
Figure 65 Comparison of XRD Result with SX from 41 Particle Simulation………………68
Figure 66 Round Specimens Used for Extracting S-N Curve of AZ31B; a) Drawing, b) Uncoated, c) Coated………………………………………………..……….…70
Figure 67 Investigation of the Stress Concentration on Hourglass Area of Cylindrical Specimen, a) Model of RBM Housings and Cylindrical Specimen, b) FEA Result on the Hourglass Area of the Cylindrical Specimen…………………………..…71
Figure 68 Rotating Bending Machine Used for Fatigue tests………………………………72

Figure 69 S-N Curves of As Received, Stress Relieved and Stress Relieved/Coated Specimens of AZ31B……………………………………..…………….…….74
Figure 70 Fatigue Surfaces of round Specimens under Different Types of Loading……….75
Figure 71 a) and b), Fracture Surface of As Received Specimen with the Nominal Stress of 165 MPa……………………………………………………..……………….76
Figure 72 a) and b), Fracture Surface of Stress Relieved Specimen with the Nominal Stress of 188 MPa…………………………………………………………..………..77
Figure 73 Fracture Surface of Stress Relieved/Coated Specimen with the Nominal Stress of 188 MPa, a) and b), Crack Initiation Region, c) Coating Layer……............…....80

List of Tables

Table 1 Properties of Pure Magnesium……………………………………………..……..……4
Table 2 Convention for Alloy Elements Designation……………………………….……6
Table 3 Temper Designations for Magnesium Alloys………………………………………6
Table 4 Summary of Available Wrought Magnesium Alloys………………………………7
Table 5 Mechanical Properties of AZ Alloys……………………………………………….9
Table 6 Chemical Composition of AZ31B………………………………………………….9
Table 7 Possible Methods for Surface Treatment of Magnesium Alloys…………………..12
Table 8 Operating Parameter Ranges of the Stationary and Portable Systems…………….13
Table 9 Fatigue Endurance Limit of Titanium Alloy Ti6Al4V Before and After Deposition of Pure Titanium Using Cold Spray Coating ……………………….….….……33
Table10 Material Properties Constants Provided by Albinmousa et al. [3]…………...……39
Table11 XRD Stress Measurement Results on As Received and Stress Relieved Samples..66
Table12 XRD Results for In Depth Measurement of Stress Relieved/Coated Samples…….66
Table13 RBM Test Results ……………………………………..……………….……….74
Table14 XRD Results on Cylindrical Specimens……………………………….………..80
Table15 Life Improvement after Coating the Stress Relieved Specimens………………….81

Chapter 1 Introduction

Strength to weight ratio is an important factor for structures in automotive and aerospace industries. This is the reason why magnesium alloys with high specific strength are attractive candidates for these industries. There are two types of magnesium alloys, casting alloys and wrought alloys. Casting magnesium alloys with very good castability have a wide application in non structural applications. Wrought magnesium alloys with specific gravity of 1700 Kg/m^3 are the lightest structural alloys that are used in the automotive and aerospace industries. This thesis is devoted to the study of wrought magnesium alloy, AZ31B.

AZ31B is produced by extrusion process with aluminum and zinc as the main alloying elements and has the lowest resistance against corrosion among aluminum/zinc (AZ) magnesium alloys. One of the methods used to protect AZ31B against corrosion is cold spray coating. This process was introduced in the 1980s. In this process, the surface of the component is bombarded by particles with sizes of 5 to 100 µm that have been accelerated by pre-heated steam of gas to supersonic velocities of up to 1200 m/s. Due to the high plastic deformation resulting from the impact of particles on the component surface, local bonding between the component and particles occurs. Several layers of particles are deposited on the component, coating the surface and providing a uniform protective layer with little porosity. The process shows better results for metallic components but the protective material can vary from metallic alloys to ceramics. Since the cold spray coating process temperature is much lower than the melting temperature of the component, there is no thermal residual stress as observed in other coating processes such as thermal coatings.

The process of impingement of particles to the component surface is similar to the shot peening process. The difference is that the size of particles is smaller and their velocity is higher. Although the main purpose of cold spray coating is corrosion protection, the similarity of the process to shot peening poses the question of whether we can expect similar results of fatigue strength improvement from cold spray coating. This thesis is attempting to answer this question for the application of cold spray coating of aluminum particles on wrought magnesium alloy, AZ31B.

This thesis includes two main parts. The first part is elaborated in chapter 3 and investigates the residual stress resulted from cold spray coating. Two methods of numerical and experimental methods have been used for this purpose and the results have been compared. For the first method, after investigating several FEA software packages, ANSYS classic code was selected for the analysis. Considering the anisotropic and asymmetric material properties of AZ31B, ANSYS code was the only package that provided the best material model for the analysis. Nevertheless ANSYS classic code is implicit and analysis of dynamic high rate plasticity with this code was a challenge. For the second method, X-Ray Diffraction (XRD) method was used for stress measurement. Flat samples of AZ31B were stress relieved using ASM recommended method and coated. In depth residual stress measurement was applied on coated samples. The results from two methods were compared. Although the results were not identical due to assumptions of FEA and error factors of XRD, they demonstrated substantial agreement. The magnitude and location of the maximum compressive residual stress were in agreement from the results of both numerical and experimental methods.

The second part of this work is discussed in chapter 4 and is devoted to investigating the effect of residual stress induced by cold spray coating of aluminum particles on fatigue life of AZ31B substrate. Cylindrical specimens with hourglass shape were tested using an R.R.Moore rotating bending machine. Three groups of specimens were prepared for the tests; as received, stress relieved and stress relieved/coated. The stress relief and coating processes were the same as what was used in chapter 3. The specimens then were tested by rotating bending machine and the S-N curve of each group was prepared for comparison.

The test results show that there is a considerable drop of fatigue strength after the stress relief process, especially in the low cycle area. This was expected since the stress relief effectively removed the compressive residual stress of the as received specimens, resulting from the extrusion fabrication process. In the comparison between stress relieved and stress relieved/coated specimens, the results showed improvement in fatigue strength. The maximum improvement of 49 percent was observed in the load of 120 MPa. The endurance limit also enhanced 9 percent. This improvement in the fatigue life of stress relieved specimens is estimated to be due to the residual stress induced by cold spray coating.

Chapter 2 Background and Literature review

One of the key goals for automotive and aerospace industries is weight reduction of components. This not only saves on energy consumption but also reduces emissions and consequent environmental impacts. Considering this goal, using light alloys as structural members is a main strategy. Magnesium alloys with considerable high specific strength are attractive candidates for this purpose. During recent years more researches have focused on different aspects of these alloys.

2.1 Magnesium Alloys

2.1.1 Magnesium Alloys Characteristics and Applications

Magnesium is the lightest structure metal used in the industry. Table 1 shows some of the key properties of pure magnesium [1].

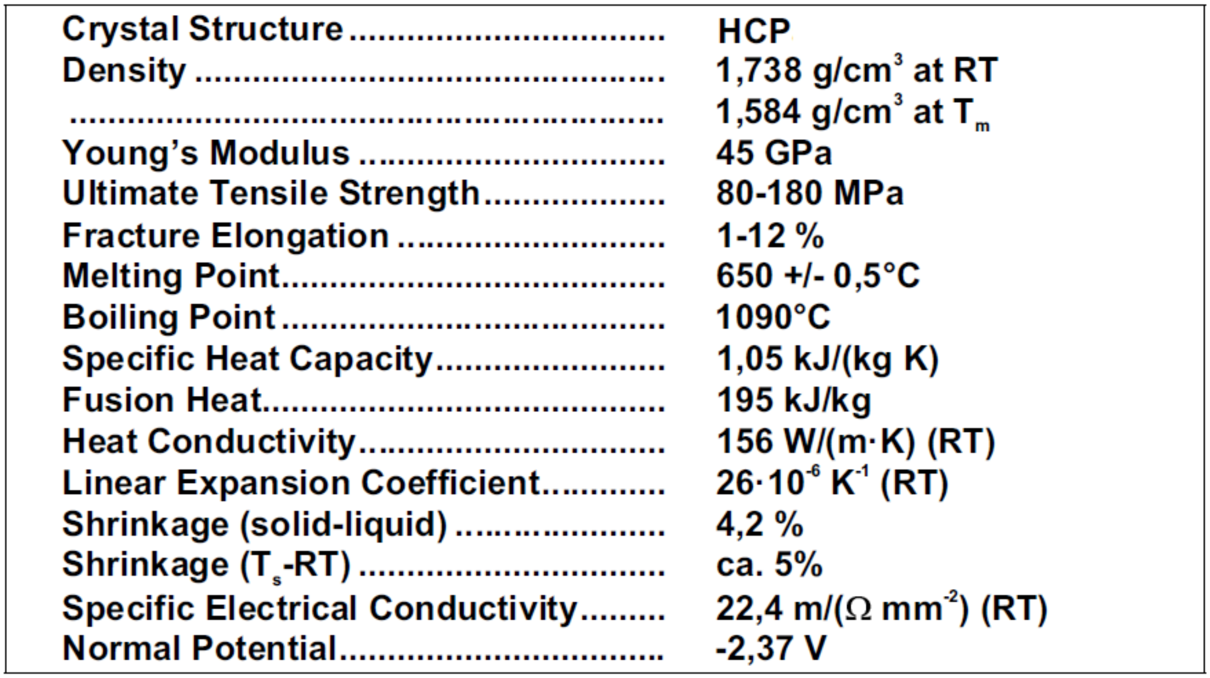

Crystal Structure	**HCP**
Density	**1,738 g/cm^3 at RT**
	1,584 g/cm^3 at T_m
Young's Modulus	**45 GPa**
Ultimate Tensile Strength	**80-180 MPa**
Fracture Elongation	**1-12 %**
Melting Point	**650 +/- 0,5°C**
Boiling Point	**1090°C**
Specific Heat Capacity	**1,05 kJ/(kg K)**
Fusion Heat	**195 kJ/kg**
Heat Conductivity	**156 W/(m·K) (RT)**
Linear Expansion Coefficient	**$26 \cdot 10^{-6}$ K^{-1} (RT)**
Shrinkage (solid-liquid)	**4,2 %**
Shrinkage (T_s-RT)	**ca. 5%**
Specific Electrical Conductivity	**22,4 m/(Ω mm^{-2}) (RT)**
Normal Potential	**-2,37 V**

Table 1- Properties of Pure Magnesium [1]

Magnesium alloys are good candidates where weight saving is important, Specific strength of magnesium alloys compete or exceed that of aluminum and steel alloys. Figure 1 compares density and specific strength of some selected alloys [1]. In this figure grey bars present the densities and the black bars show the specific gravities.

Magnesium has Hexagonal-Close-Packed structure (HCP). Because of this crystal structure, magnesium alloys show low ductility in low temperature while extensive deformability occurs above 225 °C. Magnesium alloys provide good machinability and casting properties but they are poor in cold working and corrosion resistance. New research is focusing on improving these weaknesses [1].

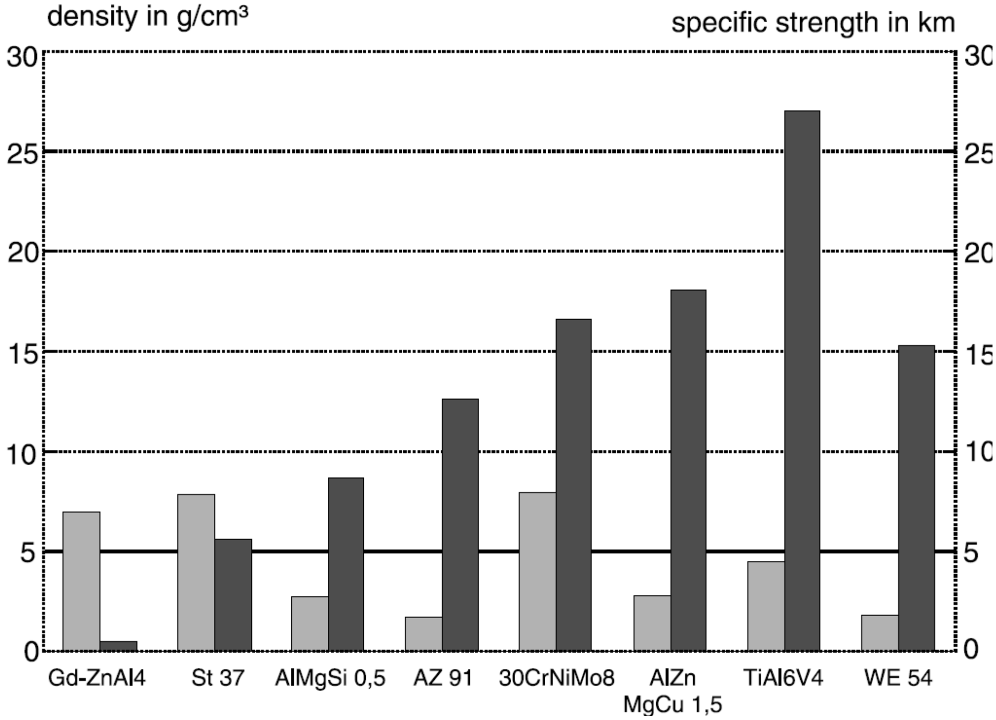

Figure 1- Densities and Specific Strengths of Selected Materials [1]

To improve mechanical properties, processability, and corrosion resistance, some specific elements are used in magnesium alloys. Identification of these alloys has been standardized. Based on ASTM standard, magnesium alloys are presented by letters referring to main alloy elements followed by their rounded percentage in the alloy. For example AZ31 includes around 3% aluminum and 1% zinc. Additional information or variation may be included by adding some letters after the last composition number that describes fabrication details and stage of development. Tables 2 and 3 present elements and temper designations for magnesium alloys [2].

2.1.2 Casting Alloys

Since magnesium alloys pose very good castability, they are used for casting and die-casting applications. AZ, AM, AS and AE alloys are the four main groups of magnesium casting alloys. AZ91 with extreme amount of 9% aluminum has a superb castability and can be used for the most complex parts.

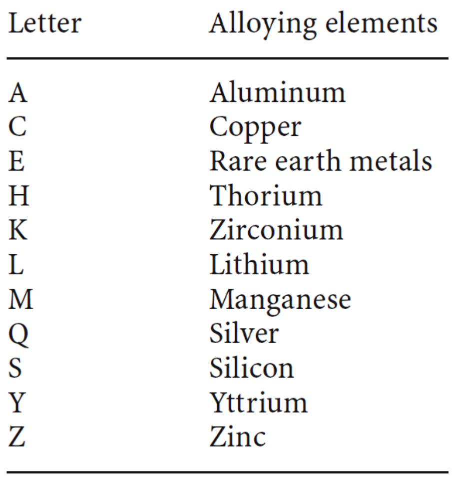

Letter	Alloying elements
A	Aluminum
C	Copper
E	Rare earth metals
H	Thorium
K	Zirconium
L	Lithium
M	Manganese
Q	Silver
S	Silicon
Y	Yttrium
Z	Zinc

Table 2- Convention for Alloy Elements Designation [2]

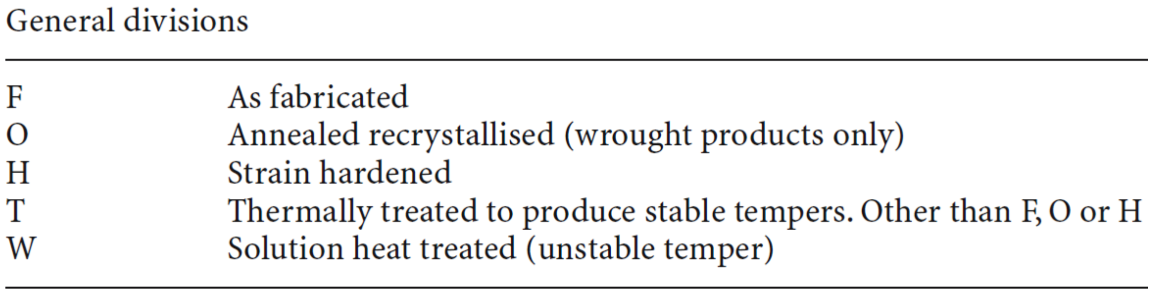

General divisions	
F	As fabricated
O	Annealed recrystallised (wrought products only)
H	Strain hardened
T	Thermally treated to produce stable tempers. Other than F, O or H
W	Solution heat treated (unstable temper)

Table 3- Temper Designations for Magnesium Alloys [2]

2.1.3 Wrought Alloys

Because of the HCP structure of magnesium, magnesium alloys show poor cold workability. Wrought alloys are hot-worked at temperatures over 330 °C by rolling, extrusion and forging. Some cold working may be applied after to prevent crack formation. In general, wrought alloys have better strength than casting alloys. Table 4 shows composition of some selected wrought alloys [1].

alloy	Al	Ca	Zn	Mn	Cu	Zr	Y	Nd	Th
AZ21X1	1,6-2,5	0,1-0,25	0,8-1,6	0,15 max.	0,05				
AZ31	3,0		1,0	0,3					
AZ31B	2,5-3,5	0,04 max.	0,7-1,3	0,20-1,0	0,05				
AZ61A	5,8-7,2		0,40-1,5	0,15-0,5	0,05				
AZ80	8,5		0,5	0,12					
AZCOML	2,0-3,6	0,04 max.	0,3-1,5	0,15 min	0,10				
AZM	6,0		1,0	0,3					
ZC71			6,5	0,7	1,2				
ZK40			3,5-4,5			0,45 min			
ZK60A			4,8-6,2			0,45 min			
ZM21			2,0	1,0					
ZW3			3,0			0,6			
HM21				0,8					2,0
HM31						0,7			2,0
WE43						0,5	4,0	4,0	
WE54						0,5	5,25	3,5	

Table 4- Summary of Available Wrought Magnesium Alloys [1]

2.1.4 Mechanical Properties

As mentioned, magnesium alloys have good casting properties while they show poor properties for plastic forming, especially in room temperature. This is the main aspect which differentiates casting and wrought alloys. On the other hand, wrought alloys show higher mechanical properties especially by specific thermo-mechanical treatments.

A comparison between casting and wrought alloys from this point of view has been shown in Figure 2 [2].

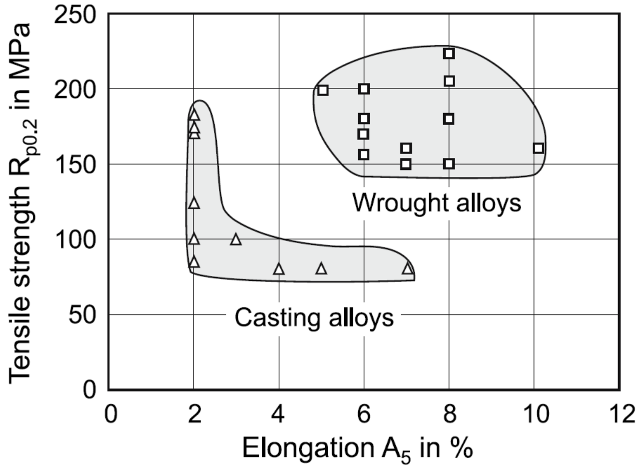

Figure 2- Elongation and Tensile Strength of Magnesium Casting and Wrought Alloys [2]

Since the focus of this work is on AZ31B which is a wrought alloy, we focus more on the details of wrought alloys and specifically AZ31B.

Main alloying elements of wrought alloys are aluminum (up to 10%), manganese (up to 2%), and zinc (up to 1.5%). Mechanical properties vary in a wide range with alloying elements and also with thermal treatments. Figure 3 compares elongation and tensile strength of different wrought alloys [2].

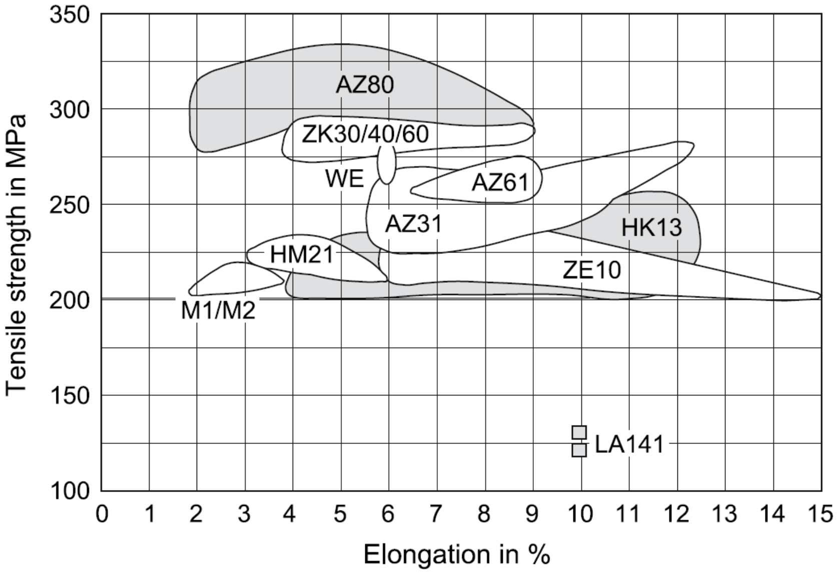

Figure 3- Elongation and Tensile Strength of Wrought Magnesium Alloys [2]

2.1.5 AZ Wrought Alloys

AZ wrought alloys with aluminum and zinc as main alloying elements include three major groups of AZ31, AZ61 and AZ80. Since aluminum improves mechanical properties, AZ31 has the lowest mechanical properties and is used for parts with moderate stress level. This alloy presents better formability and weldability compared to AZ61 and AZ80. In case the alloy is processed by extrusion or forging, it is called AZ31B. Magnesium alloys AZ61 and especially AZ80 show better corrosion resistance in High Purity (HP) condition while AZ31 has the lowest corrosion resistance in this group. Table 5 provides mechanical properties of AZ alloys [2].

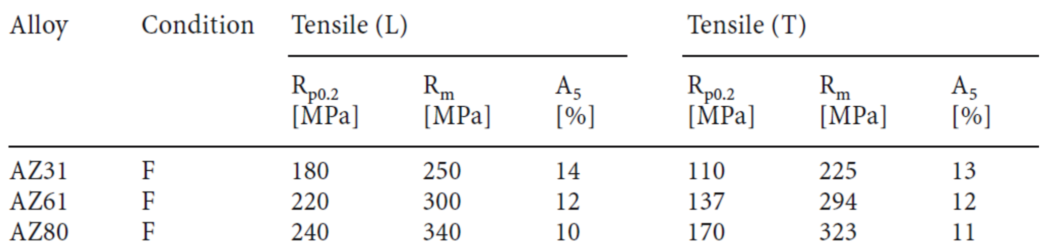

Alloy	Condition	Tensile (L)			Tensile (T)		
		$R_{p0.2}$ [MPa]	R_m [MPa]	A_5 [%]	$R_{p0.2}$ [MPa]	R_m [MPa]	A_5 [%]
AZ31	F	180	250	14	110	225	13
AZ61	F	220	300	12	137	294	12
AZ80	F	240	340	10	170	323	11

Table 5- Mechanical Properties of AZ Alloys [2]

2.1.6 AZ31B Mechanical Properties

Table 6 presents chemical composition of AZ31B [3].Because of the HCP crystal structure, AZ31B shows different mechanical properties in different directions. It also behaves different in tension and compression. In the other words this alloy is both anisotropic and asymmetric. More details about these characteristics of AZ31B and its influence on FEM analysis will be discussed in more detail in section 2.1.2.

Al	Mn	Zn	Fe	Ni	Cu
3.10	0.54	1.05	0.0035	0.0007	0.0008

Table 6- Chemical Composition of AZ31B [3]

Albinmousa et al. [3] have provided monotonic stress- strain curves of AZ31B in different directions (Figures 4 and 5).

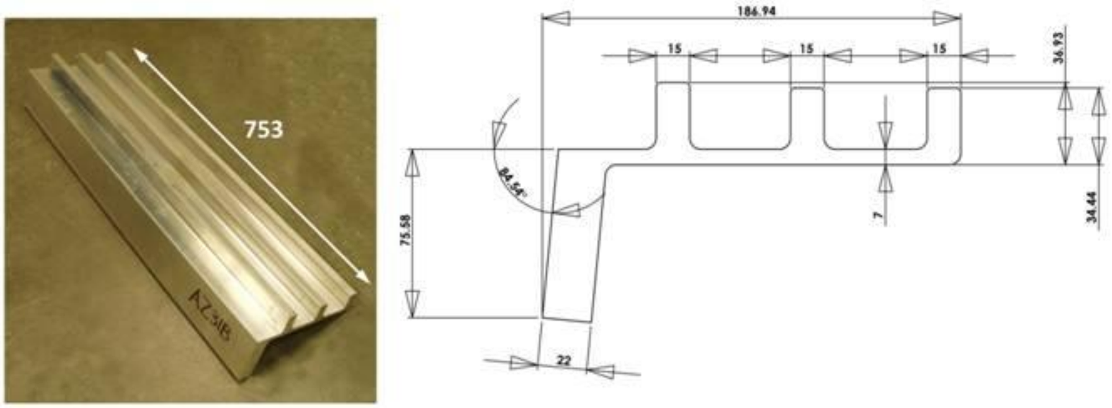

Figure 4- AZ31B Extrusion Piece Used for Experiments, All Dimensions in mm

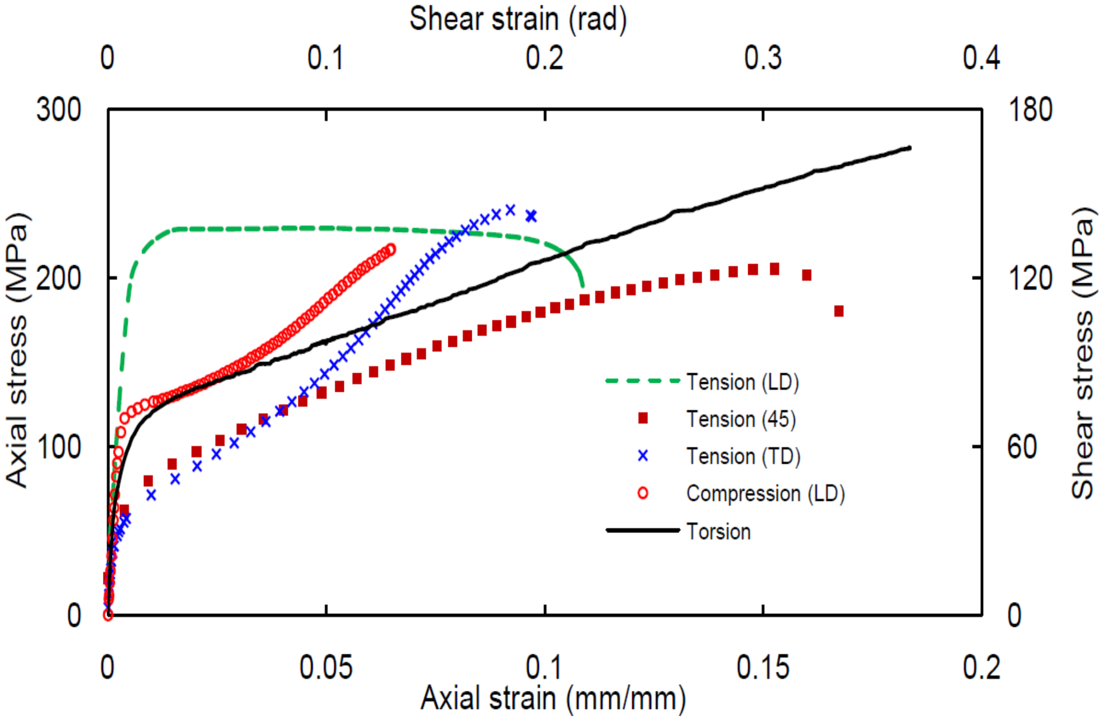

Figure 5- Monotonic Tensile, Compressive and Shear Behaviour of AZ31B Extrusion [3]

2.1.7 Corrosion Resistance of Magnesium Alloys

Besides high specific strength, having a good corrosion resistance is a crucial characteristic for structural alloys, especially in automotive and aerospace industries where components may work in aggressive environments. Landkof [4], declares that one of the main reasons for drop of demand for magnesium alloys in the 70's and 80's was "poor corrosion resistance, particularly, the so-called galvanic corrosion". In the 90's this problem was addressed by some solutions such as introducing high purity alloys and developing new techniques of coating, plating and surface treatment [4]. Kurze [1] classifies the corrosion protection measures of magnesium alloys in three groups:

1- Improving the purity of magnesium alloys

   Galvanic corrosion is very high in magnesium alloys which contain high amounts of iron, copper, and nickel. High Purity (HP) alloys with lower amount of these elements are much more corrosion resistant. Figure 6 [1] compares the corrosion rate of AZ91 (old version) to AZ91HP and some other alloys.

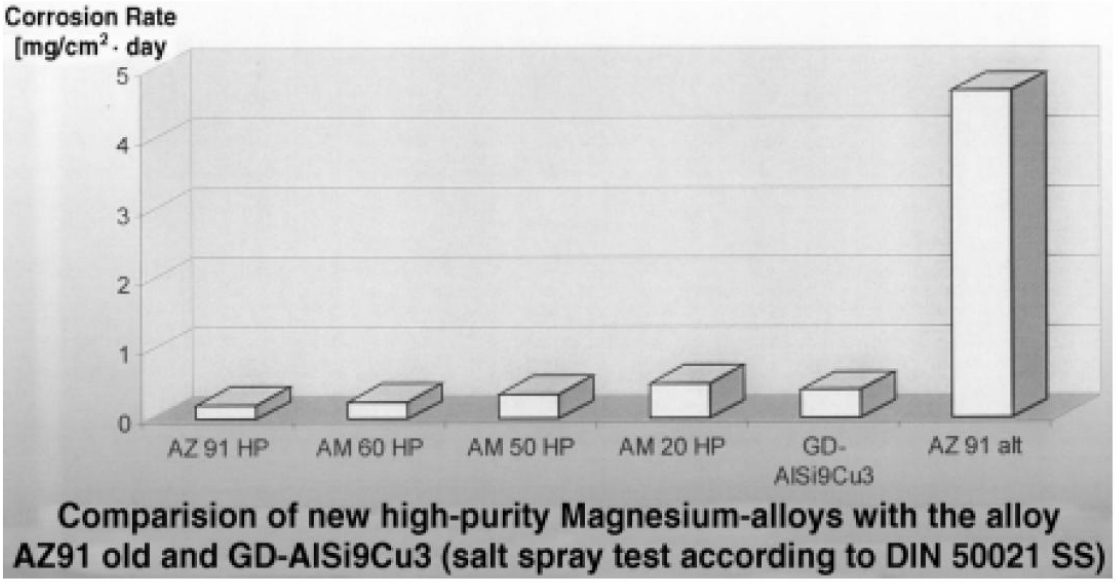

Figure 6 – Corrosion Tests on Magnesium Die-Casting Alloys [1]

As figure 6 shows, an old version of AZ91 in a salt-spray test corrodes 19 times faster than AZ91HP. Figure 7 compares the influence of different alloying elements on corrosion of magnesium alloys [5].

2- Addition of Specific Alloying Elements

Addition of some rare earth elements such as Ld, La and Ce can improve corrosion resistance of magnesium alloys as well. An example is WE54 which has excellent corrosion resistance.

3- Surface treatment

In spite of considerable improvement of corrosion resistance in HP alloys, still they need surface treatment for more development. Table 7 presents some of the possible surface treatments of magnesium alloys [1].

Cold spray coating is one of the modern coating processes which is being considered more as an emerging solution for protecting magnesium alloys against corrosion. This process will be discussed in detail in the next section.

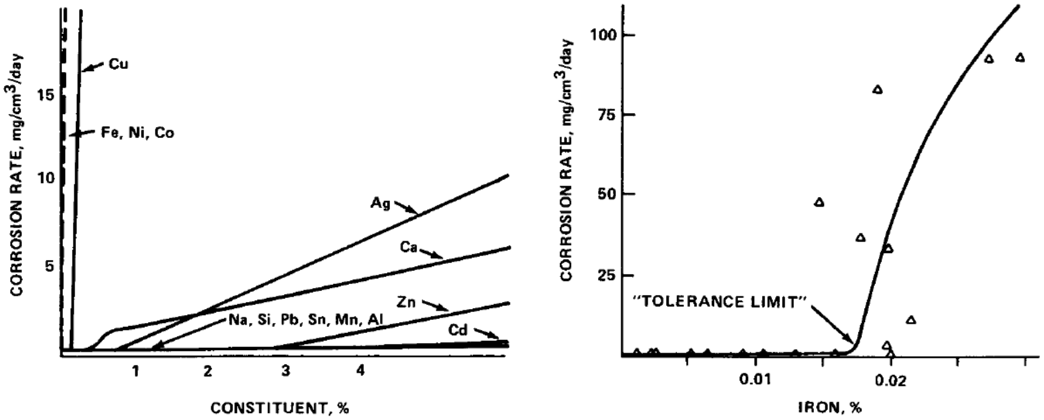

Figure 7- Comparison of Different Alloying Elements on Corrosion of Magnesium Alloys [1]

Methods for the surface pre-treatment	mechanically: grinding, polishing, brushing, blasting		
	cleaning: use of organic solvents and/or alkaline cleaners		
methods for inorganic coatings on the Mg surface	chemical treatment	electrochemical treatment	physical methods
	bondering	anodizing (HAE, DOW, UBE, TAGNITE, MAGOXID)	PVD
	chromating	galvanizing (Zn, Cu, Ni, Cr, etc.)	flame-spraying plasma-spraying
		electroless segregation such as chemical nickel-plating	
methods for organic coatings on the Mg surface, i.e. on the inorganic coating		painting	
		wet paint	
		powder lacquer	
		textured paint	
		dip paint	
		sliding lacquer	

Table 7- Possible Methods for Surface Treatment of Magnesium Alloys [1]

2.2 Cold Gas Spray Coating Process

2.2.1 Cold Spray Process

Cold gas spray coating or in brief cold spray coating initially was developed in the1980s at the Institute of Theoretical and Applied Mechanics of the Russian Academy of Sciences. In this coating process metal powder particles (5 to 100 µm) are accelerated through a high velocity stream of preheated gas to supersonic velocity (300 to 1200 m/s). After exiting the accelerating nozzle, the particles impact the surface of the substrate and because of high rate plastic deformation and local bonding, the particles bond to the substrate. As the process continues, the next particles bond to deposited particles and a uniform coating with little porosity is formed [6,7]. Figure 8 shows the configuration of typical cold spray systems and Table 8 compares operating parameters of the stationary and portable systems [8].

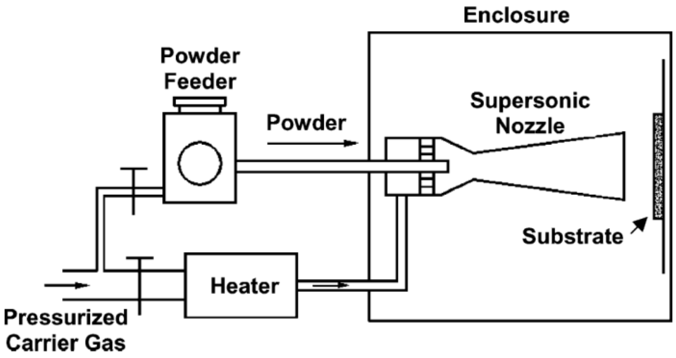

Figure 8- Schematic of a Typical Cold-Spray System [8]

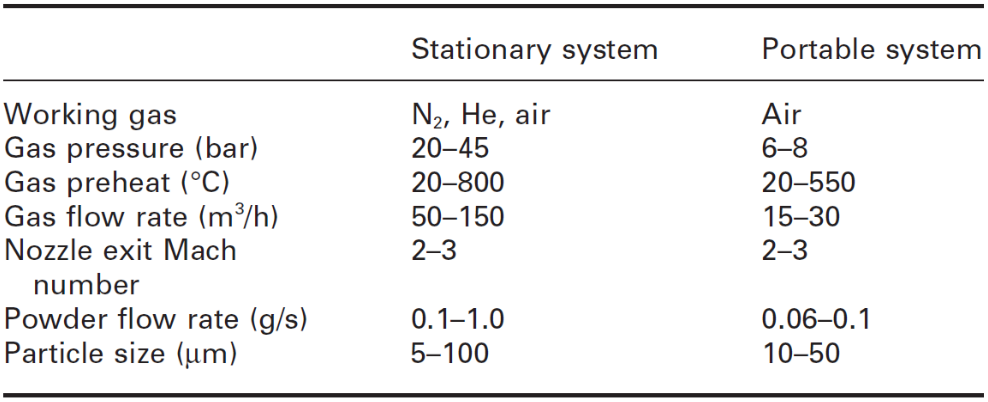

	Stationary system	Portable system
Working gas	N_2, He, air	Air
Gas pressure (bar)	20–45	6–8
Gas preheat (°C)	20–800	20–550
Gas flow rate (m^3/h)	50–150	15–30
Nozzle exit Mach number	2–3	2–3
Powder flow rate (g/s)	0.1–1.0	0.06–0.1
Particle size (µm)	5–100	10–50

Table 8- Operating Parameter Ranges of the Stationary and Portable Systems [8]

Figure 9 [8,10] shows morphology of different powders and figure 10 [11] presents an SEM image of copper particles bonded on a copper substrate.

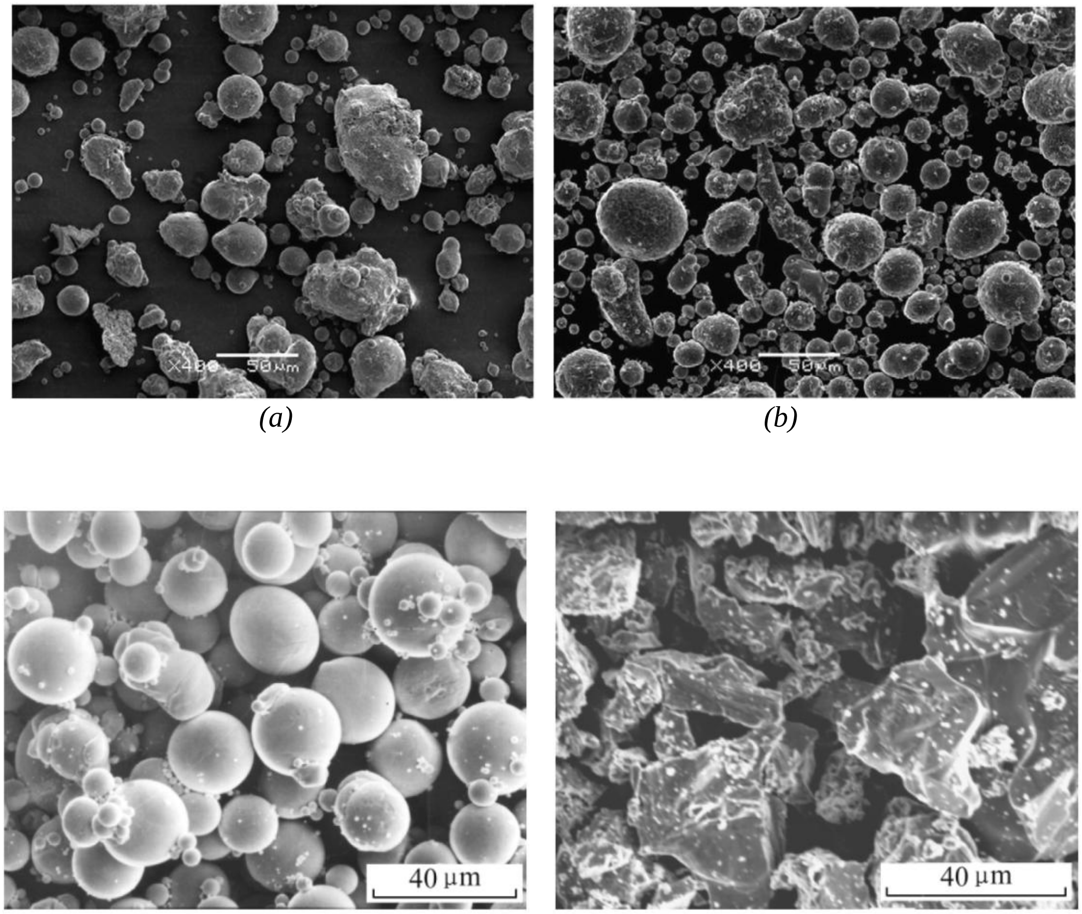

(a) *(b)*

(c) *(d)*

Figure 9- Morphology of Different Feedstock Powders; a)Al-10Sn, b)Al-20Sn, c)Copper, and d)Titanium [8, 10]

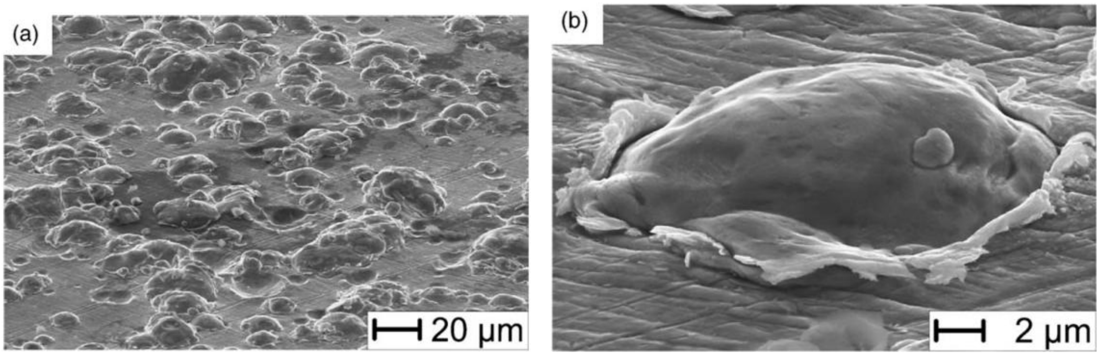

Figure 10- Scanning Electron Micrographs (Secondary Electron Mode) of Wipe Test Samples of Copper Particles on a Copper Substrate [11]

Since the temperature of the gas stream and particles are low compared to the melting point of particles, this process overcomes the two main disadvantages of traditional thermal spray coating, porosity and metal oxide impurities. Figure 11 compares the coatings produced by these two processes and the same feedstock powder [6].

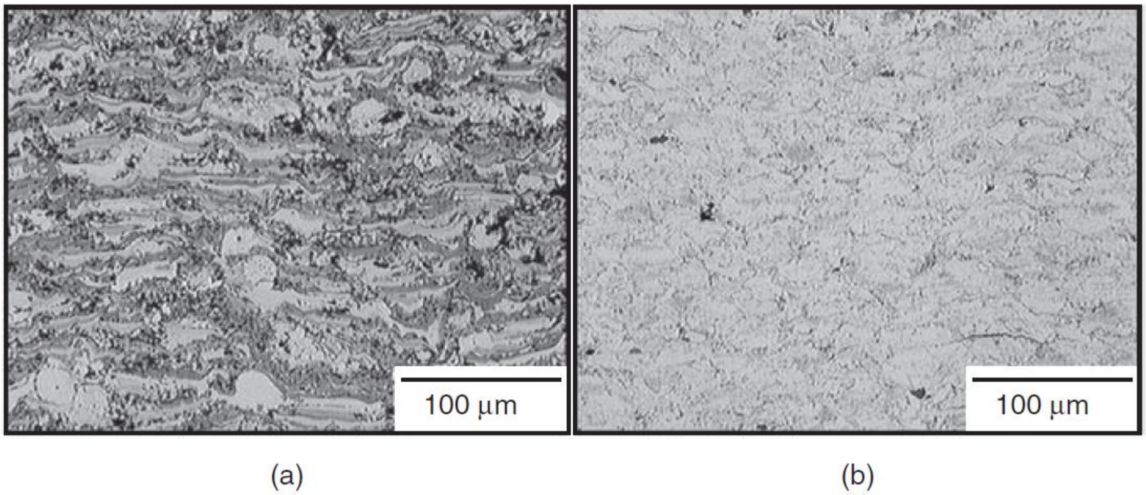

Figure 11- Comparison of Two Copper Coatings Produced from the Same Feedstock Powder; (a) copper plasma sprayed in ambient air showing 5% porosity (black areas) and 1.7 wt.% oxide (dark-gray bands), (b) copper cold sprayed in ambient air with <1% porosity and only 0.3 wt.% oxide (same oxide content as the feedstock powder) [6]

2.2.2 Research Trends

In recent years the major focus of research on cold spray coating has been on better understanding the cold spray process and the influence of process parameters on the results. Finding critical velocity, the velocity above which bonding occurs, and simulating the bonding process are two major research trends in cold spray technology. Some related works are reviewed in this section.

Assadi et al [11] simulated the impact of single particle and substrate by FEM and investigated the plastic deformation during the process. They concluded that bonding is attributed to adiabatic shear instabilities which occur at the surface of contact at high velocity. Comparing the low strength of copper coating resulted from experiment to strength of bulk material; they concluded that bonding happens in a fraction of contact surface. They also suggested that density and particle temperature are two main parameters determining the critical velocity.

In a similar work, Grujicic et al. [8] have numerically simulated the impact of a single spherical particle on a semi infinite substrate. They have investigated two cases of deposition of copper particles on aluminum and aluminum particles on copper. Experimental results show more efficient deposition of copper particles on aluminum. Their simulation has related this to higher density of copper particles which causes higher kinetic energy, higher pressure at the contact area and larger particle/substrate interfacial area. They also show that interfacial instability has a major role in causing interfacial roll-ups and vortices which cause material mixing and mechanical interlocking and play a main role in bonding mechanism.

Li et al. [10] have studied the effect of spray angle on deposition efficiency. They have classified three ranges of spray angle: maximum deposition angle, transient deposition angle, and no deposition angle. In the first range which also determines critical deposition angle, similar to critical velocity, the deposition efficiency is 100%, in the second range the efficiency can vary between 0 to 100% and in the last range there is no deposition. The maximum and transient angle ranges depend on mean velocity of particle and the velocity distribution.

Using Abaqus Explicit, Li et al [12] have simulated impact of a 3D single spherical particle on a substrate and have investigated the influence of different settings on the results. They have shown that better results can be obtained by using material damage with the element excessive distortion. They also have concluded that by proper definition of material properties, the simulation can predict critical velocity.

Kim et al. [13] have studied the deposition of titanium particles on titanium, aluminum and zirconium substrates. These substrates have equal, lower and higher hardness relative to titanium particles, respectively. They have shown how the difference between the hardness of particle and substrate influences the quality of bonding as well as the shape of the particle and substrate after plastic deformation. They also have discussed how the oxide layer on the substrate is removed by plastic deformation during the impact prior to bonding. They have shown the effect of this layer on regional bonding and the voids created between the particles and substrate at the end of the process.

Some researchers believe in a metallurgic nature for bonding. They claim that because of high rate plastic deformation of particle and/or substrate, the temperature of some points increase rapidly up to melting point and at the points where oxide layer has been removed, metallurgical bonding happens. In spite of this belief, Morgan et al. [14] claim that the boding mechanism has more of a mechanical nature. They claim that metallurgic bonding occurs occasionally after breaking surface films by kinetic energy of particles. However by interpreting the results of SEM images of different coating samples, they show that the predominant mechanism for bonding is mechanical interlocking and not metallurgic bonding.

The results of the work done by Zhang et al.[15] show that the mechanism of bonding is more metallurgical. They have estimated the ease of initiation of deposition during the cold spray of pure aluminum on substrates of different substances. They realised that deposition on non metallic substrates was difficult and the difficulty is interpreted as the absence of metallurgic bonding. The deposition on soft metallic material was not considerable due to lack of hardness to cause deformation of particles. They concluded that the best deposition is in the case where the substrate is metallic and with higher hardness than the particle. In this state, the impact causes high deformation of particles and the pressure resulting from impact removes the oxide layer on the substrate and prepares metallurgical bonding between particle and substrate.

To investigate the influence of powder state on deposition behaviour, Kumar et al. [16] have studied the coating produced from smooth spherical and irregular granular copper powders on copper and aluminum substrates. The results of their tests show that bonding properties of irregular granular powder is better that smooth spherical ones. They have simulated the process by Abaqus Explicit and the simulation shows better bonding properties due to higher frictional dissipation effects.

King et al. [17] have studied the relationship between particle size and deformation in an experiment of aluminum and copper particles on ceramic substrate. They have concluded that aluminum particles less than 5 micrometer and copper particles of less than 2 micrometer don’t have enough flattering parameter, as a criterion for deformation of the particles. This has been related to their low kinetic energy which causes deceleration or deflection of the particles before impacting the substrate due to low shock effects in the gas flow.

Measuring the in-flight velocity of particles in low pressure cold spray process, Ning et al. [18] have found out that there is a decrease of in-flight velocity as the size of particles increase from 20 micrometer to 62 micrometer. This decrease is more for spherical particles compared to irregular particles of the same size. They also have found that pre heating feed stock powder reduces critical velocity and increases deposition efficiency.

2.3 Evaluation of Residual Stress Induced by Cold Spray Coating

A part of this work is devoted to simulation of the residual stress induced by cold spray coating by FEM and comparing it to the experimental results. For this purpose, some flat samples of AZ31B are prepared. After applying cold spray coating on these samples, the stress of as received, stress relieved and stress relieved/coated samples are measured at the surface using the X-Ray Diffraction method. For the coated sample, the stress is measured along the depth as well. This helps to evaluate the residual stress induced by cold spray coating. The results of this stress measurement are then compared to finite element analysis results. This investigation has been provided in details in section 2.

As mentioned, most of the focus of the research in cold spray coating is on the process itself. The simulations provided for this process have been more targeted for finding critical velocity or evaluating the bonding mechanism. On the other hand, the impingement of particles on substrate in cold spray coating is very similar to the shot peening process. The difference is the size of particles and the velocity but the nature of the residual stress induced in both processes is similar. The lack of data in literature about FEM simulation of residual stress in cold spray coating and also rich literature for shot peening process, led us to review literature of the shot peening.

In the literature, three methods of evaluation of residual stress induced by shot peening can be recognized: analytical, experimental, FEM, and a combination of the three methods. Among these categories, FEM analysis is the most common method which in some cases has been accompanied by experimental results. The reason for the popularity of this approach is the relative simplicity, the accuracy, and the flexibility of the method. The literature related to each category is discussed in this section.

Shot peening is a popular surface treatment for inducing compressive residual stress on the surface of the critical components and improving their fatigue life. Particles of diameter 0.18 to 3.35 mm and high hardness impinge the surface of the substrate with the velocity of 40 to 70 m/s and through plastic deformation on the surface, compressive residual stress is induced on the surface of the substrate. Figure 12 shows the typical profile of residual stress along the depth, induced by surface treatments such as shot peening and cold spray coating. Because of compressive residual stress on the surface of the component, high cycle subsurface cracks initiate at the tensile stress region of the component [36]. Similar crack initiation is expected for cold spray coating.

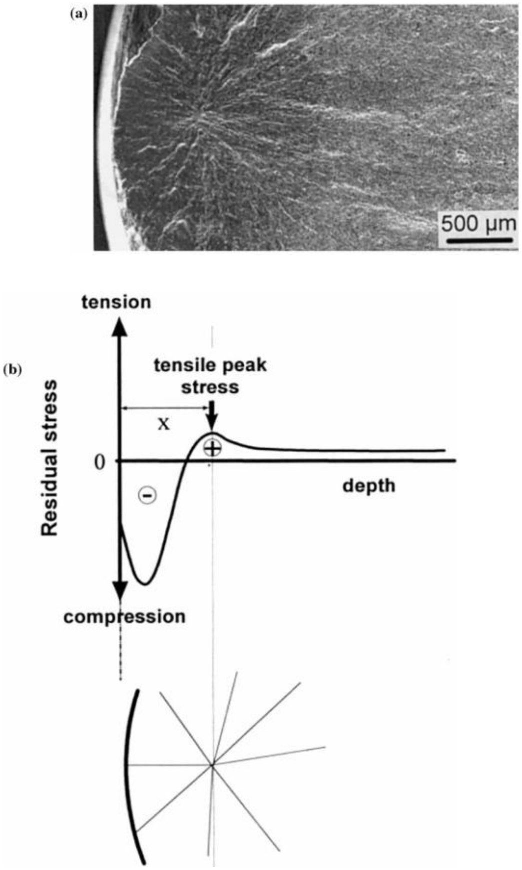

Figure 12- Subsurface Fatigue Crack Nucleation; a) Rotating Bending Specimen, Titanium Alloy, b) Schematic of Residual Stress Distribution and Crack Nucleation Point [36]

Finding a method for predicting the induced residual stress is an important topic for both academic and industrial researchers. Guechichi [19] developed an analytical model to predict the residual stress induced by shot peening in metallic parts. This model then was improved by Khabou [20]. Fathallah et al. [20] used the latter model and applied some more factors including friction, angle of impingement and hardness ratio in their model. The model related the pressure on the surface of substrate to the velocity of particle by Hertz's theory of elastic contact. They compared the analytical and experimental results that showed a good agreement between the results. In another analytical method with a different approach, Al-Hassani [22] used experimental results to develop a model for residual stress of elastic-perfectly plastic material. Although these models save in computation costs in comparison to finite element analysis, they are not flexible enough for complicated applications like impingement of particle on a non-flat target and the multiple particle impact and their interaction on each other. For this reason simulation of shot peening by FEA has been widely considered as an effective method by researchers.

Meguid et al. [23] evaluated the residual stress resulting by shot peening in a simulation using ANSYS. They studied the effect of velocity, shape and size of a single shot on the induced residual stress and plastic strains. They also checked the effect of hardening rate of bilinear elasto-plastic material on the results. They extended their evaluation to co-indentation of two shots and studied the effect of the separation distance on the results. They concluded that velocity and shape of shot, and the separation distance of co-indentation shots are most influential parameters of the process.

In similar research by Schwarzer et al. [24], the shot peening process has been simulated by Abaqus Explicit and the results have been compared to verification experiment results. The comparison shows a similar distribution of residual stress along the depth at the point of contact but different magnitudes for surface and maximum compressive residual stresses. They also have studied the effect of the size and velocity of shots and the angle of impingement. It has been shown that the size and velocity of shots change the depth of the compressive layer significantly while they don't have much influence on surface and maximum compressive stress magnitude. It also has been shown that increasing the impact angle reduces the depth and the magnitude of surface compressive stress and maximum residual stress.

Majzoobi et al. [25] have employed LS-DYNA code to simulate the shot peening process. They have used Johnson-Cook model, ignoring temperature effects and applying strain rate influence. They have extracted material property constants through experiments and have verified the profile of indentation with experiment which shows a good agreement between numerical and experimental results. Using these material properties, they have simulated single and multiple shot impacts in different velocities. They have concluded that increasing shot velocity improves residual stress distribution up to a limit which has been found to be 90 m/s. After this limit, increasing the shot velocity may decrease maximum compressive residual stress. They also have found 25 shots to be the optimum number of shots for simulation to produce a uniform distribution of residual stress.

For the purpose of lowering the tensile residual stress due to welding process, Meo et al. [26] have considered the application of shot peening. They have simulated the welding process and the resulting tensile residual stress by FEM. Then they have simulated the shot peening process and have found the distribution of final residual stress. Their simulation shows good agreement with experimental stress measurement and demonstrates how shot peening lowers significantly the tensile stress of welding along the path of welding and even creates compressive residual stress in the regions close to the welding path. They have concluded that this can improve fatigue life of welded components considerably.

Frija et al. [27] have used Abaqus Implicit to simulate shot peening. In this work, static loading has been used instead of dynamic impact. They have used energy equations and have calculated equivalent static pressure for dynamic impact and have used a static indentation approach. Assuming rigid shot and elasto-plastic material behaviour with damage for substrate, they have simulated indentation of single shot on the substrate. The simulation has been compared with experimental results.

The conventional method for evaluating compressive residual stress induced by shot peening is Almen-scale. This method was introduced by John Almen [48]. In this method a thin strip (SAE 1070 steel) with specified dimensions that is called Almen strip is fixed on a fixture and shot peening with 200% coverage is applied to it. After releasing the strip from the fixture, it will get a curved shape due to induced compressive stress. The height of the curve is measured by a gauge (Almen Gauge) and this height is a scale for measuring peening intensity and induced compressive stress [49]. This method has been the subject of some studies.

Schiffner and Helling [28] have simulated shot peening of steel plates by ADINA and have studied the influence of shot velocity and size on resulting parameters such as residual stress and residual indentation. They have compared the results with experimental observations. They recommend FEM as a powerful tool for studying shot peening parameters and measuring the peening intensity rather than conventional methods like Almen intensity.

In another simulation of shot peening by Abaqus Explicit, Gugliano [29] relates the results of simulation to the arc height of Almen strip so that the residual stress can be found from the value of Almen-Scale. He also develops analytical functions for relating shot velocity to Almen intensity. The results show good agreement with experimental measurements.

In an experimental evaluation of the residual stress induced by shot peening, Kobayashi et al [30] applied static compression and dynamic impact tests using steel ball on a flat steel plate. The results of stress measurement showed that in static compression tests, the stress at the centre of indentation was almost zero and compressive residual stress was induced close to the centre of the indentation. In dynamic impact test, surprisingly, the residual stress at the centre of the indentation was tensile and compressive residual stress was outside of the indentation area. The tensile stress at the centre changed to compressive when more impingements applied around the first impact point. They concluded that compressive residual stress induced by shot peening is the result of superposition of residual stress of surrounding impacts.

As mentioned before, the number of researches on evaluations of residual stress induced by cold spray coating is very limited. These works are reviewed here.

Phan et al. [31] simulated the process of cold spray coating by ANSYS. Their work includes two parts. In the first part, they have used ANSYS CFX to simulate accelerated particles in de Laval nozzle by supersonic jet of Helium at temperatures of 600 °C. During this process, the accelerated particles of pure titanium have a velocity of 700 m/s and temperatures of 600 °C at the exit. In the second part of their work, they have used an explicit program, ANSYS Autodyn, to simulate the impact of these particles to a substrate of titanium and finding the resulting stress distribution. Figure 13 shows the two steps of the simulation.

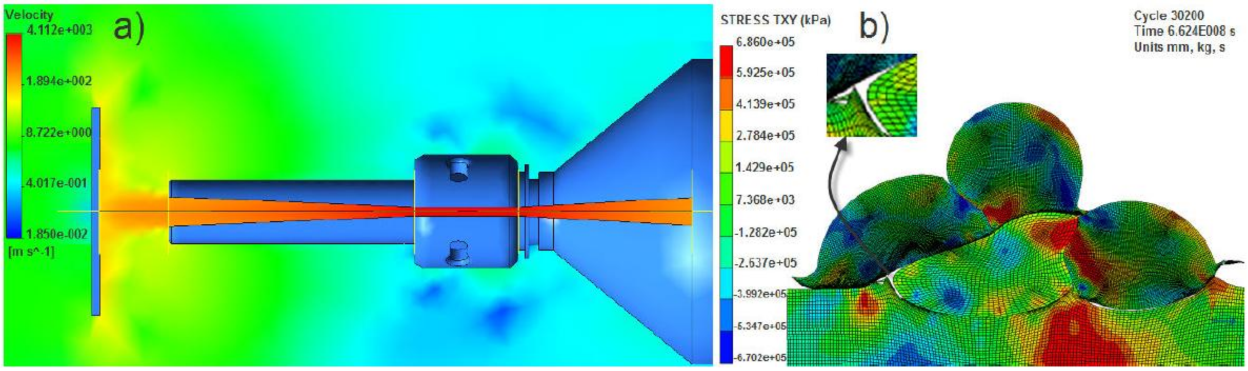

Figure 13 a) Gas Velocity Contour Plot of the Helium Gas Jet, and (b) FEM Calculated Stresses Contours [31]

They have concluded that the regions of more concentrated stress are the areas of interface (particle/particle and particle/substrate) and crack propagation more likely begins in these regions. They also have recommended that preheating the substrate can reduce residual stress. Finally, they have mentioned that the stress distribution after the cooling down of particles will change and more study and investigation of stress distribution in that state is needed.

Choi et al. [32] have made an integrated investigation on microstructure, mechanical, expansion and electrical properties of deposition of aluminum powder on aluminum substrate by cold spray coating. In one part of this study, they have measured the residual stress of substrate in two states; before cold spraying (after sand blasting) and after coating (Figure 14). After coating, the compressive residual stress has been balanced and the average compressive residual stress through thickness of the substrate is 10 MPa. They have concluded that the induced residual stress is insignificant especially when compared to thermal spray process, presumably because of absence of thermal stresses.

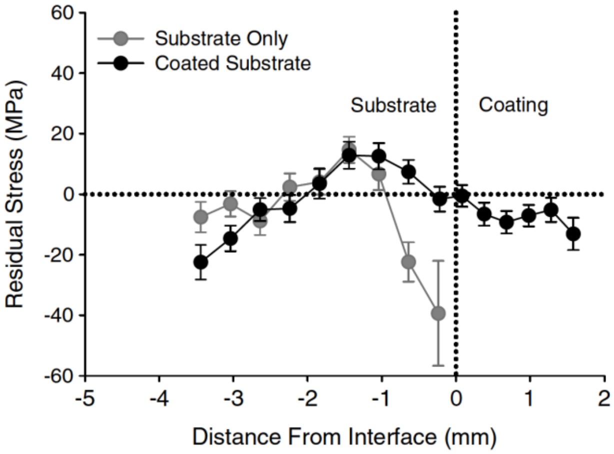

Figure 14- Residual Stress Before and After Cold Spray Coating of Aluminum Powder on Aluminum Substrate [32]

Through an experimental observation, Mc Cune et al. [33] have investigated different electrical and mechanical aspects of coatings produced by cold spray coating process using two different copper powders. They have used direct reduction and gas atomized copper powders. The first one is spongier with more oxygen content which causes minute oxide particles in the deposit and the second is denser with more of a spheroid shape. The substrate is commercial copper which is grit blasted by aluminum particles before coating. Figure 15 shows the distribution of measured residual stress through thickness. This comparison shows how the difference in the process of production and morphologies of feedstock powders can change mechanical properties of deposition and specifically residual stress in our case.

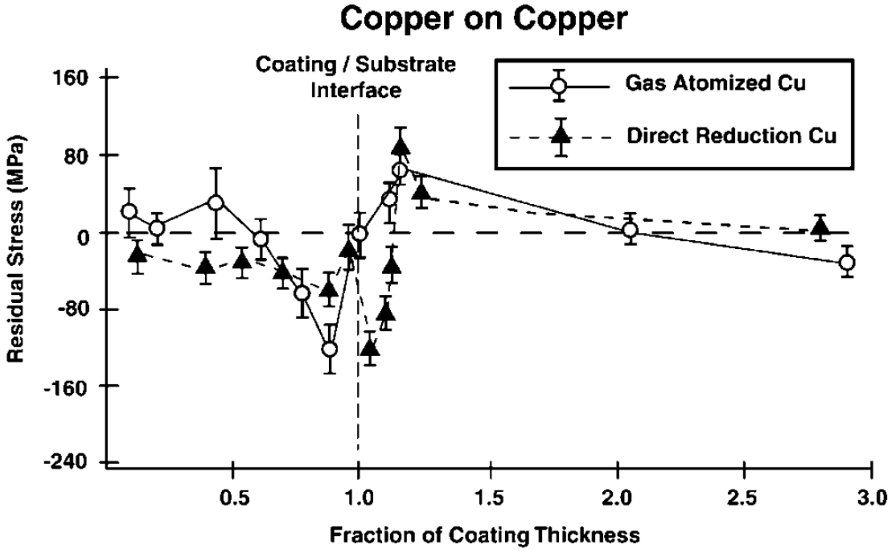

Figure 15- Comparison of Residual Stress Distributions of Gas Atomized and Direct Reduction Copper Powders [33]

Section Summary

- The residual stress induced in cold spray process is similar in nature to the resulting residual stress from shot peening.
- The research and evaluation of induced residual stress in cold spray is very limited compared to shot peening due to the relatively young age of this process
- The main approaches in evaluation of residual stress in both fields of cold spray and shot peeing includes: analytical, FEM, experimental, and combination of them
- The researchers in shot peening have mostly used FEM and have verified the results with experimental results.
- In cold spray field, the finite element method has been used mostly for simulating the process of cold spray and less attention has been paid to residual stress. Evaluation of residual stress has been done more by experiment, mostly by X-Ray Diffraction.

2.4 Residual Stress Induced by Cold Spray Coating and Fatigue Life

Surface treatments are applied on metallic components for different purposes. Some of them are used to improve fatigue strength while some are useful for protecting against corrosion. Shot peening for example, is a process that is used for fatigue life improvement while the main purpose of cold spray coating is corrosion protection. The impingement of particles to the surface of the substrate in cold spray coating is similar to the process of shot peening and it results in residual stress. Therefore it is estimated that cold spray coating may increase the fatigue life as well. This is being investigated in this project. For this purpose the S-N curves of uncoated and coated specimens of AZ31B are prepared using a rotating bending machine and then these curves are compared. Details of these tests are provided in section 3.

In this section, the literature involved in the relation between residual stress induced by cold spray coating and fatigue life is reviewed. Similar to section 1.3, because of the similarity between cold spray coating and shot peening processes, the research done on shot peening is reviewed as well. The main point of interest is the substrate of magnesium alloy, especially AZ31B, but all works with different particles and substrate materials are reviewed here.

2.4.1 Shot Peening and Fatigue Performance

Mayer et al. [43] have provided fatigue life of wrought, forged, cast, and fibre reinforced AZ magnesium alloys and compared them to aluminum alloy AlMgSi1. They have used ultrasonic fatigue testing methods with the loading frequency of 20 KHz which is used for fatigue test at high and very high cycle tests. Figure 16 shows S-N curves of AZ31hp which has been compared to AZ61hp and aluminum alloy AlMgSi1. Arrows demonstrate the specimens which passed the runout cycle and did not fail.

Zhang and Lindemann [34] have studied the influence of shot peening on high cycle fatigue life of wrought magnesium alloy AZ80. Using shot peening with glass beads, testing with rotating bending machine, and measuring stress by hole drilling method, they have evaluated the induced residual stress and change of fatigue life (Figures 17, 18). As Figure 18 presents, shot peening can modify the high cycle fatigue life by up to 60%, increasing fatigue strength from 100 MPa to 160 MPa. They have observed that magnesium alloys are sensitive to shot peening. Their fatigue strength is improved by shot peening up to a limit of Almen intensity and after that limit it reduces the fatigue strength dramatically. They have concluded that shot peening is a promising method for improving fatigue strength of magnesium alloys.

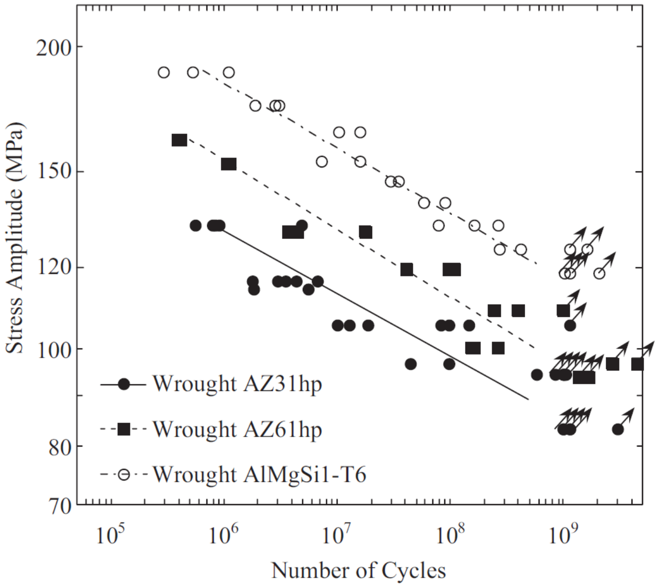

Figure 16- S-N Curves of AZ31hp, AZ61hp and AlMgSi1 [43]

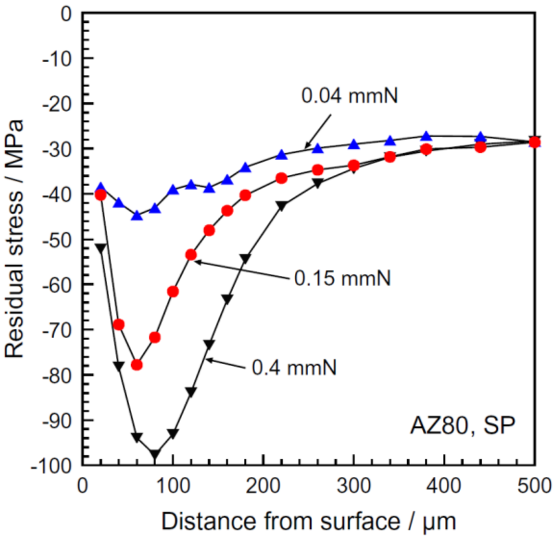

Figure 17- Induced Residual Stress by Shot Peening in AZ80 for Different Almen Intensities Ranging from 0.04 mmN to 0.4 mmN [34]

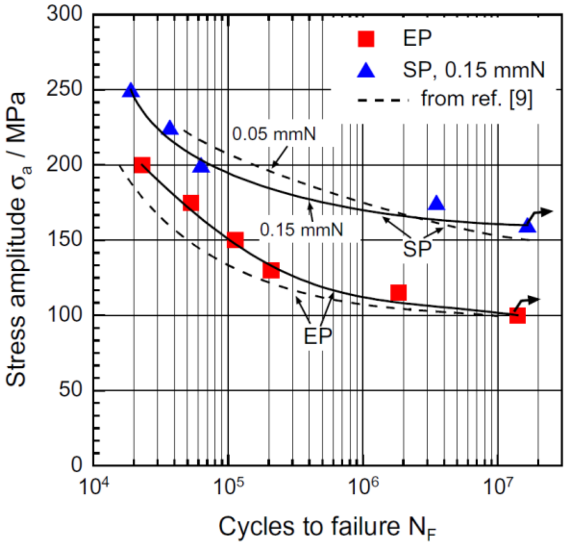

Figure 18- S-N Curves of Original Electro Polished (EP) and Shot Peened (SP) Specimens of AZ80 [34]

In a similar work, Dorr et al. [35] have compared the influence of shot peening on the fatigue performance of aluminum alloy Al2024 and magnesium alloy AZ80. They have performed several tests with different peening media and different Almen intensities. The results of the tests show that the fatigue performance depends strongly on Almen intensity and is independent from peening medium. The other remarkable result is that Al2024 fatigue strength improves by increasing Almen intensity up to a limit and then there is no more improvement while AZ80 shows to be sensitive to Almen intensity and after a critical limit, the improvement of AZ80 drops considerably. Figure 19 shows the results. Their observation about AZ80 is similar to what is reported by Wagner [37].

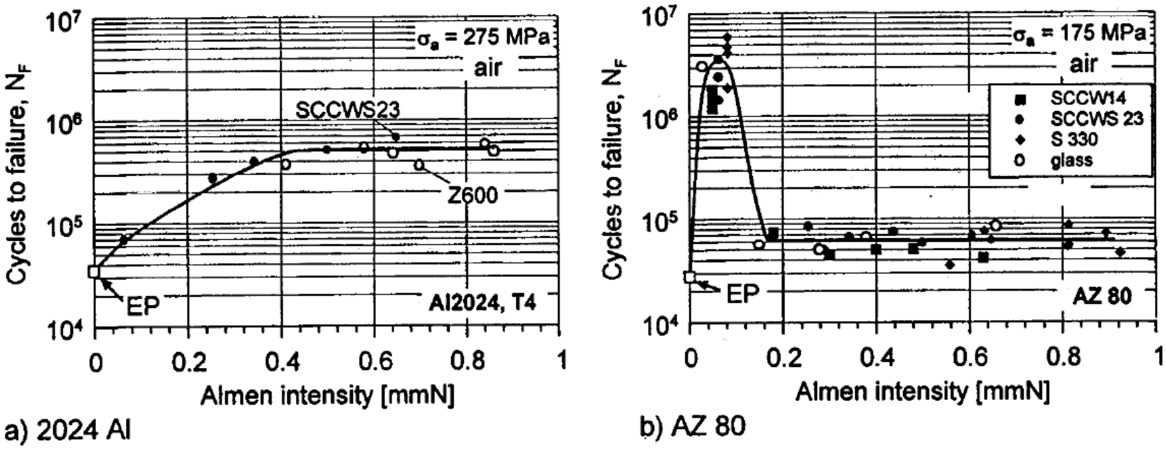

Figure 19- Influence of Almen Intensity on Fatigue Performance of Al2024 and AZ31 [37]

In another part of their work, Dorr et al. have investigated heavily shot peened specimens and the influence of surface removal on their fatigue performance. They have removed peeing induced micro cracks and dents by surface removal and have observed the results on fatigue performance. While no improvement is observed for Al2024, fatigue performance of AZ80 increased considerably after surface removal of about 100 µm (Figure 20).

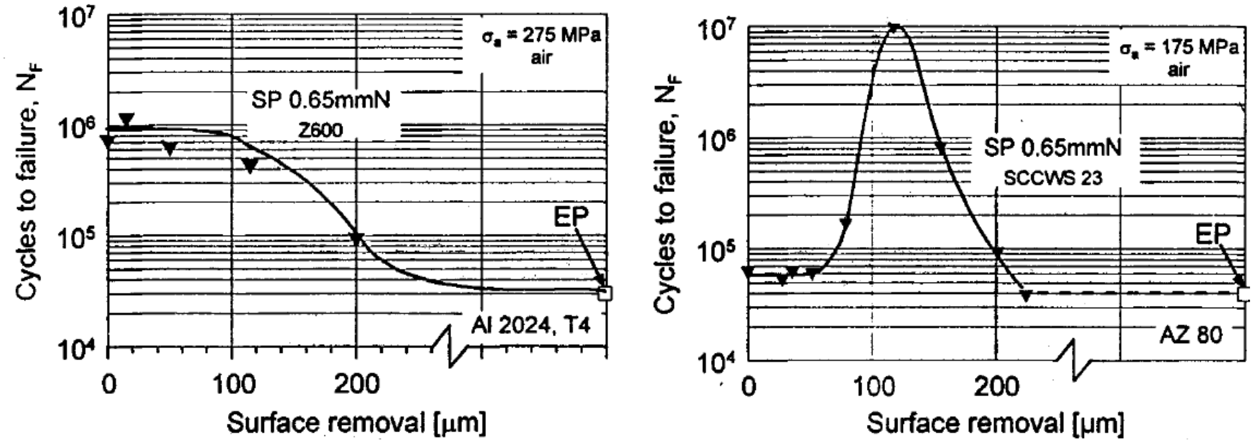

a) 2024 Al

b) AZ 80

Figure 20- Influence of Surface Removal on Fatigue Performance of Heavily Peened Specimens of AL2024 and AZ80 [37]

Wagner [36] has investigated the influence of different surface treatments such as shot peening, roller burnishing, and deep rolling, on the fatigue behaviour of titanium, aluminum, and magnesium alloys. Some results of this study show how magnesium alloy AZ80 is sensitive to peening intensity (Figure 21), how shot peening can lower its crack growth rate (Figure 22), and comparison of the effect of different surface treatments on S-N curve of AZ80 (Figure 23).

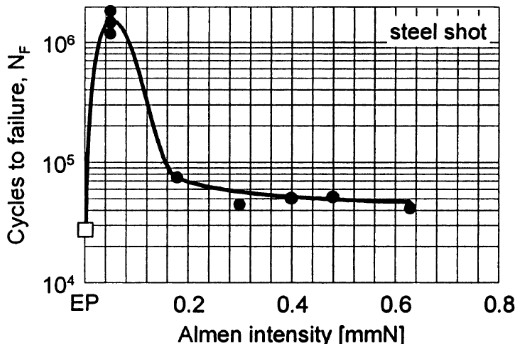

Figure 21- Response of Fatigue Life to Almen Intensity in AZ80 [36]

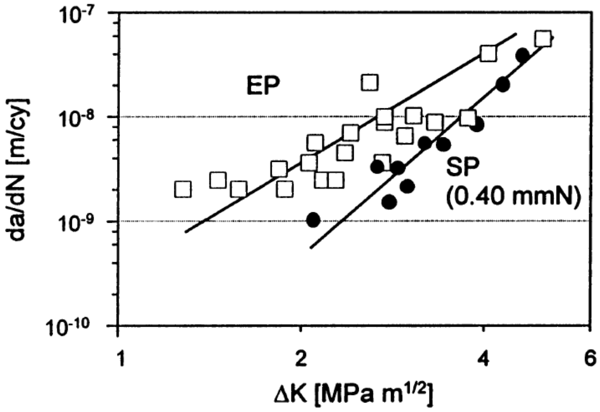

Figure 22- Crack Growth Rate for Electro Polished and Shot Peened AZ80 [36]

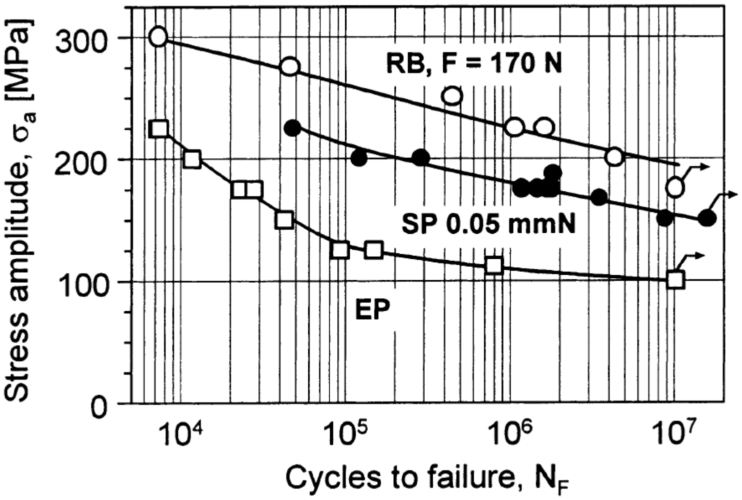

Figure 23- Effect of Shot Peening and Roller Burnishing on Fatigue S-N Curve of AZ80 [36]

The effect of different surface treatment and different environment conditions on fatigue life of AZ31 and AZ80 has been studied by Hilpert and Wagner [37]. They prepared S-N curves for both magnesium alloys which were electro polished and uncoated. They tested the specimens in vacuum, air, and 3.5% solution of NaCl. Their study shows that the best fatigue performance is in vacuum, followed by air and finally in a NaCl solution. They have repeated the tests in air and NaCl solutions for shot peened and roller burnished specimens. Both shot peening and roller burnishing treatments have improved fatigue strength in air but their improvement in NaCl is less effective. In addition, when exposed to NaCl solution, AZ80 is more sensitive. Also in this environment, shot peened specimens of both alloys are less resistant than roller burnished specimens. This has been interpreted to be due to the different surface roughness resulting from shot peening and roller burnishing.

Zinn and Scoltes [38] have investigated the effect of mechanical surface treatments, shot peening, and deep rolling on fatigue strength and surface microstructure of some aluminum base alloys and magnesium alloy AZ31. Figure 24 shows the residual stress distribution of AZ31 specimens for different shot peening treatments. In this study, the stress relaxation of AlZn4.5Mg1 and AZ31 after shot peening and through bending fatigue has been compared. Stress relaxation of AlZn4.5Mg1 is considerable in first cycle of load while this is not observed in AZ31 (figure 25). It has been mentioned that the interpretation of the results of AZ31 specimen is hard due to the low level of stress at the surface.

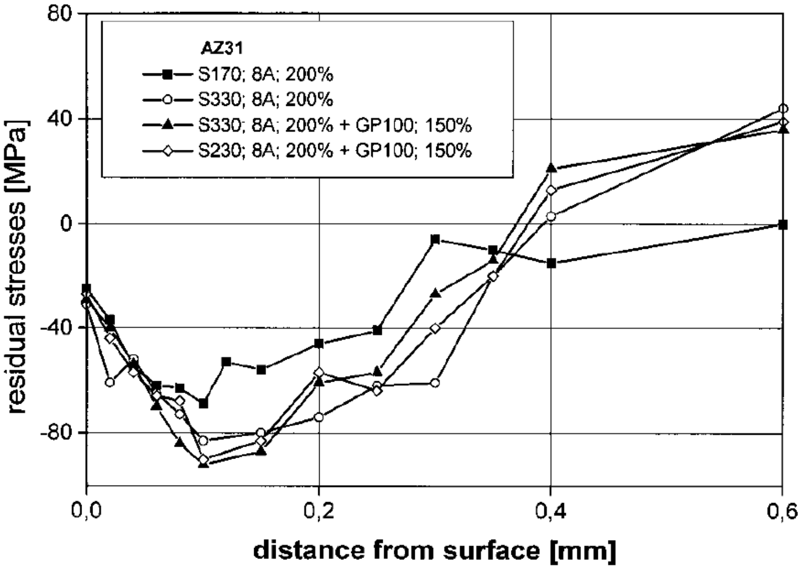

Figure 24- Residual Stress Distribution of Shot Peened AZ31 for Different Shot Peening Treatments [38]

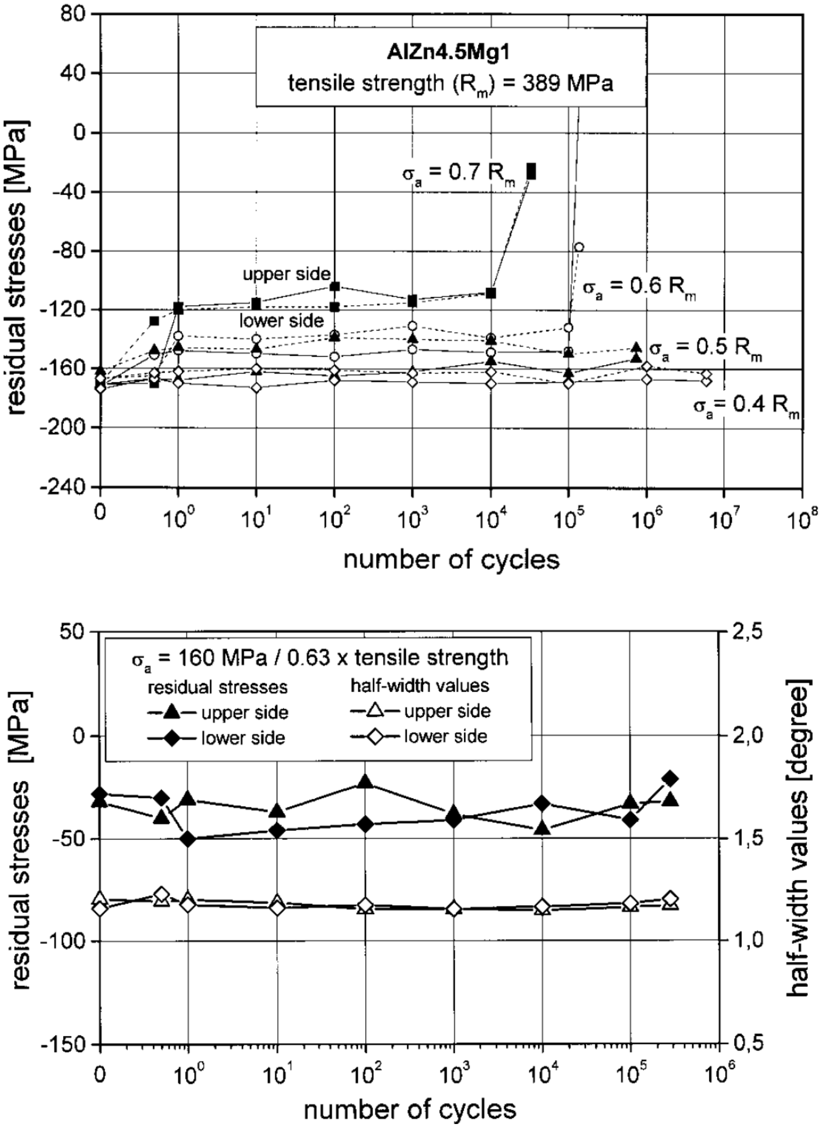

Figure 25- Stress Relaxation in Bending Fatigue Test of AlZn4.5Mg1 and AZ31 [38]

The influence of shot peening and corrosion on the fatigue strength of magnesium die-cast alloy AZ91hp has been investigated by Dindorf and Muller [42]. They have shot peened the specimens in two stages, first by ferritic shots and then by glass beads. They have then applied corrosion tests on both specimens and finally have tested uncorroded and corroded specimens using a rotating bending machine. The result of the tests show that ferritic shot peened specimens have almost the same fatigue performance of the specimens with ferritic and glass bead shot peening but corrosion has decreased fatigue performance drastically (figure 26).

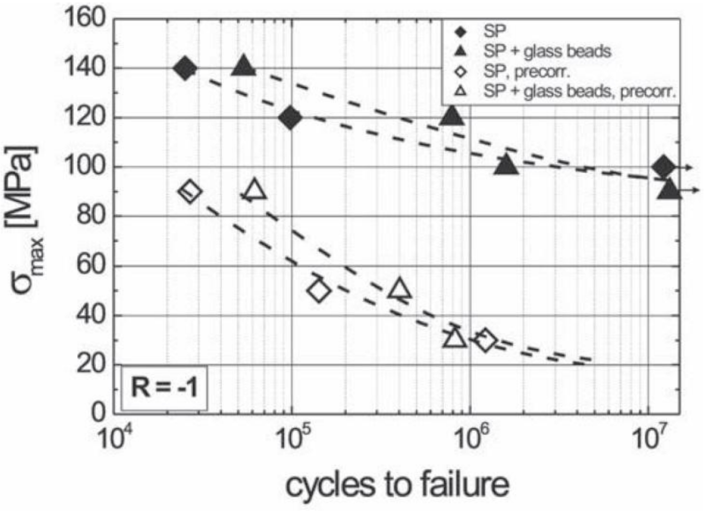

Figure 26- Fatigue Performance of Corroded and Uncorroded Shot Peened Specimens of AZ91 hp [42]

2.4.2 Cold Spray Coating and Fatigue Performance

Price et al. [39] have investigated the effect of cold spray coating on fatigue strength of titanium alloy Ti6Al4V. They have deposited pure titanium on as received and grit blasted Ti6Al4V substrate. The fatigue endurance limit in all states of as received, grit blasted, as received and coated, and grit blasted and coated, has been measured by rotating bending machine and by using the step loading method. The result of the tests show that cold spray coating has improved fatigue performance of as received substrate and reduced the fatigue endurance limit by 15% while no remarkable improvement for grit blasted specimens is observed (Table 9). It has been concluded that low compressive residual stresses due to cold spray coating, especially in grit blasted substrates is the reason for these results.

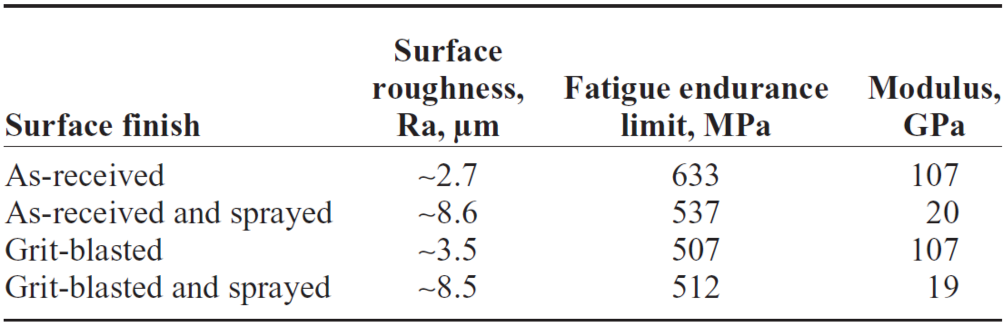

Surface finish	Surface roughness, Ra, µm	Fatigue endurance limit, MPa	Modulus, GPa
As-received	~2.7	633	107
As-received and sprayed	~8.6	537	20
Grit-blasted	~3.5	507	107
Grit-blasted and sprayed	~8.5	512	19

Table 9- Fatigue Endurance Limit of Titanium Alloy Ti6Al4V Before and After Deposition of Pure Titanium Using Cold Spray Coating [39]

Jeong and Ha [41] have investigated the effect of cold spray of Al-Si powder on aluminum alloy A356. Their results show more than 200% improvement in high cycle fatigue life after cold spray coating (Figure 27).

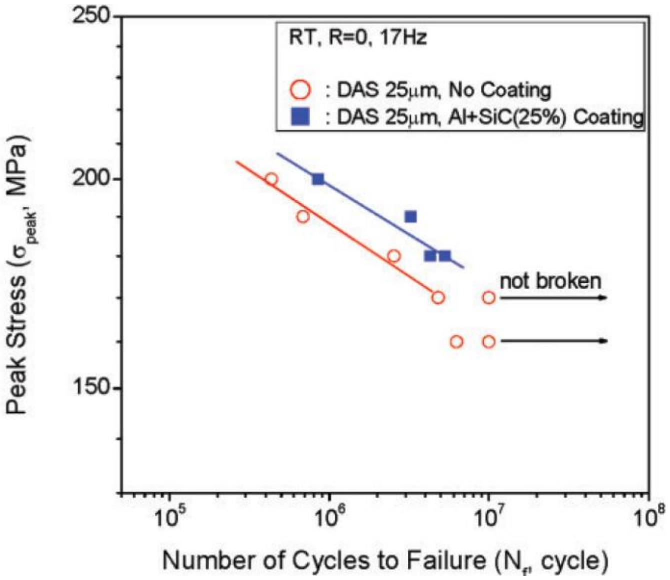

Figure 27- High Cycle Fatigue Performance of Coated and Uncoated A356 [41]

To study the effect of cold spray coating on fatigue life, Sansoucy et al. [40] have used the cold spray coating process to deposit gas atomized particles of Al-13Co-26Ce alloy on aluminum alloy AA 2024-T3 specimen. They have used bending fatigue tests to compare fatigue performance of coated specimens with bare and Alclad specimens. The results of the tests show a better fatigue performance of cold sprayed specimens, especially in lower levels of stress. As figure 28 shows the fatigue performance of cold spray coated specimens is improved over an order of magnitude compared to bare and Alclad specimens. This fatigue strength improvement has been related to compressive residual stress induced by cold spray coating. During the test, the deposition shows a strong bonding and no delamination of coating from substrate is observed.

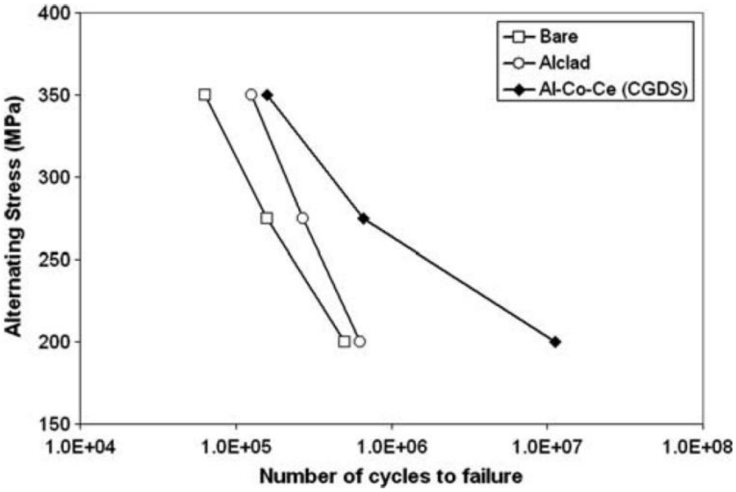

Figure 28- Fatigue Performance of the Bare, Alclad, and Cold sprayed Al-13Co-26Ce Coating on AA 2024-T3 Specimens [40]

Section Summary

- Considering the similarity between shot peening and cold spray coating, the literature of both processes and their influence on fatigue strength has been reviewed.
- Both aluminum and magnesium alloys show better fatigue performance after shot peening. The differences are that the improvement in aluminum alloys is saturated at a level of Almen intensity while magnesium alloys are sensitive to Almen intensity. After a level of shot peening intensity a sharp decrease of fatigue performance due to severe shot peening is observed in magnesium alloys.
- Very limited number of works has been done on the study of the influence of cold spray coating on fatigue life of metallic components. While one study reports no remarkable improvement of fatigue strength after cold spray coating on titanium, more research shows that cold spray coating can improve high cycle fatigue life of aluminum alloys.
- Increasing demand for using wrought magnesium alloys as structural members in automotive, aerospace, and other industries, combined with cold spray coating as an emerging method for corrosion protection, requires the need for investigation of the effect of cold pray coating on the fatigue performance of wrought magnesium alloys such as AZ31B.

Chapter 3 Residual Stress Evaluation

The residual stress induced by cold spray coating has been evaluated by comparing FEM results to experimental tests. In this chapter the details of FEM models, material properties used, and the assumptions for the analysis have been described and the results have been presented. The experimental process and results have been shown and compared to FEM results.

3.1 Simulation of the Residual Stress Induced by Cold Spray Coating

3.1.1 Selection of FEA Software

In this work, coating of Aluminum alloy series 1100 on AZ31B substrate has been considered. Centerline Ltd. has provided the coating services and the related information. Based on the data received from Centerline, average particle diameter is 40 µm and the particle velocity is 400 m/s.

Simulation of the process of cold spray coating on Magnesium alloy AZ31B has all the aspects of nonlinearity and is therefore very challenging. First of all, there is material nonlinearity since magnesium alloys have post yield nonlinear behaviour as discussed in 1.1.6 and will be shown in more details in this section. In addition the contact between particles and substrate needs a nonlinear simulation. Finally the simulation includes high rate plastic deformation of particles and the substrate.

Consideration of the high velocity of the particles and the high rate of plastic deformation in a very short time, led us to use an explicit FEA package. At first to make the problem easier, cold spray coating of aluminum particles on aluminum substrate was tried. For this purpose, Abaqus Explicit 6.7 was used and the impact of a single particle of diameter 40 µm on aluminum substrate with the dimensions of 150µm x 150µm x 150 µm was simulated. It was then attempted to define AZ31B material properties using Abaqus 6.7 Explicit but this package did not include the needed material model. As will be shown in this chapter, AZ31B is isotropic in elastic region while it shows anisotropic and asymmetric behaviour after its yield point. The closest material model that has been offered by Abaqus 6.7 is Hill's anisotropic model that cannot cover all the aspects of AZ31 behaviour [46]. Although this material model is anisotropic, it assumes the material to be symmetric, having the same behaviour in tension and compression, which is not true about AZ31. In addition, Abaqus does not let the user define different curves for the material behaviour in different directions. It only differentiates yield points and accepts one curve to define post yield behaviour for all directions. This is another limitation of using Abaqus 6.7 Explicit and its anisotropic material model for this work, since post yield curves of AZ31 behaviour are considerably different and cannot be defined by one curve. All these issues directed us to select another FEM package for the simulation.

The second choice that was considered was LS-DYNA. As an explicit package it seemed suitable for this purpose but there was issue with the material model. LS-DYNA material model number 124, tension-compression plasticity, was the closest model to our application [47]. This material model can accept asymmetric properties with different stress-strain curves in tension and compression but it did not include anisotropic properties. This was a main shortage for definition of AZ31B material properties.

Finally the decision was made to neglect the computation time of simulation of explicit packages and select a package that can simulate the material properties more accurately, even if it is implicit. With this criterion, the best FEM software that could be selected was ANSYS classic package. This package includes the generalized Hill's anisotropic model and can accommodate both anisotropic and asymmetric material properties [44]. However there are two disadvantages for selecting this FEM code. The first disadvantage is that stress-strain curves should be defined to be bilinear. Secondly the run time for simulation is not as fast as an explicit package and there is also the risk of a non converging solution that needs more accurate definition of parameters and smaller time steps. Regardless, implicit packages offer more accurate solutions than explicit codes and thus can justify the difficulties of using them. In sum, consideration for the most accurate material model that matches to application and the accuracy of the implicit solution convinced us to use ANSYS classic code for simulating the process of cold spray coating.

3.1.2 Material Model

The anisotropic material model of ANSYS provides all the options for specifying the anisotropic and asymmetric properties. To define elasto-plastic material properties of an anisotropic-asymmetric material like AZ31B to ANSYS, the user needs to have material behaviours in both elastic and plastic regions. In this section the material properties that have been used for the simulation are elaborated.

As elastic properties, the following data should be defined in ANSYS:

Modulus of elasticity, E, in different directions

Poisson Ratio, PR, in different directions

Shear modulus, G, in different directions

As the results of the test by Albinmousa et al [3] show, the modulus of elasticity in different directions is close and therefore AZ31 can be considered isotropic in the elastic region. Figure 29 shows the ANSYS table for the elastic material properties and the data obtained from Albinmousa et al tests [3].

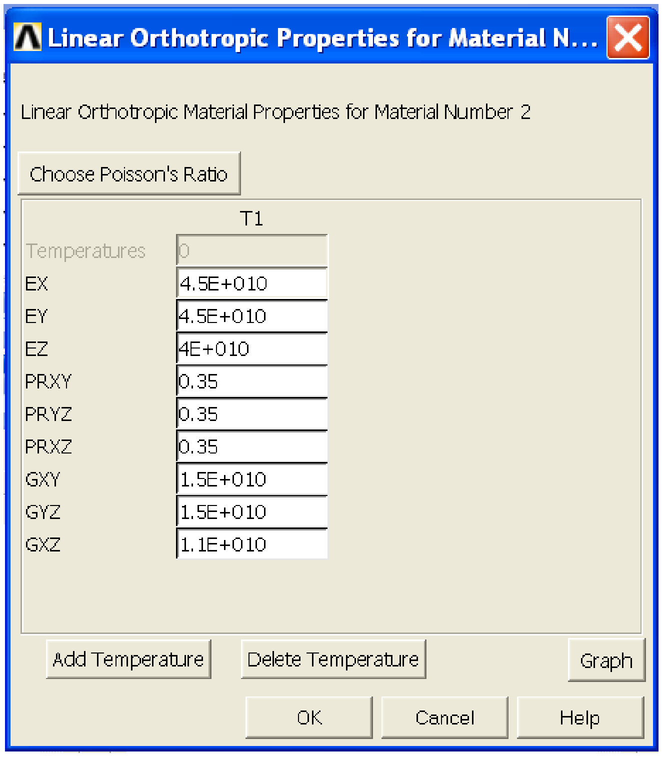

Linear Orthotropic Material Properties for Material Number 2

	T1
Temperatures	0
EX	4.5E+010
EY	4.5E+010
EZ	4E+010
PRXY	0.35
PRYZ	0.35
PRXZ	0.35
GXY	1.5E+010
GYZ	1.5E+010
GXZ	1.1E+010

Figure 29- Linear Orthotropic Material Properties of AZ31B

Post yield material properties are more complicated. Figure 30 shows the material constants that should be defined for the ANSYS anisotropic material model [44].

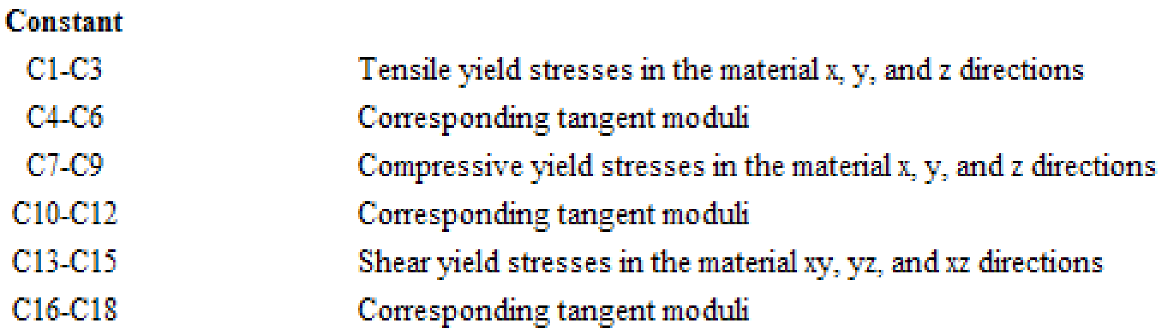

Constant	
C1-C3	Tensile yield stresses in the material x, y, and z directions
C4-C6	Corresponding tangent moduli
C7-C9	Compressive yield stresses in the material x, y, and z directions
C10-C12	Corresponding tangent moduli
C13-C15	Shear yield stresses in the material xy, yz, and xz directions
C16-C18	Corresponding tangent moduli

Figure 30- Material Constants of ANSYS Anisotropic Material Models [44]

The coordinate system that has been used in the simulation is as follows:

X → Extrusion direction, ED
Y → Thickness Direction, THD
Z → Transverse Direction, TD

Considering the conversion between the ANSYS coordinate system and the material extrusion direction, Albinmousa et al results [3] provide the material constants provided in table 10.

		Yield Stress ED (X)	Yield Stress THD (Y)	Yield Stress TD (Z)
Tension	Yield Stress	C1	C2	C3
	Et	C4	C5	C6
Compression	Yield Stress	C7	C8	C9
	Et	C10	C11	C12
Torsion	Yield Stress	C13	C14	C15
	Et	C16	C17	C18

🟩	Determined by [3]
	Not Determined by [3]

Table10- Material Properties Constants Provided by Albinmousa et al. [3]

As this table shows, all the material properties in THD and also torsion properties in TD needed to be determined. For this purpose two complimentary actions were taken: implementing more tests on AZ31 in THD and using the ANSYS consistency equation.
To prepare more material properties, two more tests were applied on AZ31; compression test in THD and torsion test in TD. Figures 31 and 32 show specimen used in THD compression test and the results.

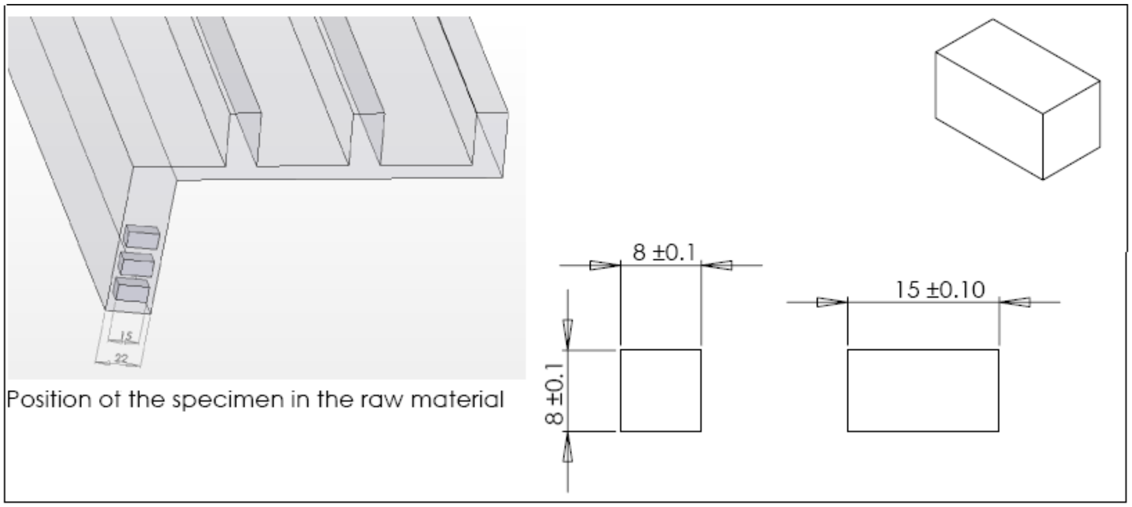

Figure 31- Extrusion Piece (left) and Compression Test Specimen, AZ31, THD

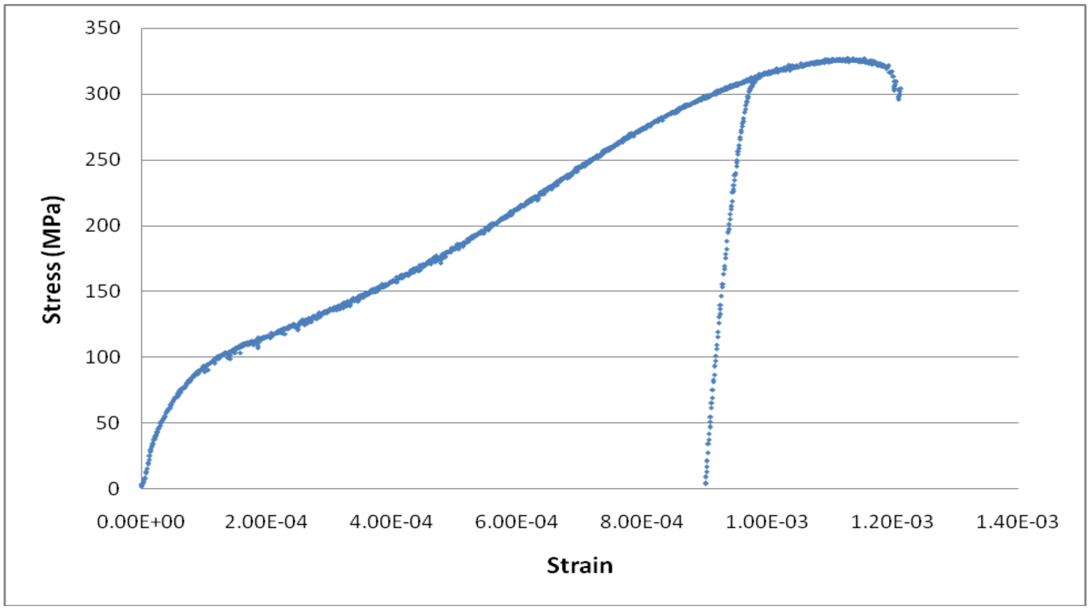

Figure 32- Compression Test Result, AZ31, THD

Figures 33 and 34 show the specimen and the results of torsion test in TD.

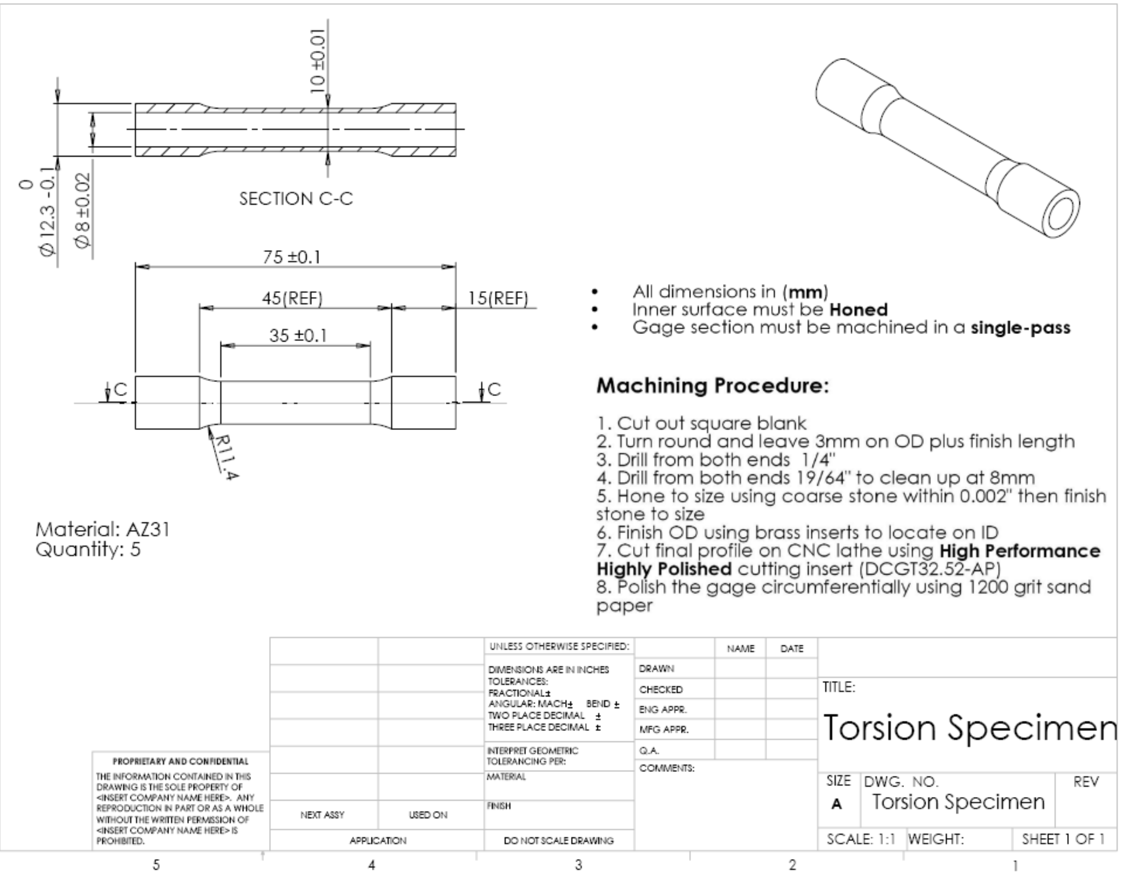

- All dimensions in **(mm)**
- Inner surface must be **Honed**
- Gage section must be machined in a **single-pass**

Machining Procedure:

1. Cut out square blank
2. Turn round and leave 3mm on OD plus finish length
3. Drill from both ends 1/4"
4. Drill from both ends 19/64" to clean up at 8mm
5. Hone to size using coarse stone within 0.002" then finish stone to size
6. Finish OD using brass inserts to locate on ID
7. Cut final profile on CNC lathe using **High Performance Highly Polished** cutting insert (DCGT32.52-AP)
8. Polish the gage circumferentially using 1200 grit sand paper

Figure 33- Torsion Specimen, AZ31, TD

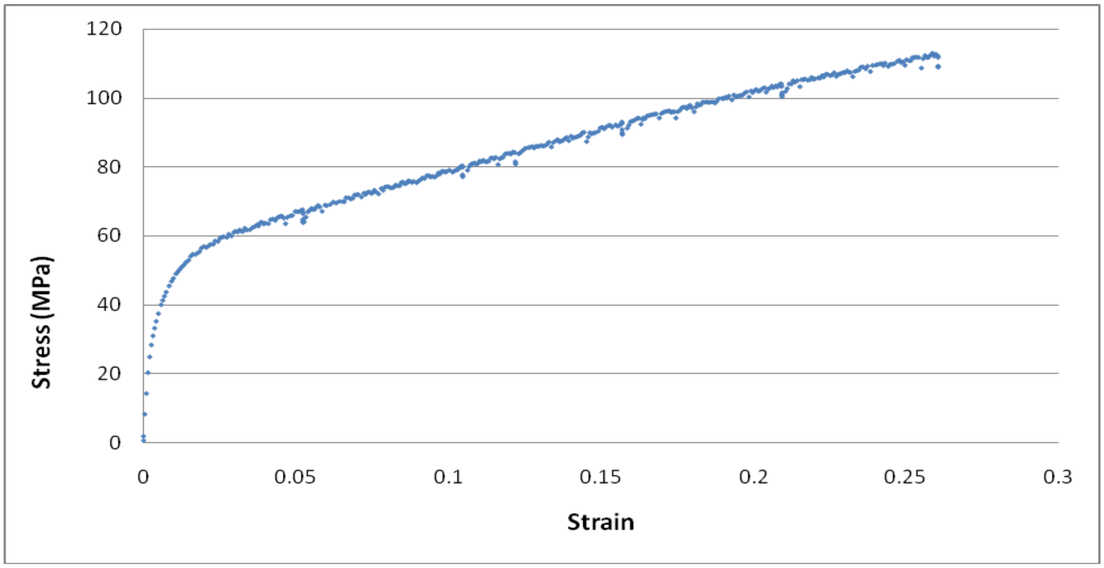

Figure 34- Torsion Test Result, AZ31, TD

These two tests provide the following data:

Compression, THD	**Torsion, TD**
E = 45 GPa	G = 15 GPa
Yield Stress = 50 MPa	Yield Stress = 40 MPa
Et = 2.67 GPa	Et = 320 MPa

These material properties provided material constants C8, C11, C15 and C18.

In the next step, the ANSYS consistency equation was used to determine another unknown material constant, C2. In the ANSYS anisotropic model, uniaxial yield stresses are not completely independent and must satisfy the consistency equation due to the requirements of plastic incompressibility[44]. This equation is:

$$\frac{\sigma_{+x} - \sigma_{-x}}{\sigma_{+x}\sigma_{-x}} + \frac{\sigma_{+y} - \sigma_{-y}}{\sigma_{+y}\sigma_{-y}} + \frac{\sigma_{+z} - \sigma_{-z}}{\sigma_{+z}\sigma_{-z}} = 0 \qquad (1)$$

The only unknown data in this equation is σ+z that can be calculated knowing other parameters from [3] and the test results. This provides material constant C2. The only yield point that in unknown is C14 which has been assumed to be in the range of C13 and C15.

As mentioned before, the ANSYS anistropic model accepts a bilinear material model. It means that the post yield stress-strain curve must be approximated by a line. For this purpose a line has been fitted to the post yield curve to minimize the error. The slope of this line has been considered as Et for each curve and provides the material constants related to the tangent modulus: C4,C6,C10,C11,C12,C16 and C18. Finally by assuming C5 and C17, that are the only remaining unknowns, the material properties needed for the anistropic plastic model of ANSYS is determined. Figure 35 shows the ANSYS table of the parameters defined for the plastic anistropic model.

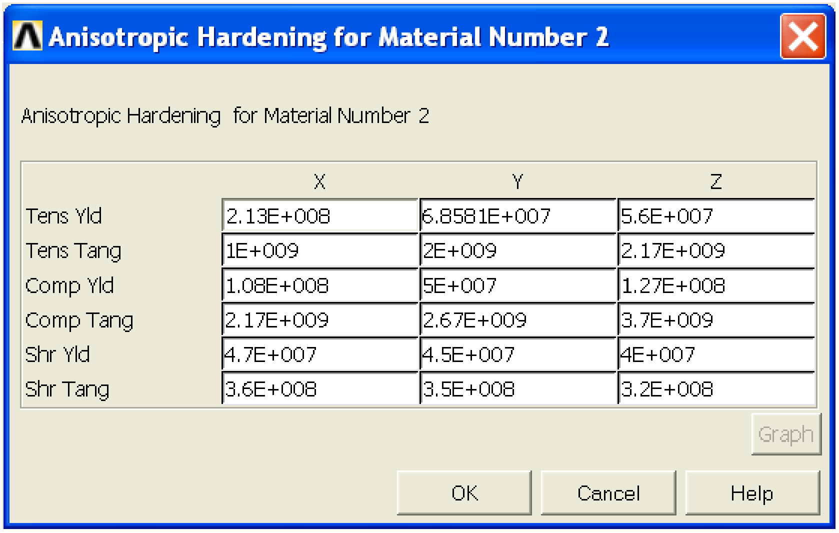

Anisotropic Hardening for Material Number 2

	X	Y	Z
Tens Yld	2.13E+008	6.8581E+007	5.6E+007
Tens Tang	1E+009	2E+009	2.17E+009
Comp Yld	1.08E+008	5E+007	1.27E+008
Comp Tang	2.17E+009	2.67E+009	3.7E+009
Shr Yld	4.7E+007	4.5E+007	4E+007
Shr Tang	3.6E+008	3.5E+008	3.2E+008

Figure 35- Plastic Anisotropic Material Parameters (All Values in Pa)

Before applying this model to the simulation of cold spray coating, it was tested on a simplified model. Figure 36 shows a simple block that this material model was applied to. Then uniaxial stresses in ED (X) and TD (Z) directions were applied to it and the related strains were determined. Figures 37a and b show the actual curve, simplified curve, and the FEM results. This test showed that the model worked accurately since the results follow the stress-strain curve as load changes. Therefore the model is reliable for the simulation.

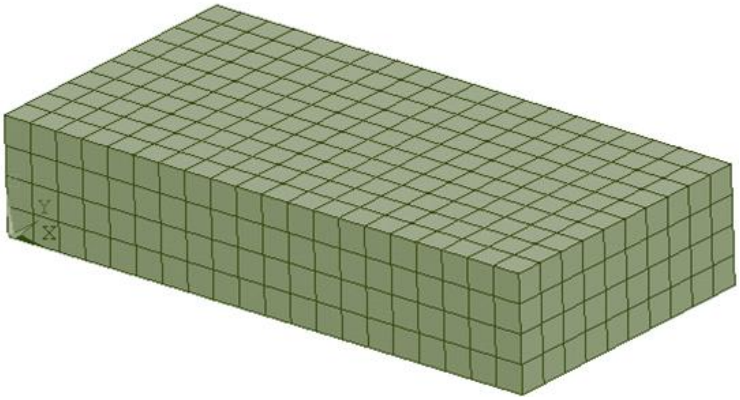

Figure 36- Model Used for Material Model Verification

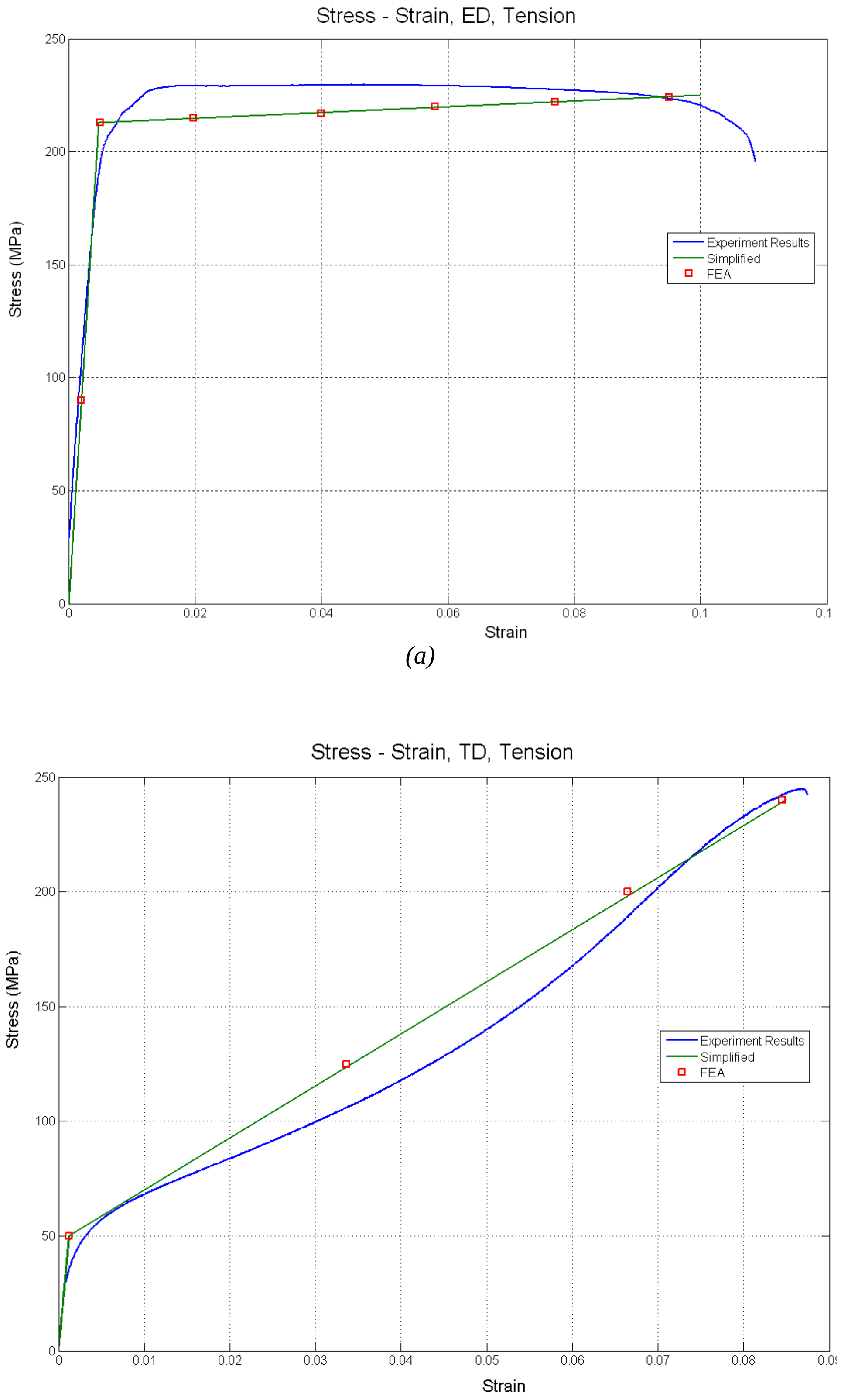

(a)

(b)

Figure 37- Comparison of Material Properties and FEA Results, Uniaxial Tensile Load for a) ED,

b) TD

3.1.3 Simulation Models and Solution Parameters

Three different models with single, 13 and 41 particles have been used for the simulation. Considering the symmetry, in all simulations, a quarter of the model was discretized, in order to reduce computation time. Particle velocity is 400 m/s in all three models, based on the information from centerline. In section 2.1.5 where the effect of velocity has been studied, simulations with the velocities of 500 m/s and 600m/s for single particle model have been presented.

Since the oxide layer is removed from the surface of particle and substrate due to the impact and the large surface deformation [13], the oxide layer hasn't simulated.

In all models, node to surface contact with a penalty contact algorithm has been used. Normal penalty stiffness factor has been considered equal to 1 and is the default of the package. Using KEYOPT(10)=2, contact stiffness is updated in each iteration to obtain more accuracy. Penetration tolerance has been taken as 0.1 and a friction coefficient equal to 0.1 has been considered.[44]

The first model simulates the impingement of a single particle on the substrate. Figure 38 shows the model. Based on the information received from Centerline, particle diameter is 40 µm. After several trial runs, substrate dimensions have been selected as 7Rx6Rx6R, where R is particle radius, equal to 280µm x 240µmx 240µm to eliminate the boundary effects.

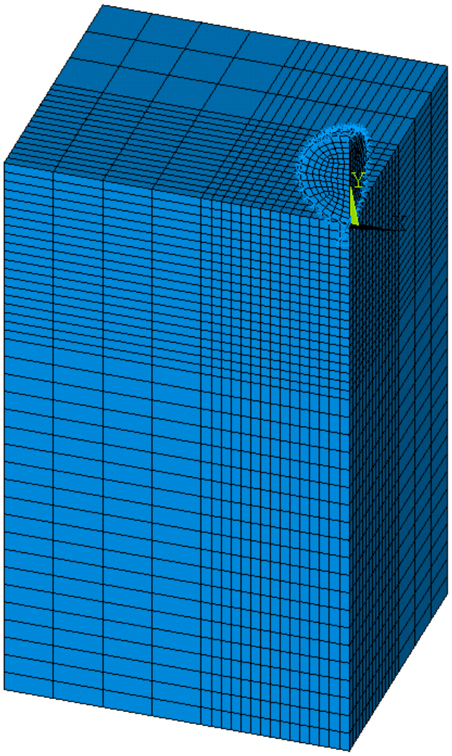

Figure 38- A Quarter of Single Particle Model

To achieve more accuracy, hexagonal elements have been used in the substrate model. Particle elements are 8 nodes structural element of Solid185. Elements that can be used for the substrate are more limited because of anisotropic material properties of the substrate [44]. For particle, 8-node solid45 elements have been used. After several trial runs, mesh size was selected as follows:

Particle: 5µm
Substrate, at contact area: 4µm
Substrate, under impact area: 8µm
Substrate, regions far from impact: 24µm

To study the effect of residual stress from adjacent particle impacts, two more models with multiple particles were developed as well. Figures 39 and 40 show a quarter of the models with 13 and 41 particles. All simulation parameters for these models are the same as the single particle model.

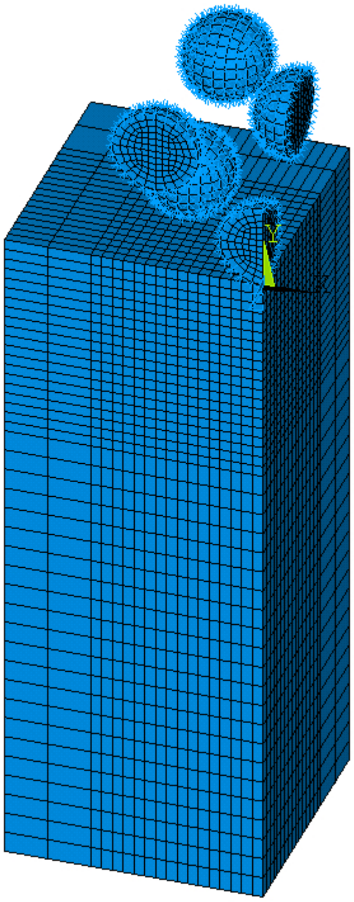

Figure 39- A Quarter of Thirteen Particle Model

In the 13 and 41 particle models, particles impinge the substrate in several layers with no interference between two subsequent layers. Figures 41 and 42 show the arrangement of the particles in the 41 particle model. The number on each particle shows the layer number.

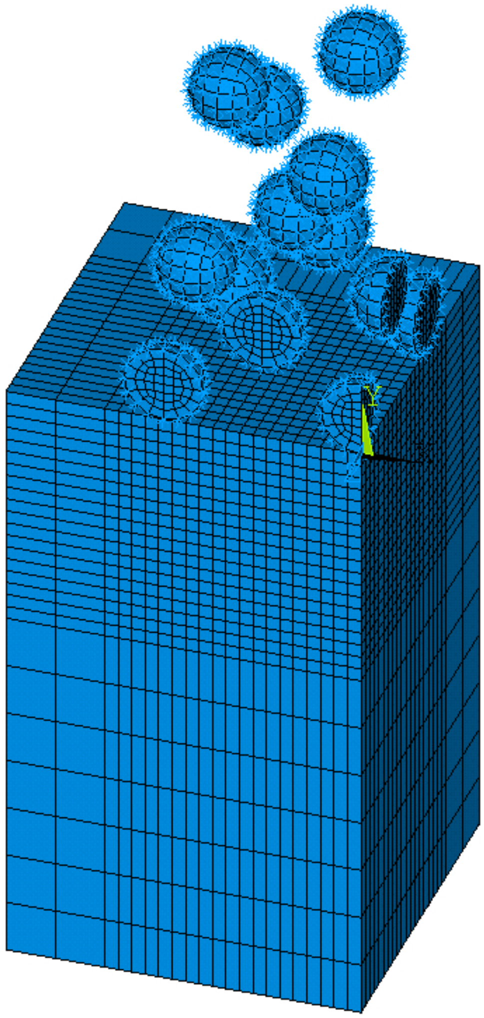

Figure 40- A Quarter of Forty One Particle Model

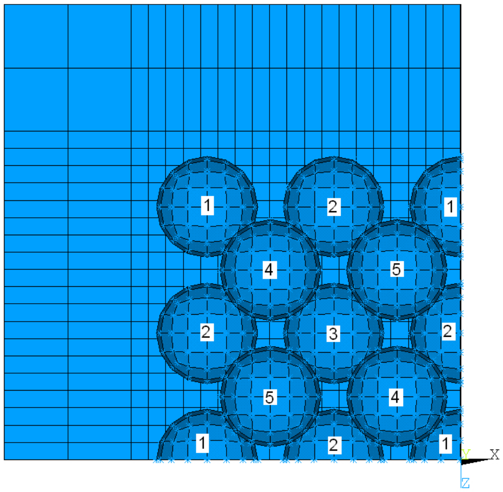

Figure 41- Forty One Particle Model with Five Group of Particles in Different Layers

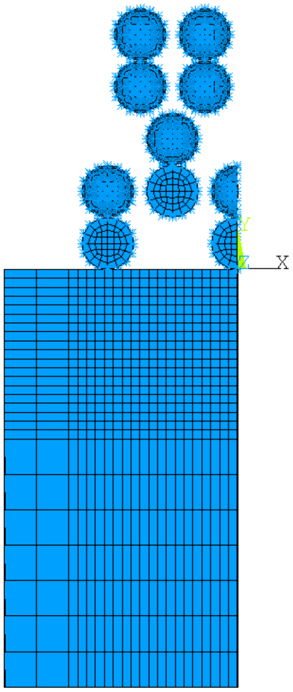

Figure 42- Level Difference of the Particle Layers Equals to Particle Diameter

An important phenomenon that must be considered in this simulation is the stress waves that appear due to the impact of particles on the substrate. These stress waves spread and oscillate in the substrate in three directions and change the magnitude of stress in each element even after the impingement is complete. Since this wave moves in the substrate with the velocity of sound, the results of stress in each element changes every instant based on the value of the stress wave in it. To achieve accurate residual stress distribution, this stress wave must be filtered from the results. There are several approaches to fulfill this. One approach is using infinite elements on the boundaries of the substrate so that the stress wave does not reflect inside the model. Abaqus6.7 does provide structural infinite elements that can be used for this purpose [47], but this application is limited to electromagnetic models in ANSYS. The second approach is applying a damping effect in the simulation. ANSYS provides six categories of damping effects and three of them are applicable to our full transient simulation. These three categories are:

a- Alpha and Beta damping: defines mass and stiffness matrix multipliers for damping effect

b- Material dependent damping: damping is defined as a part of material definition

c- Element damping: some elements are used to apply damping effects

Using this approach requires that the damping behaviour of the material is known and is applied as a multiplier to material properties. Since the needed material data does not exist in the literature, an alternative approach was used in this work. The approach that has been used here is to increase the time of simulation and let the stress wave dissipate through that time. The advantage of this approach is that it doesn't affect the residual stress and the result will be accurate. The disadvantage on the other hand is that computation time is increased. To overcome this issue, the time steps after the impact and in the phase of stress wave damping can be selected to be large to save on computation time. In this work, for all simulations, the time steps during impingement of particle(s) to the substrate have been selected from 0.01 ns to 2 ns to avoid a non-converging solution. After impingement when the stress wave is dissipated, the time steps have been increased to 4 ns. Beyond that the time steps have been increased gradually to 40 ns. The impact time of the particle is around 60 ns as the simulation shows. Depending on the simulation, the solution has been continued up to 30 ms to ensure that the stress wave has been dissipated. To check this, the graph of stress- time has been checked for the elements at the top and the bottom of substrate under the line of impact. Figure 43 shows an example of the dissipation of stress waves vs. time for one simulation. As this figure presents, the magnitude of the stress in the elements is constant after the time of about 30 ms.

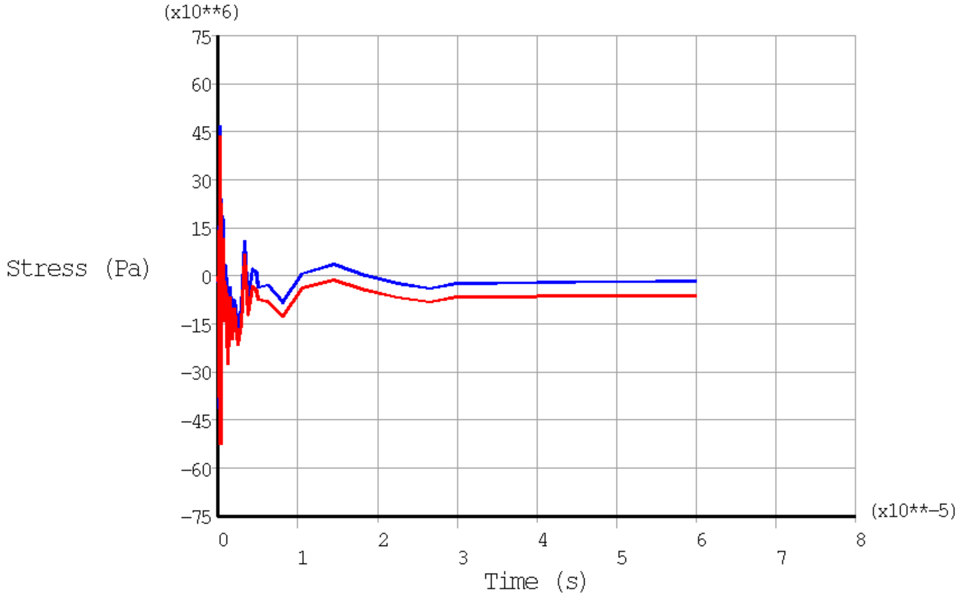

Figure 43- Dissipation of Stress Wave through Time Measured for One Element

3.1.4 Simulation Results

Before discussing the simulation results, it is better to review the residual stress distribution in a shot peened specimen. As discussed in section 1.3, the residual stress induced by shot peening in a substrate with isotropic material properties is shown in figure 44. It starts with compressive residual stress at the surface and at a certain depth there will be maximum compressive residual stress. Beyond this depth, the magnitude of compressive residual stress decreases to zero and then rises to a maximum tensile stress and then declines toward zero. Simulation of shot peening has shown that this distribution is observed in single shot impact under the impact point [23]. This distribution can be generalized to the entire surface of the substrate if the process covers the entire surfaces evenly.

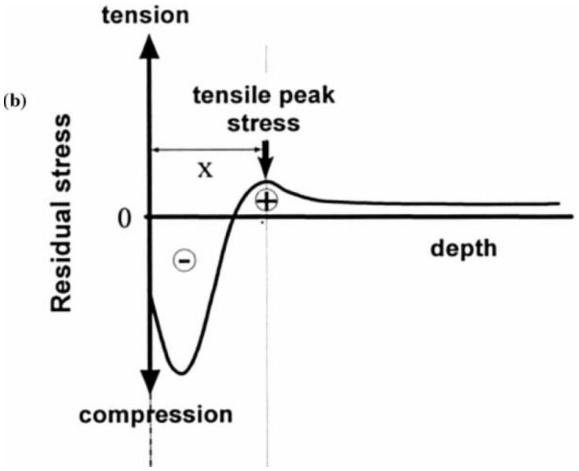

Figure 44- Residual Stress Distribution in a Shot Peened Specimen [36]

Simulation results that are discussed in detail in this section show that there is a considerable difference between the results of residual stress in a substrate with anisotropic material properties, as is in AZ31B, in comparison to what has been reported for isotropic materials. The major difference is that the residual stress on the surface for a single particle model is tensile while the residual stress changes to compressive for a multiple particle simulation. In the other words, the interaction between the stresses induced by adjacent particles can change the distribution and magnitude of the residual stress considerably. For this reason, for an anisotropic material, the result from single particle simulation is not enough and applying a multiple particle simulation is crucial. More details are elaborated in this section.

3.1.4.1 Single Particle Simulation Results

As a starting point, a single particle model with particle velocity of 400 m/s is presented. Using material properties detailed in 2.1.2 and simulation model and parameters detailed in 2.1.3, the residual stress distribution on substrate after 50 ms and stress wave dissipation has been shown in figures 45 and 46. In the model, the particle velocity vector has been defined in the Y direction which is the thickness direction of the substrate Extrusion Direction is presented by X and Z denotes the Transverse Direction, as has been outlined in the material properties definition. Therefore SX is residual stress of ED and SZ shows residual stress of TD.

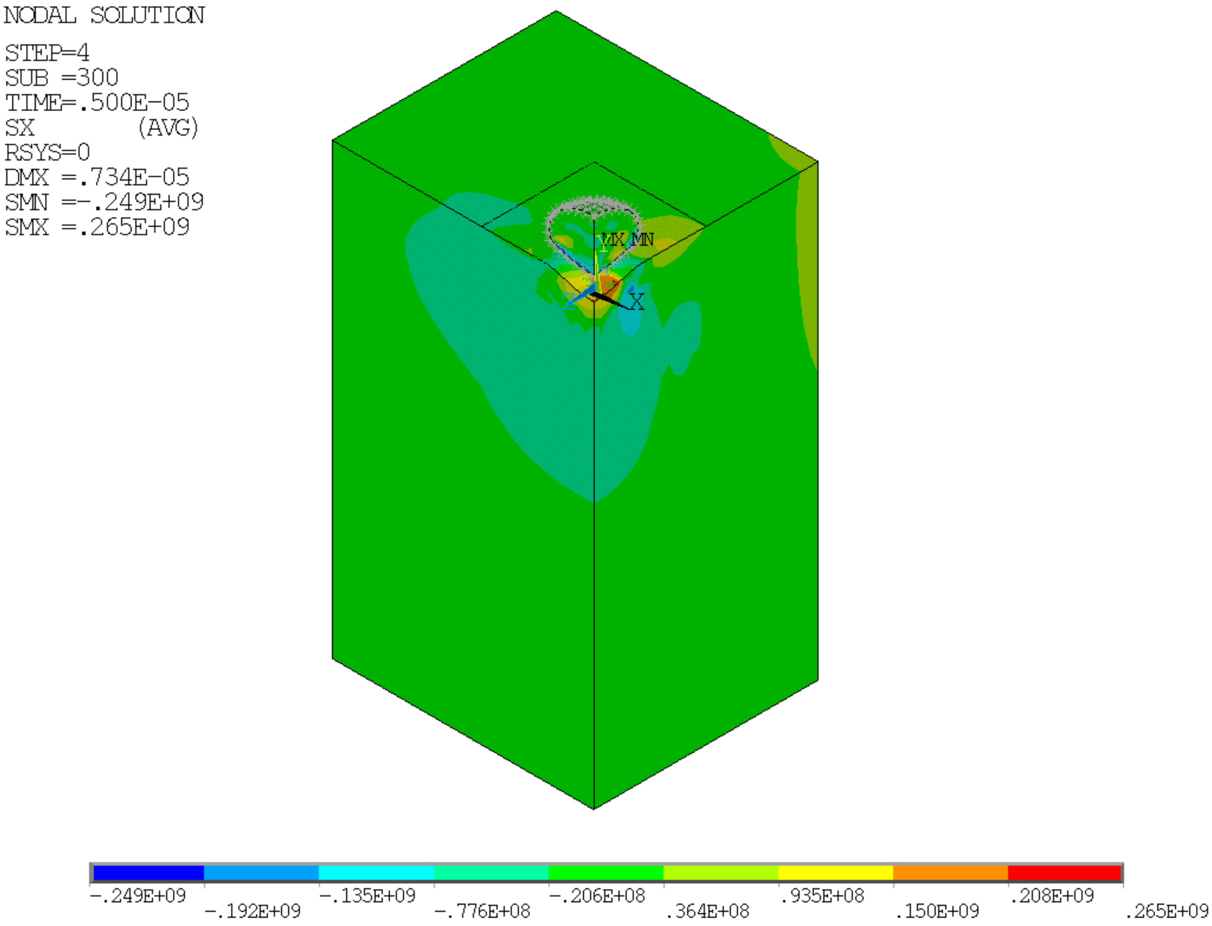

Figure 45- Residual Stress SX, ED, Single Particle

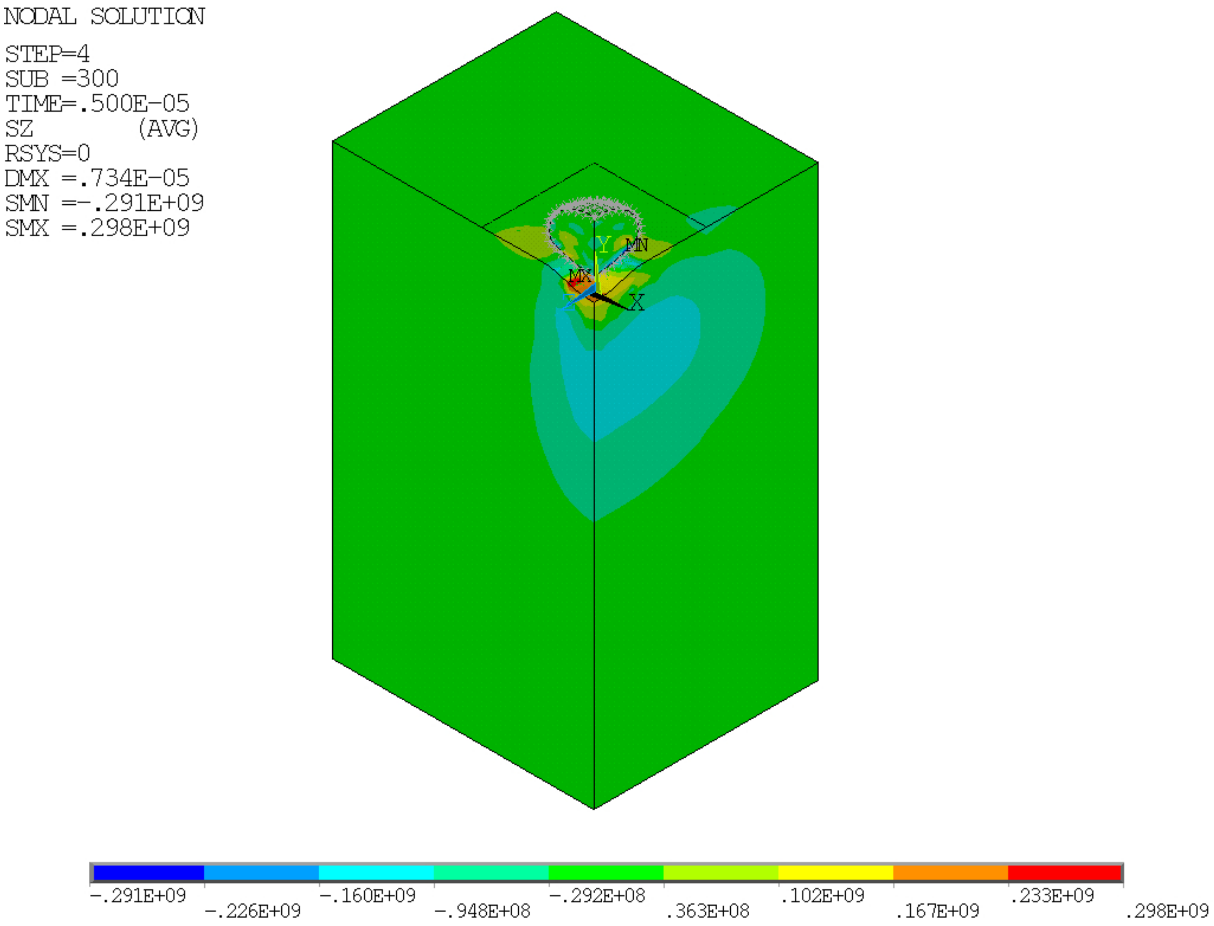

Figure 46- Residual Stress SZ, TD, Single Particle

As shown, residual stress on the surface of the substrate is tensile which changes to compressive in deeper regions, and then diminishes to zero.

Figure 47 shows the top view of the substrate. Point A which is the origin of the coordinate system is the initial contact point of the particle and substrate. Points B, C and D have distance from Point A equal to 8 µm in X and Z directions respectively. Residual stress distributions through depth for the paths that pass through these points have been shown in Figures 48 to 51. The figures show that the residual stress field for the area close to the impingement point is similar.

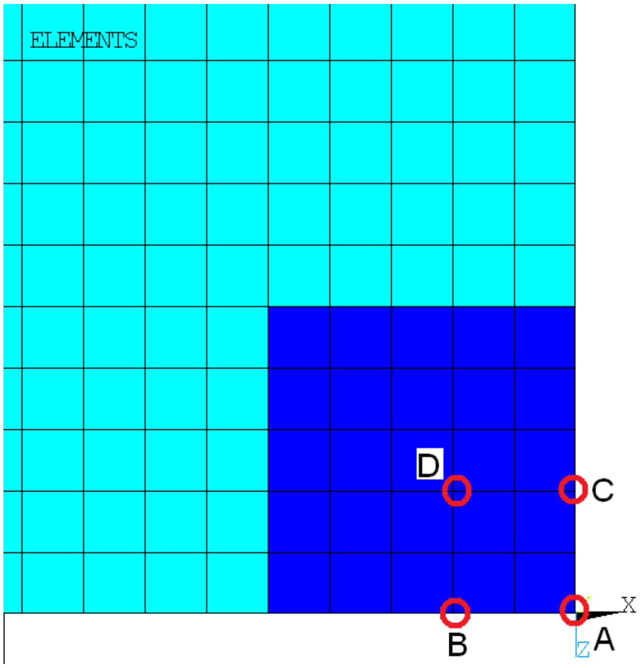

Figure 47- Top View of Measurement Paths

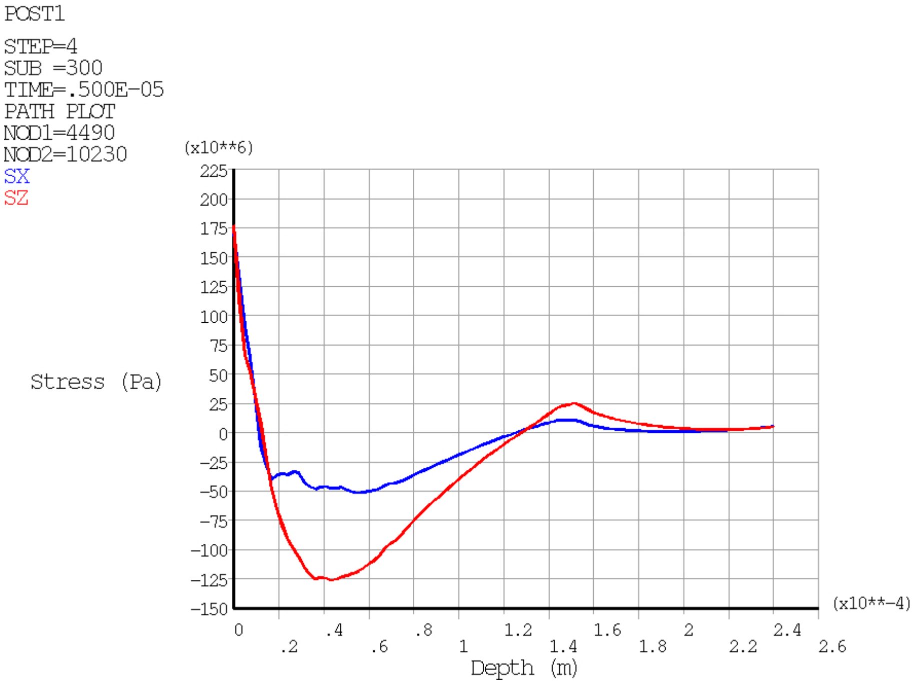

Figure 48- SX and SZ under Impact Point, Point A

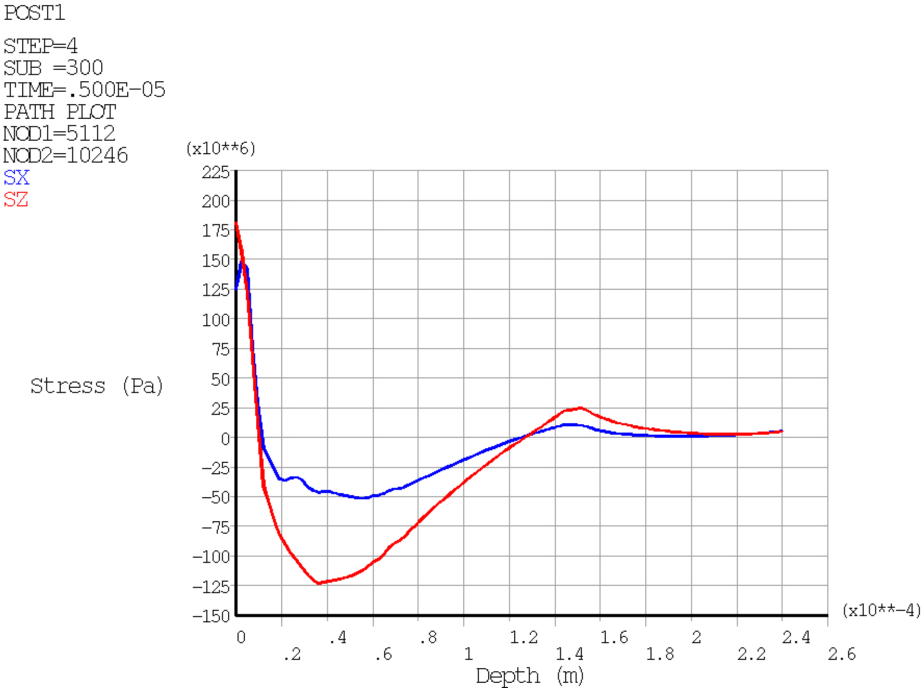

Figure 49- SX and SZ at Path Passing Through Point B, X= 8 µm, Z=0

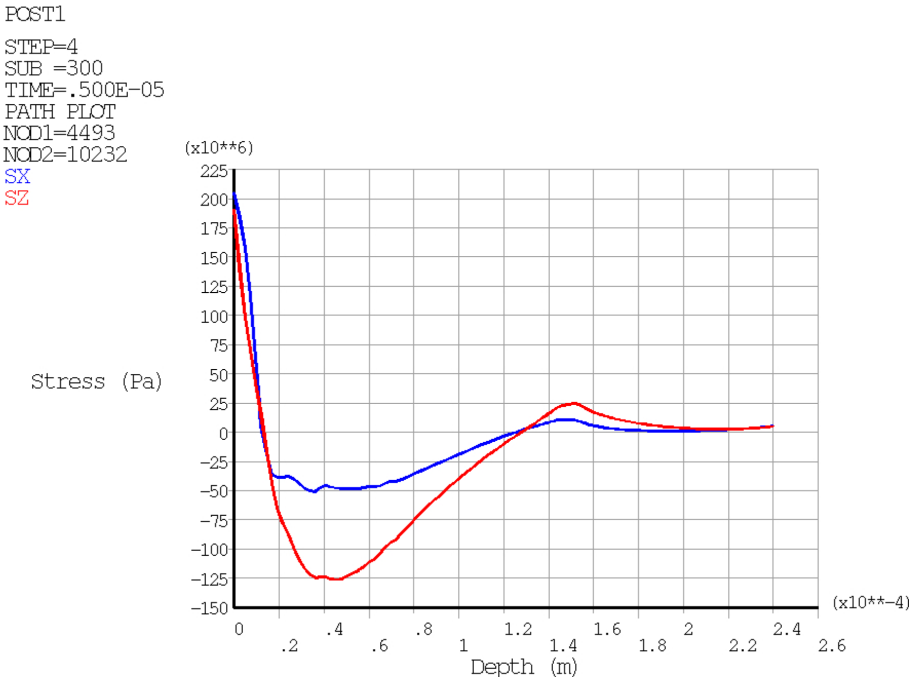

Figure 50- SX and SZ at Path Passing Through Point C, X= 0, Z=8 µm

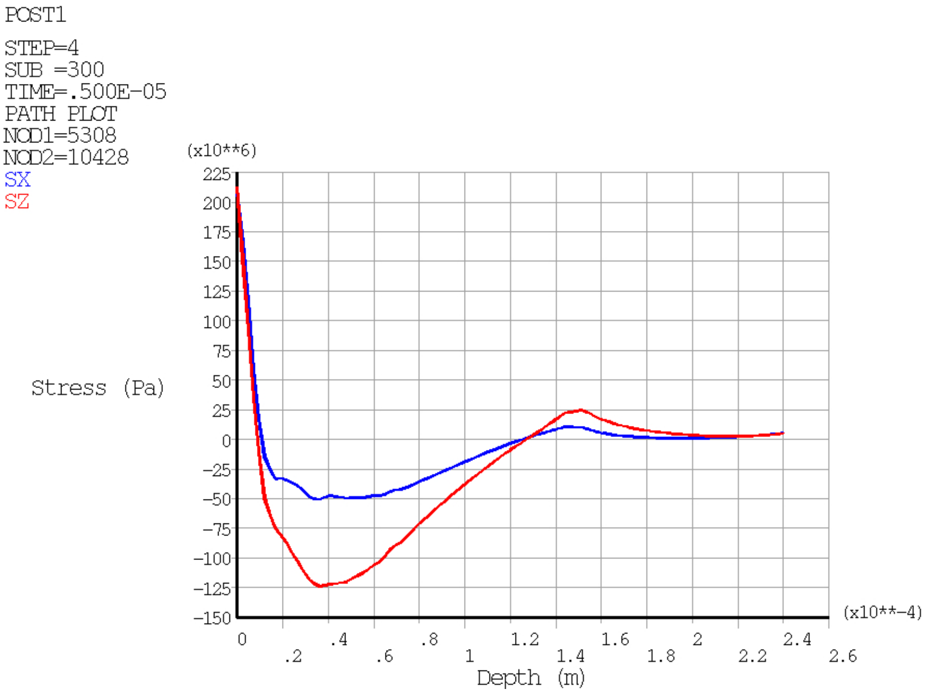

Figure 51- SX and SZ at Path Passing Through Point D, X= 8 µm, Z=8 µm

It is necessary to compare the FEM results to the XRD stress measurements. Therefore FEM results need to be prepared in a way to be comparable to the XRD results. Since in the XRD stress measurement the average of stress over an area is considered as the measurement result, The same approach was employed in the simulation. For this reason, instead of preparing the stress measurement on a path through depth, the average of stress on layers in different depths has been used for preparing stress distribution. Figure 52 presents distribution of SX and SZ though depth obtained by calculating the average of stress on layers of area 25µmx25µm in the quarter model.

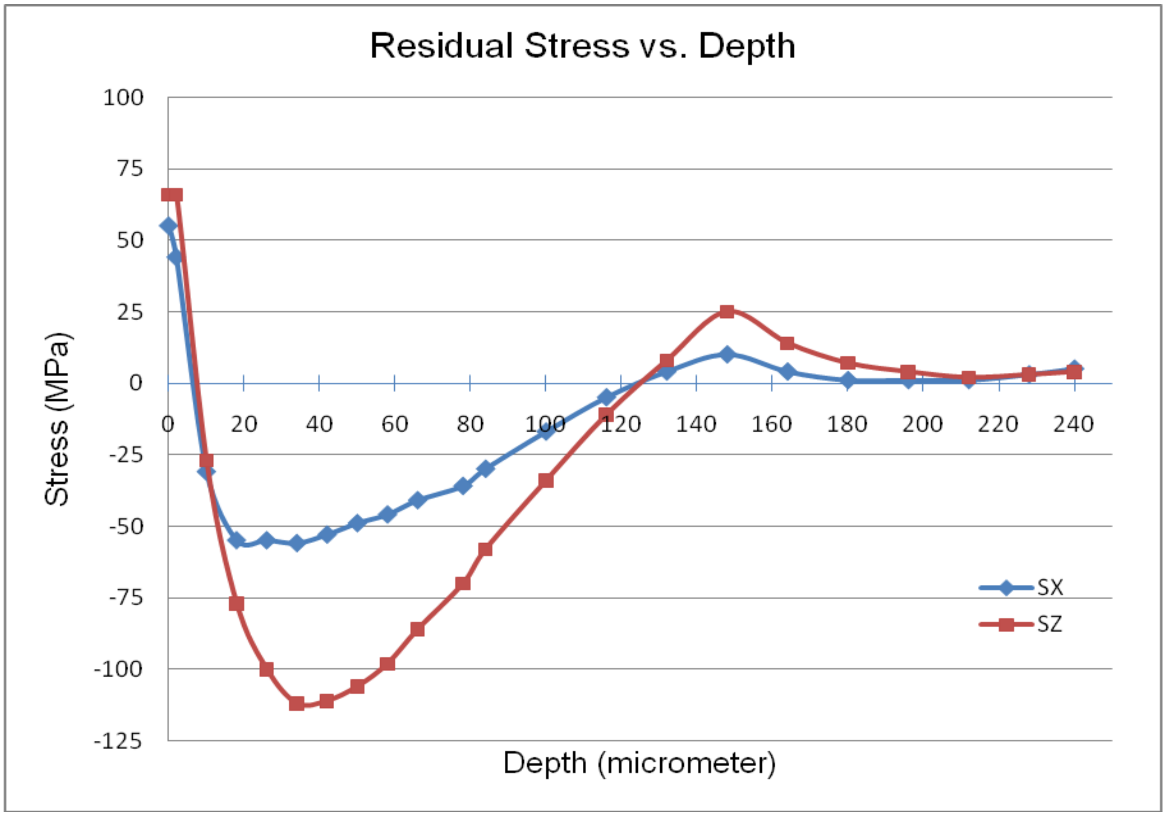

Figure 52- SX and SZ Residual Stress through Depth by Calculating the Average, Single Particle model

As Figure 52 shows, the average residual stress on the surface is tensile with a magnitude of 55 MPa and 66 MPa for SX and SZ respectively. There is a region of compressive residual stress under the surface. For a depth between 20 µm to 70 µm, the average compressive residual stress can be calculated as 50 MPa and 100 MPa for SX and SZ respectively. In this region, SX is almost constant while SZ changes considerably with a maximum of 112 MPa compressive stress.

3.1.4.2 Multiple Particle Simulation Results

Similar to the results of single particle simulation, results for 13 and 41 particle simulations have been prepared. Figure 53 shows the stress profile through depth in the centre of the model for the 13 particle model. Figures 54 and 55 depict the average SX and SZ on area of 50µm x 50µm and 25µm x 25µm on the quarter model respectively. Similarly figures 56 to 58 show the results for the 41 particle model in the centre of the model and also on the area of 100µm x 100µm and 50µm x 50µm.

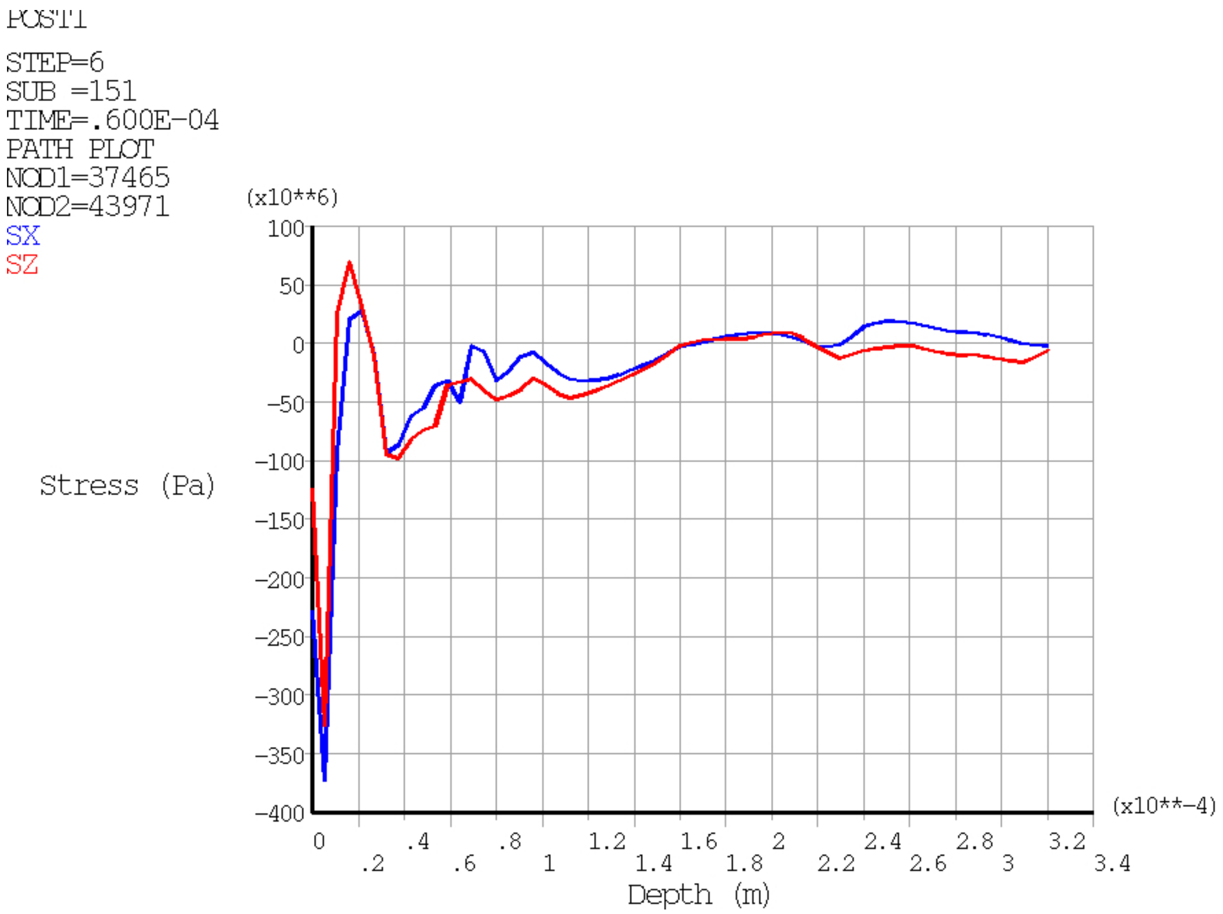

Figure 53- SX and SZ in the Centre of the Model, 13 Particle model

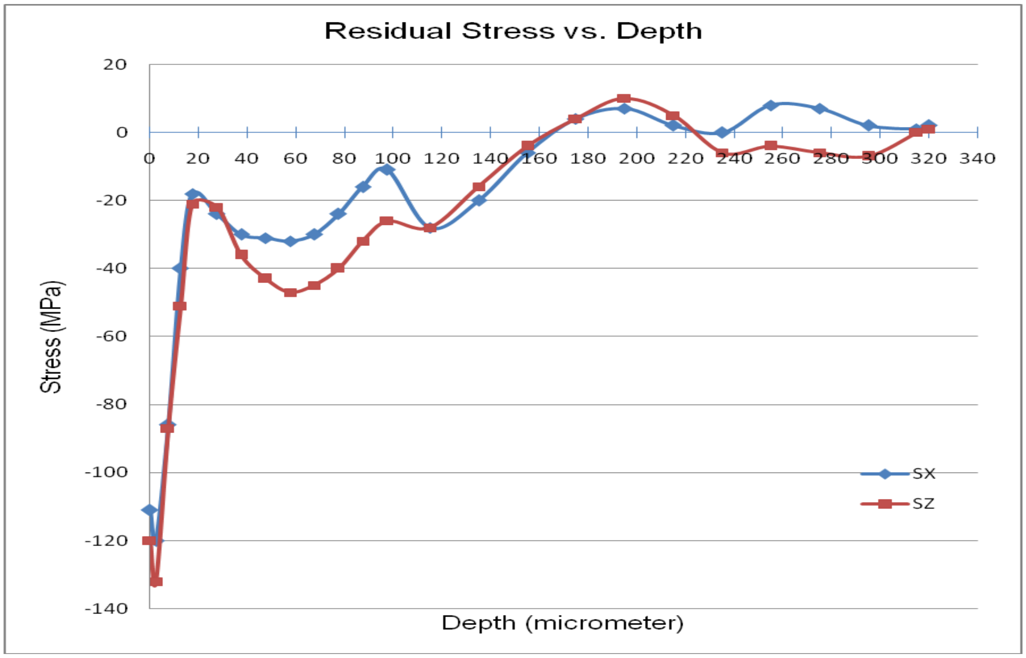

Figure 54- Average SX and SZ on 50μmx50μm Area Through Depth, 13 Particle Model

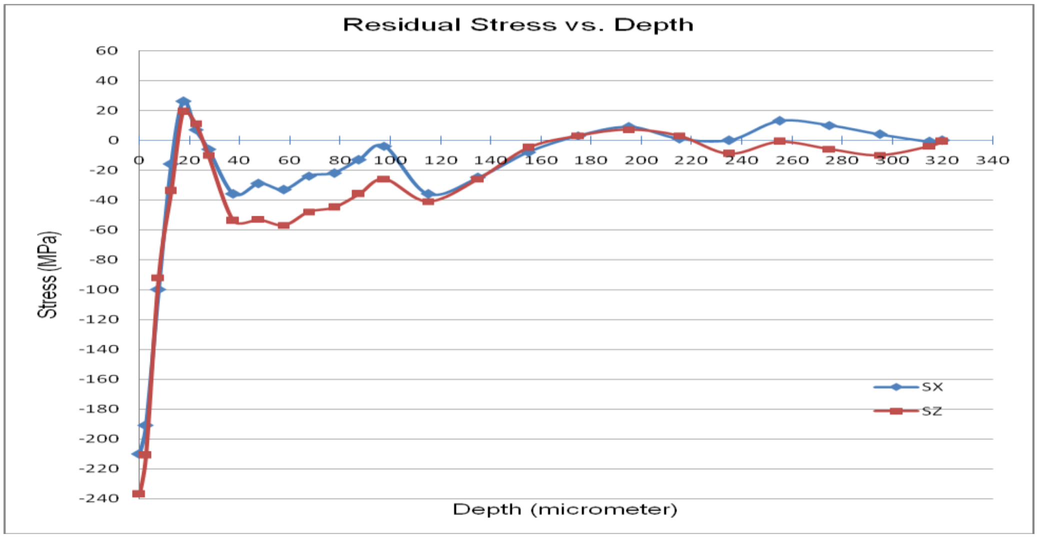

Figure 55   Average SX and SZ on 25μmx25μm Area Through Depth, 13 Particle Model

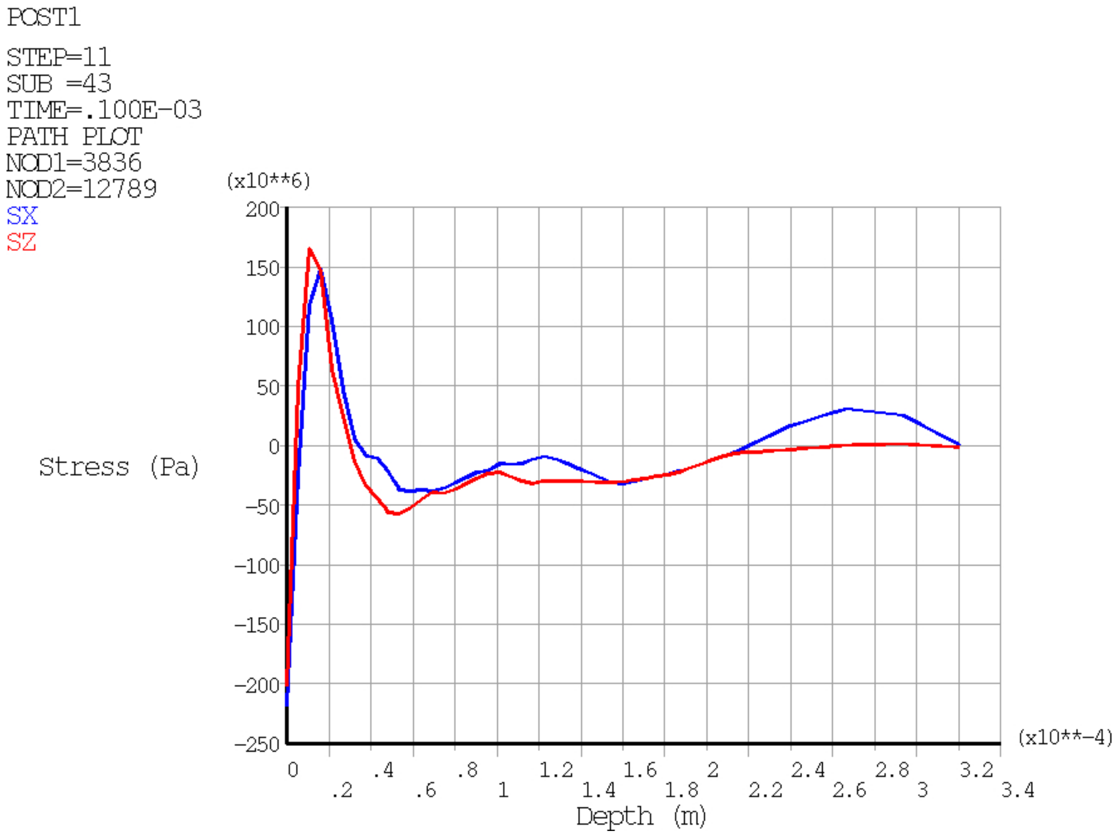

Figure 56- SX and SZ in the Centre of the Model, 41 Particle Model

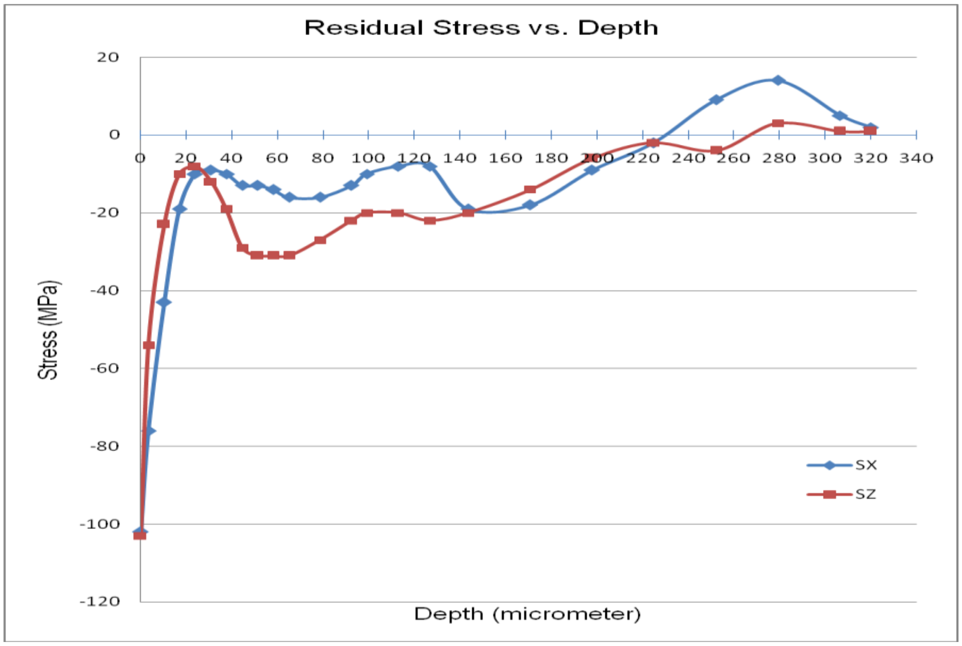

Figure 57- Average SX and SZ on 100 µm x100µm Area Through Depth, 41 Particle Model

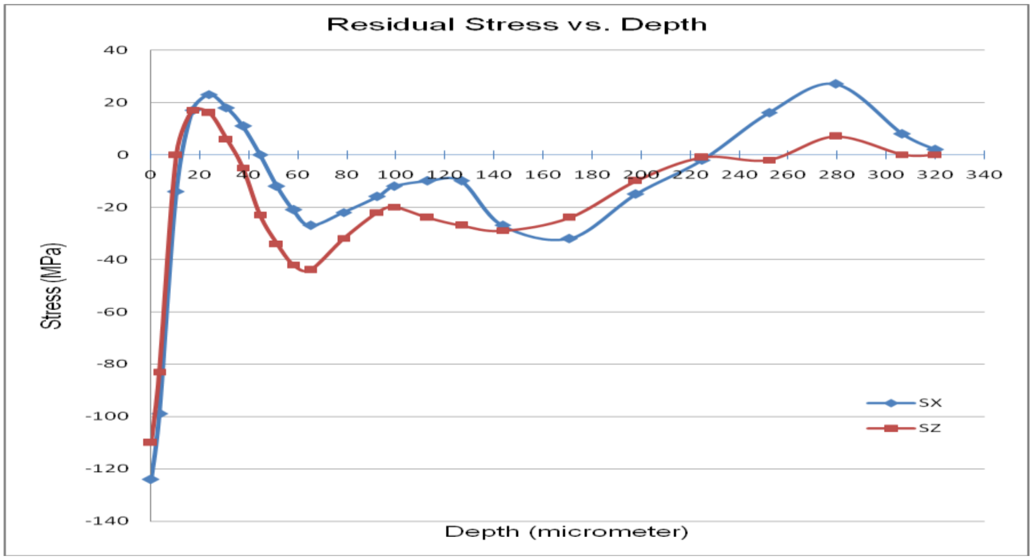

Figure 58- Average SX and SZ on 50µmx50µm Area Through Depth, 41 Particle Model

As the area for calculating the average becomes smaller, the results converge to the residual stress profile in the centre of the model. The common points that can be observed in these results are as follows:

- In spite of single particle results, multiple particle simulations present high compressive residual stress on the surface between 100 to 250 MPa for SX and SZ. Existence of compressive stress on the surface is expected but the values cannot be reliable due to the computational errors on surface elements. It is estimated that the magnitude of the compressive residual stress on the surface is lower than what simulation shows.
- Up to a depth of 20 µm a rapid decrease in compressive stress is observed in all multiple particle results and in some cases it changes to tensile stress within this depth. This is a major difference between the results of isotropic and anisotropic materials. In isotropic materials at a depth close to the surface there is a maximum compressive stress while for anisotropic materials like AZ31B, there is a considerable tensile residual stress under the surface. This can be considered as a crack initiation point for components with anisotropic material that have been introduced to surface treatments such as cold spray coating or shot peening.

- Below 20 µm, a region of compressive stress is observed with a maximum of 20 MPa to 100 MPa. This compressive stress exists down to a depth of 160 µm to 220 µm. Beyond that there is a minor oscillation of stress around zero.
- The trends of SX and SZ are similar but in all results, SZ show more compressive stress than SX.

3.1.5 Effect of Material Properties and Velocity of Particles on Residual Stress

In this section the effect of material properties and velocity of particles on the results have been studied. As mentined in section 2.1.1, particle material is Aluminum alloy, series 1100, based on data received from Centerline. Yield stress for this material is 35 MPa. To study the effect of material properties, a single particle simulation has been repeated with yield stresses of 70 MPa, 105 MPa, and 150 MPa for the particle and also with rigid particle. The same particle velocity of 400 m/s has been applied as section 3.14.1. The residual stress results have been obtained and compared to the results from the original material properties as shown in Figures 59 and 60. As the results demonstrate, increase of yield stress of particle material results in the slight increase in depth residual stress. This shows that particle material properties do not play a major role in induced residual stress.

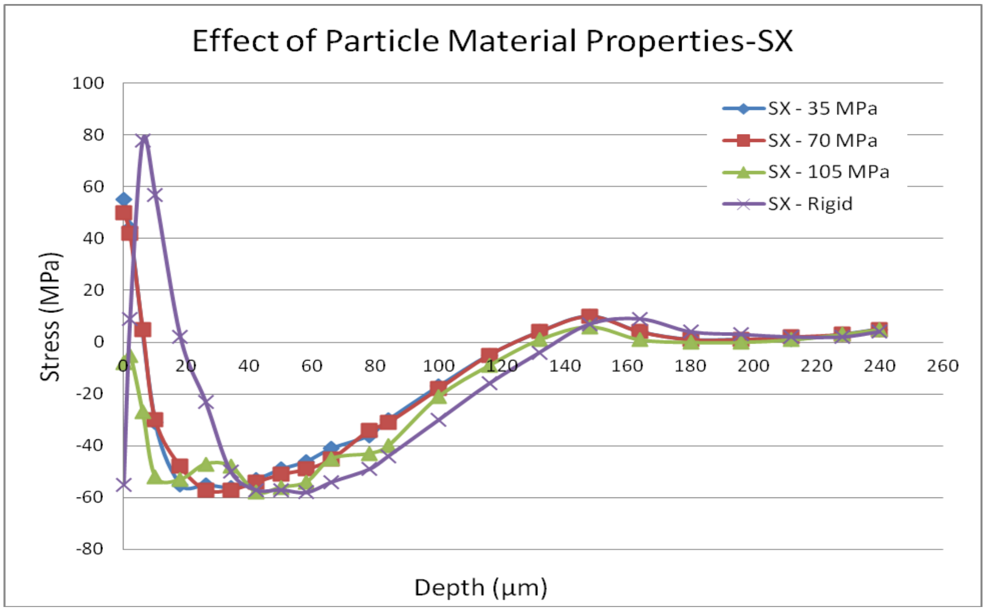

Figure 59- Effect of Particle Material Properties on Induced Residual Stress, SX

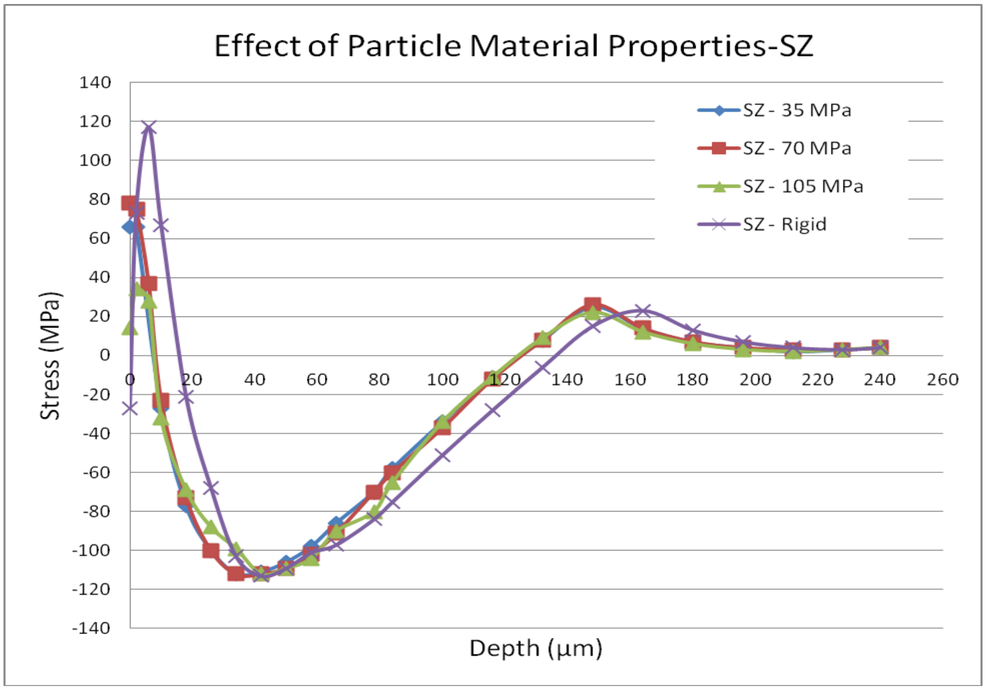

Figure 60- Effect of Particle Material Properties on Induced Residual Stress, SZ

To study the effect of particle velocity, a single particle simulation has been repeated with particle velocities of 500 m/s and 600 m/s and the results for SX and SZ have been compared with 400 m/s in figures 61 and 62.

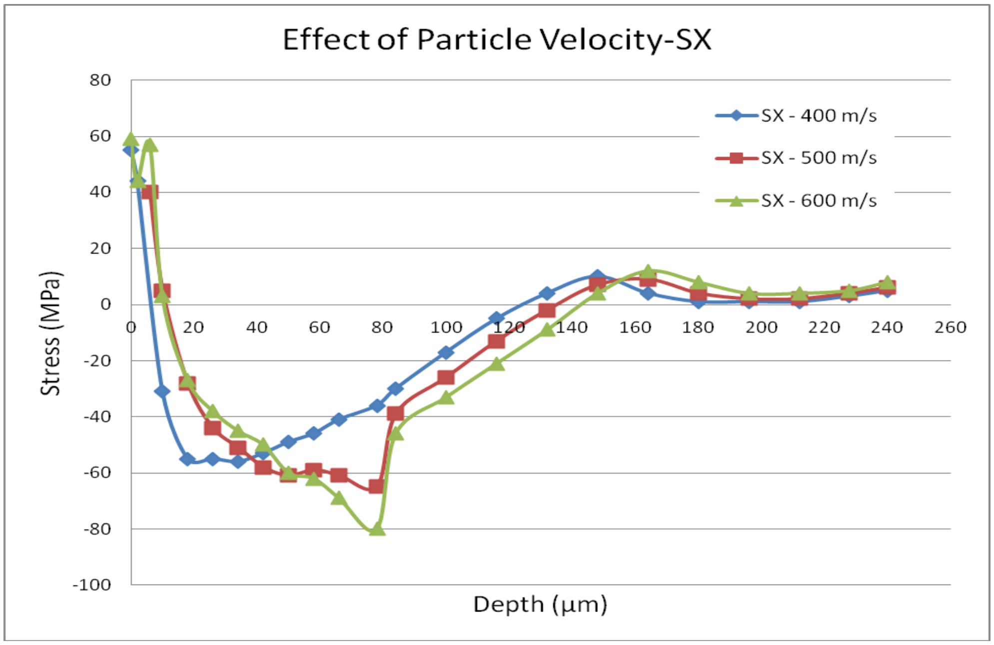

Figure 61- Effect of Particle Velocity on Induced Residual Stress, SX

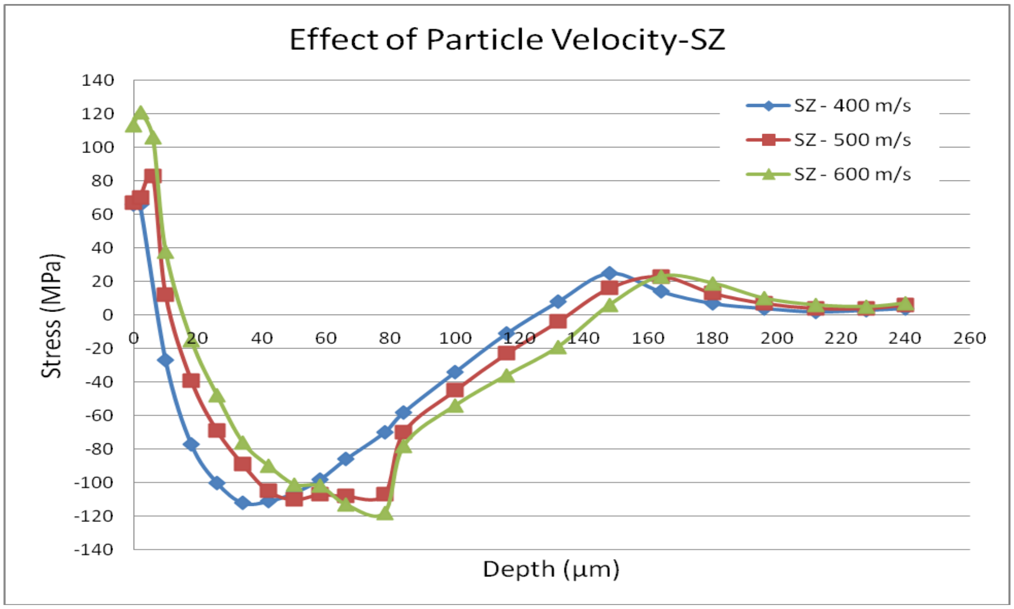

Figure 62- Effect of Particle Velocity on Induced Residual Stress, SZ

As the figures 61 and 62 show, particle velocity has more effect on the residual stress compared to its material properties. Increase of particle velocity increases intensity of residual stress, especially in the depth of 40 µm to 80 µm. In addition SZ shows more sensitivity to particle velocity compared to SX.

3.2 Stress Measurement Using X-Ray Diffraction (XRD)

Parallel to using FEA, stress evaluation has been performed using experimental methods. For this purpose X-Ray Diffraction (XRD) which is a widely used method for residual stress measurement has been employed. Figure 63 shows the sample of AZ31B that has been used for this purpose. The first step is to apply a stress relief process to relieve the initial residual stress that exists in the sample due to extrusion of the raw material. For stress relief, the ASM recommended method has been employed [45]. This standard recommends a thermal process of 500 °F (265 °C) for 15 minutes. To verify the effectiveness of stress relief process, residual stress on the surface of as received and stress relieved samples has been performed by two sources, Lambda Technologies and The Polytechnic Institute of Milan. Table 11 provides the stress measurement results that approve the stress relief process.

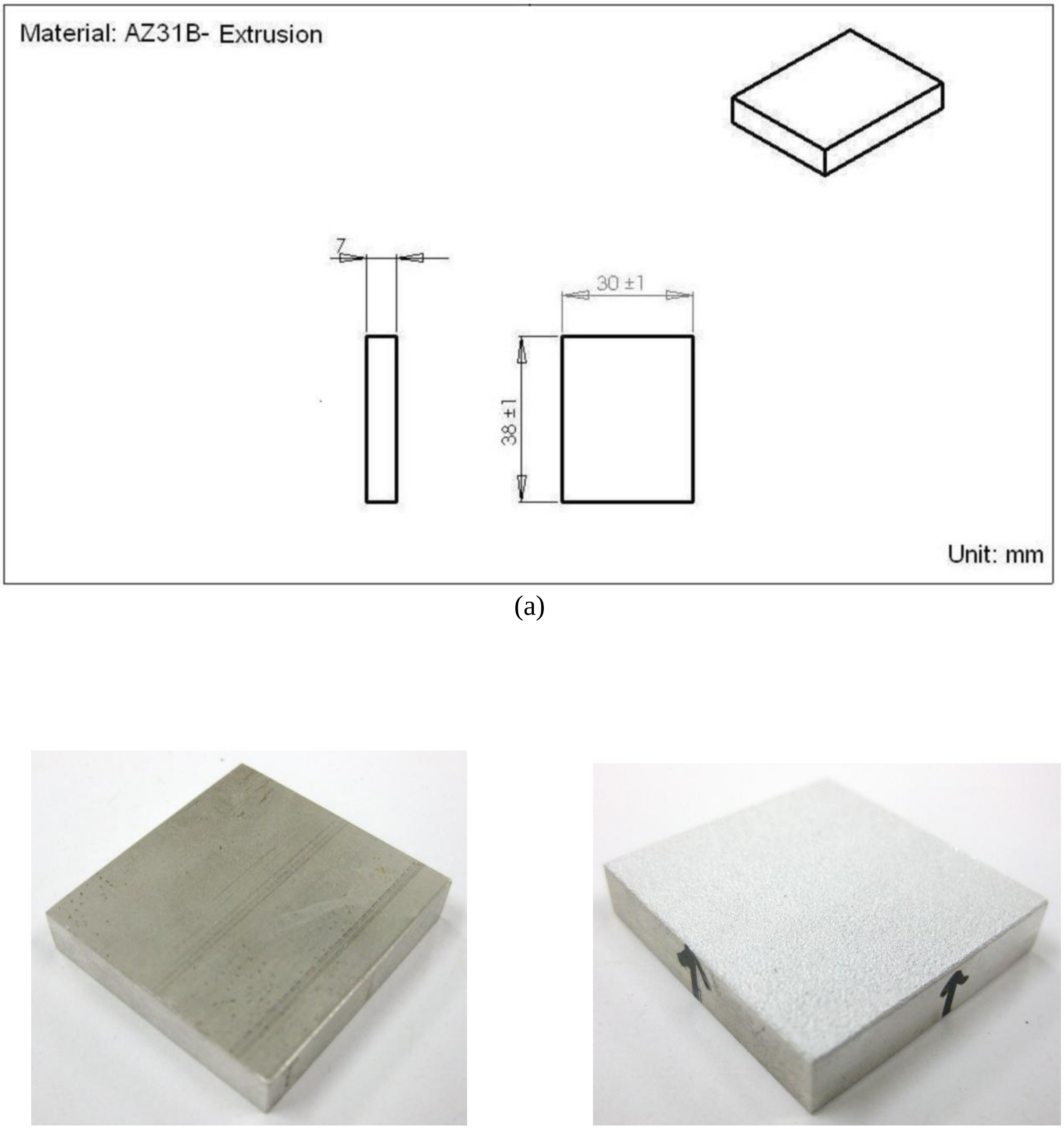

(a)

(b) (c)

Figure 63- Flat Sample of AZ31B for Stress Relief Process; a) Drawing, b) Uncoated Sample, c) Coated Sample

Sample/Process	Lambda Technologies		Polytechnic of Milan	
	Noimnal (MPa)	Tolerance (MPa)	Noimnal (MPa)	Tolerance (MPa)
As received sample	-43	+/- 1	-36.6	+/- 21.1
stress relieved sample	2	+/- 1	137*	+/- 109

* The value is considered zero due to the wide tolerance. (Comment from the Polytechnic Institute of Milan)

Table 11- XRD Stress Measurement Results on As Received and Stress Relieved Samples

After stress relief, cold spray coating has been applied on the flat sample using the following characteristics:

Particle velocity = 400 m/s

Particle diameter= 40 µm

Particle material: Aluminum alloy, series 1100

Grit blasting before cold spray coating

Coating layer thickness= 0.1 mm

These are the same parameters that have been used for FEA.

The coated sample then has had a stress measurement in depth by Lambda Technologies. X-Ray Diffraction residual stress measurements were performed using a two-angle sine-squared-psi technique, in accordance with SAE HS-784, employing the diffraction of manganese K-alpha radiation from the (203) planes of the HCP structure of the AZ31. Table 12 and Figure 64 provide the results of this measurement. Figure 64a presents the profile of the residual stress through depth and Figure 64b, Peak Width Distribution, shows that the material in the last depth is softer or less cold worked than the other depths.

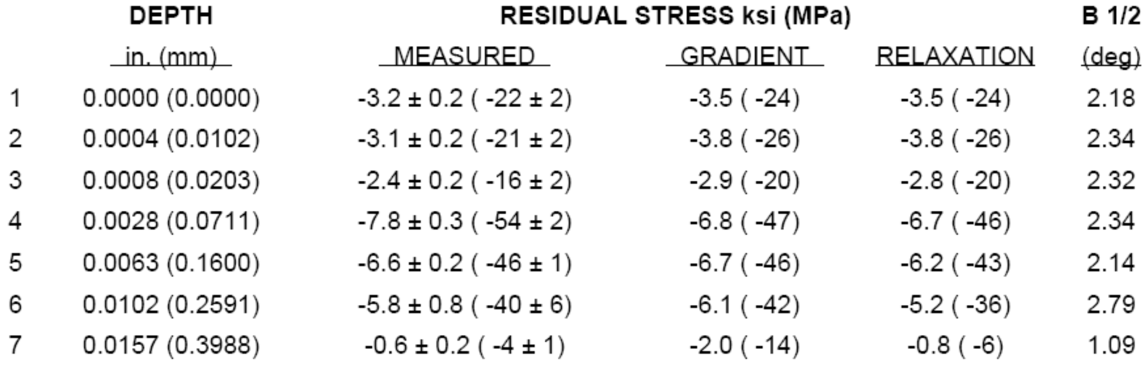

	DEPTH	RESIDUAL STRESS ksi (MPa)			B 1/2
	in. (mm)	MEASURED	GRADIENT	RELAXATION	(deg)
1	0.0000 (0.0000)	-3.2 ± 0.2 (-22 ± 2)	-3.5 (-24)	-3.5 (-24)	2.18
2	0.0004 (0.0102)	-3.1 ± 0.2 (-21 ± 2)	-3.8 (-26)	-3.8 (-26)	2.34
3	0.0008 (0.0203)	-2.4 ± 0.2 (-16 ± 2)	-2.9 (-20)	-2.8 (-20)	2.32
4	0.0028 (0.0711)	-7.8 ± 0.3 (-54 ± 2)	-6.8 (-47)	-6.7 (-46)	2.34
5	0.0063 (0.1600)	-6.6 ± 0.2 (-46 ± 1)	-6.7 (-46)	-6.2 (-43)	2.14
6	0.0102 (0.2591)	-5.8 ± 0.8 (-40 ± 6)	-6.1 (-42)	-5.2 (-36)	2.79
7	0.0157 (0.3988)	-0.6 ± 0.2 (-4 ± 1)	-2.0 (-14)	-0.8 (-6)	1.09

Table 12- XRD Results for In Depth Measurement of Stress Relieved/Coated Samples

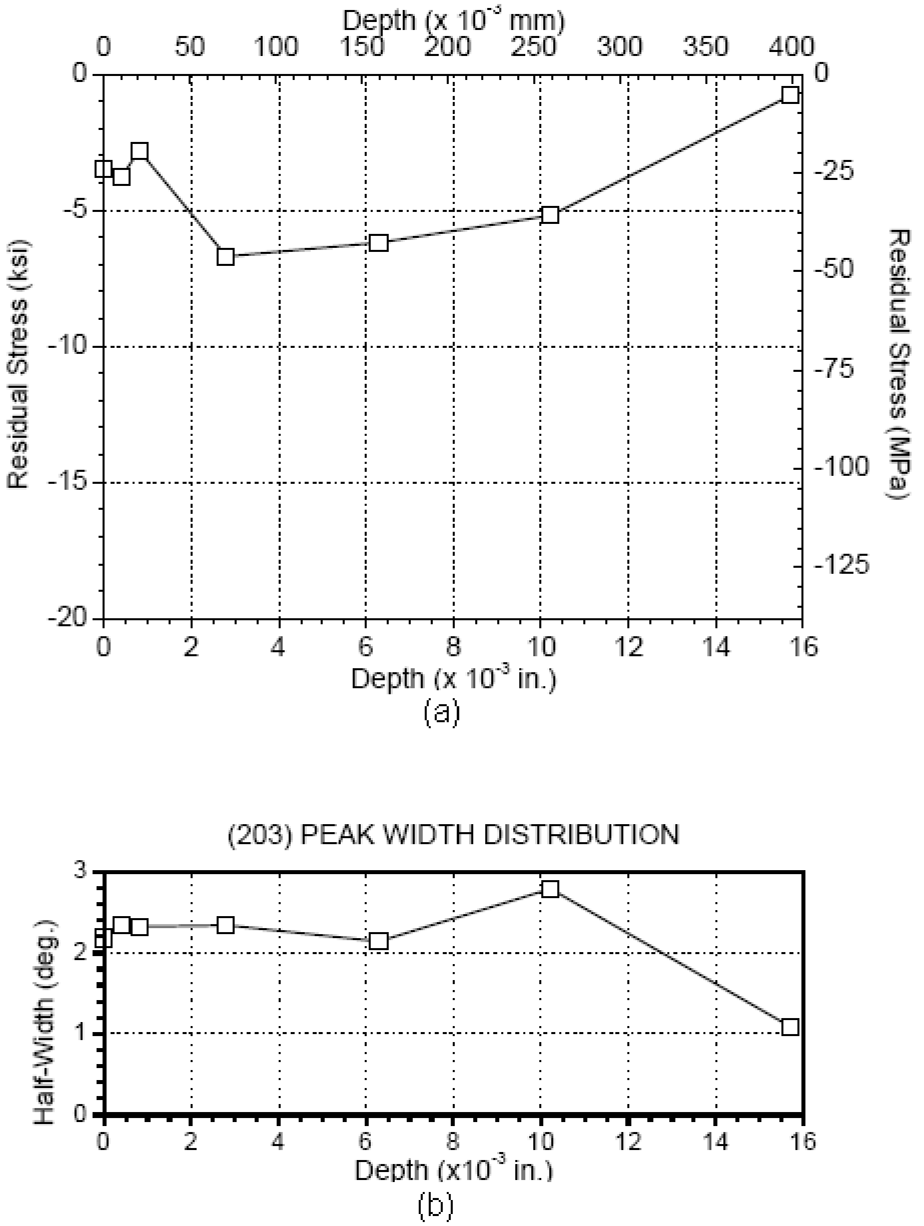

Figure 64- XRD Results for In Depth Measurement of Stress Relieved/Coated Samples, a) Profile of Residual Stress through depth, b) Peak Width Distribution

Since the stress measurement by XRD has been done only in the direction of extrusion (ED or X direction), It should be compared to SX calculated by FEA. Among the FEA results, SX obtained from 41 particle simulation is closer to XRD in comparison to single and 13 particle simulations. Figure 65 compares XRD result to SX obtained from 41 particle simulation.

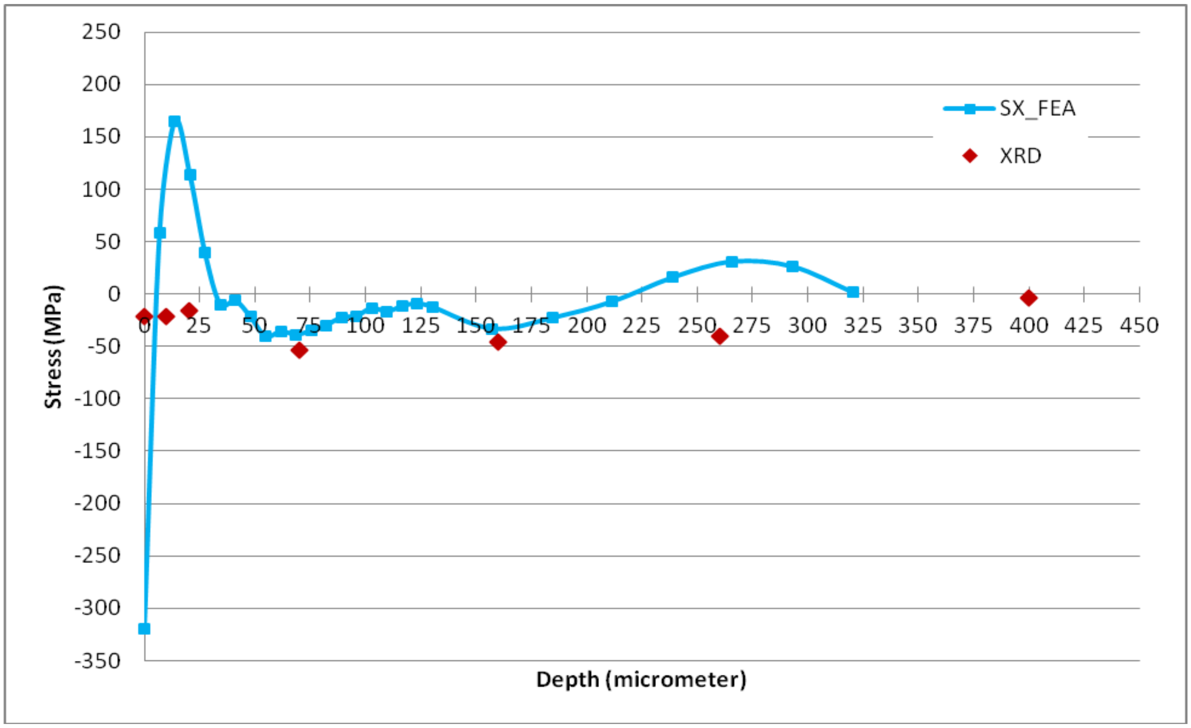

Figure 65- Comparison of XRD Result with SX from 41 Particle Simulation

The following points can be concluded from comparison of XRD results and FEA results:

- There is a big difference in results between the two methods for residual stress on the surface of the substrate. This was expected because of the errors that exist for the outer layers of elements in FEA.
- There is a similarity between the two methods at the depth of 20 µm where a decrease in compressive stress is observed.
- Maximum compressive stress obtained from XRD matches results from single particle simulation and is in the same order of magnitude for 13 and very close to 41 particle simulations.
- The depth of maximum compressive stress is close for XRD and single, 13, and 41 particle simulations.
- Beyond the depth where maximum compressive stress occurs, there is a considerable difference between XRD results and FEA results. This is due to all the assumptions made in the FEA that makes the results far from the reality. These assumptions include material properties, shape of particles, velocity of particles, number of particles that hit the substrate, and the rebounded particles from the surface of the substrate.

Chapter 4 Effect of Cold Spray Coating on Fatigue Strength

In this section the effect of cold spray coating on fatigue strength of AZ31B is studied. For this purpose cylindrical hourglass specimens have been used. Three groups of specimens including as received, stress relieved and stress relieved/coated specimens have been tested by a Rotating Bending Machine (RBM) to prepare S-N curves for each group. Comparing S-N curves provides an estimation of the effect of cold spray coating on fatigue strength of AZ31B.

4.1 Test Specimens

Specimens used for the test are shown in figure 66. Overall length of the specimens is 70 mm and the diameter of the neck is 7 mm. These specimens have been designed in accordance with the requirement of the Rotating Bending Machine. To make sure the hourglass shape is smooth enough and does not cause any stress concentration affecting the test results, an FEA simulation has been done using Abaqus6.7 CAE. In this analysis, stress induced in the specimen due to the weight of RBM machine bearings has been calculated. The model and the result of the analysis have been provided in figure 67. Bearing housing with the weight of 2.5 kg each can rotate about axes 1 and 2 shown in Figure 67a. This applies a constant bending moment on the cylindrical specimen which has been shown in green, resulting maximum compressive stress on the top and maximum tensile stress on the bottom of the cylindrical specimen with the magnitude of 27.8 MPa as shown in Figure 67b. The results show no high stress zone and stress concentration area. The magnitude of bending stress was used in the evaluation of the initial induces stress due to RBM components weight.

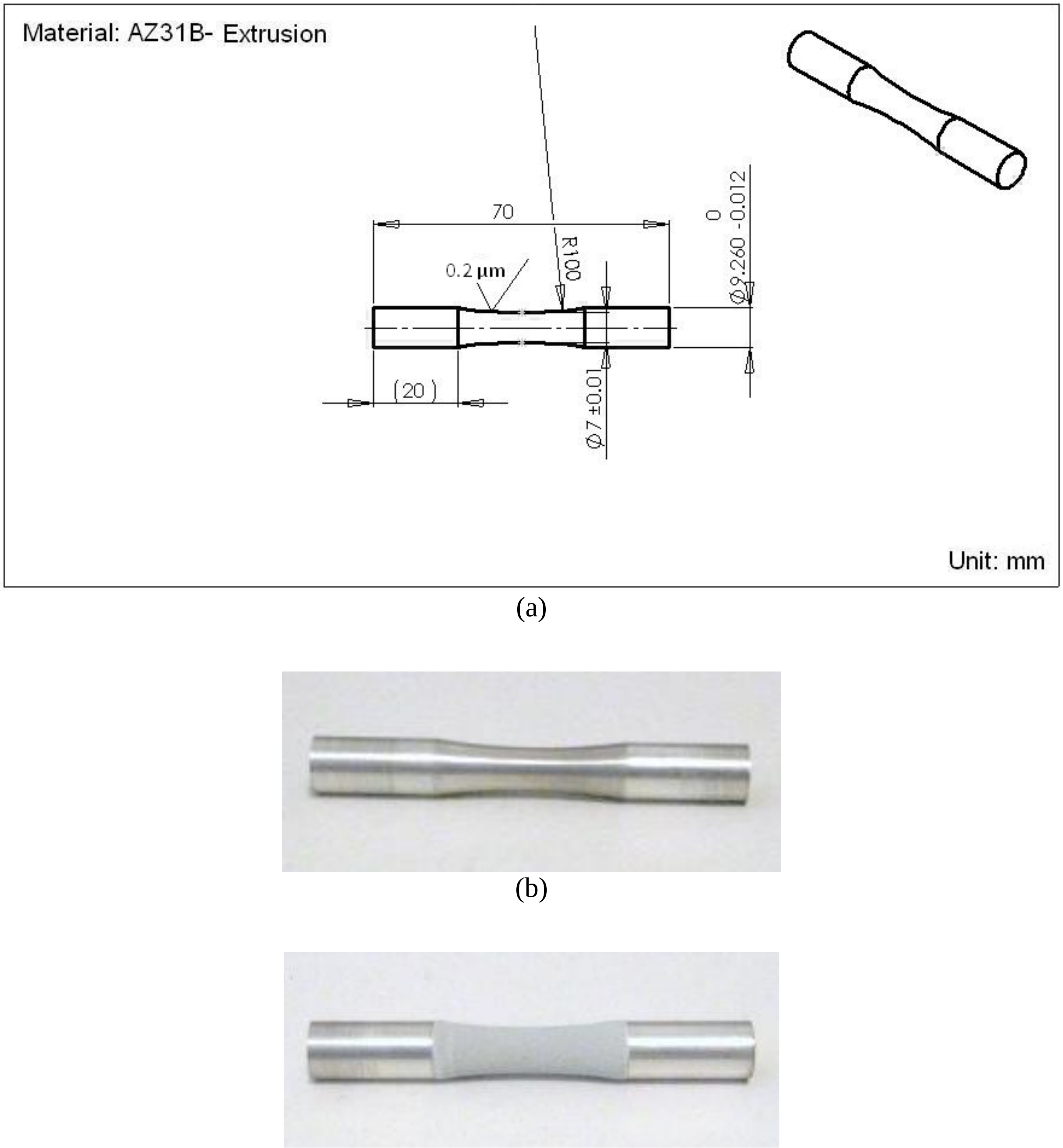

(a)

(b)

(c)

Figure 66- Round Specimens Used for Extracting S-N Curve of AZ31B; a) Drawing, b) Uncoated, c) Coated

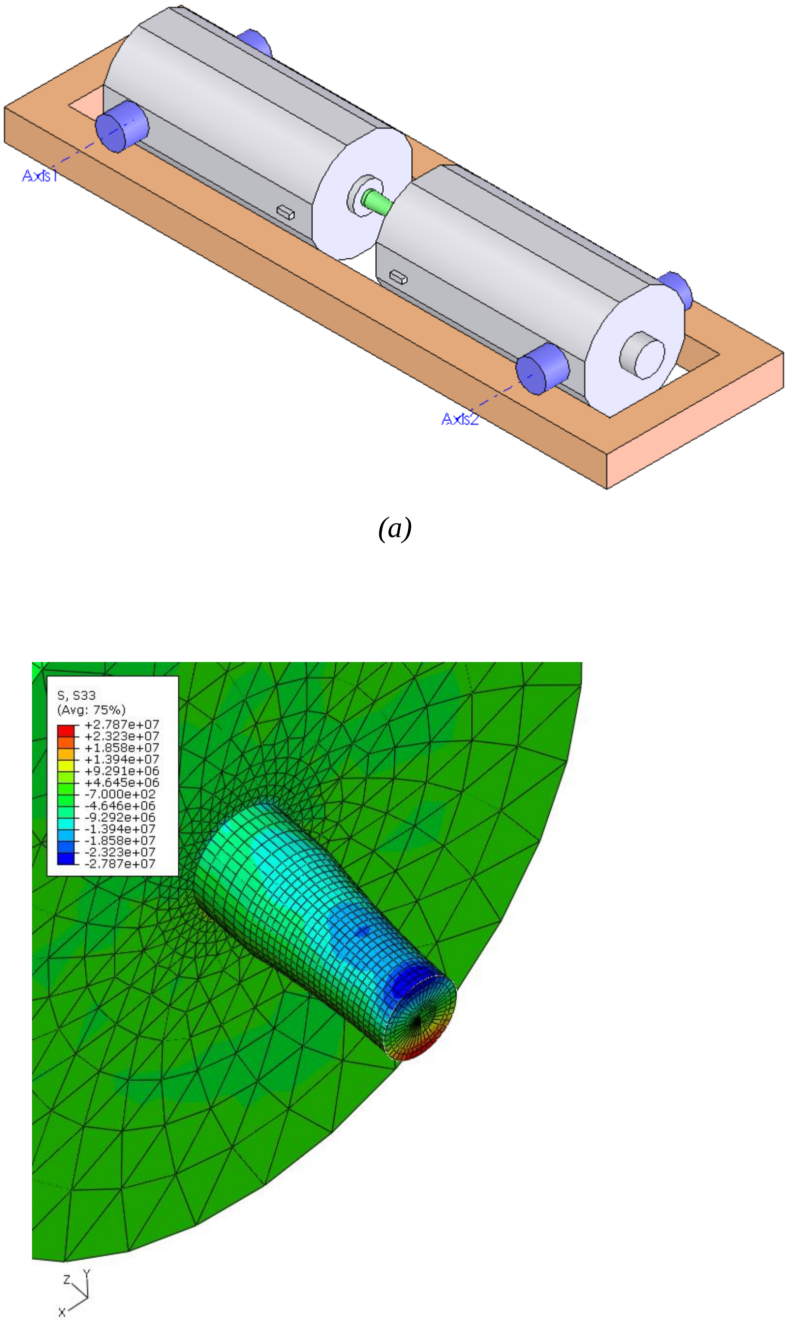

(a)

(b)

Figure 67- Investigation of the Stress Concentration on Hourglass Area of Cylindrical Specimen, a) Model of RBM Housings and Cylindrical Specimen, b) FEA Result on the Hourglass Area of the Cylindrical Specimen

4.2 Rotating Bending Machine

An R.R.Moore machine has been used for the fatigue tests. This equipment is widely used for rotating bending fatigue tests. Figure 68 shows this equipment. A round hourglass specimen is gripped by two collets between two bearing housings. An adjustable load is applied to the end of the bearing housings that causes constant bending moment in a vertical plane to the specimen. The bending moment applies maximum compressive stress at the top point of the specimen and maximum tensile stress at the lower point of the specimen. The stress can be varied by changing the weight loads. An electrical motor with adjustable speed between 500 RPM to 10,000 RPM rotates the specimen. As a result of each rotation, the specimen experiences an oscillating stress varying from maximum compressive to maximum tensile with the average of zero. Number of rotations that shows the number of load cycles is recorded by a counter. Applying different loads on the specimen and recording the number of cycles to failure provides the data necessary for the S-N curve. Maximum loads with number of cycles more than 10 million is considered as run out or the endurance limit.

▲
R. R. Moore rotating beam fatigue testing system

Figure 68- Rotating Bending Machine Used for Fatigue tests [52]

4.3 Fatigue Tests

Three groups of cylindrical specimens have been used for fatigue tests: As Received, Stress Relieved, and Stress Relieved/Coated. All tests performed at standard lab condition. Tests were performed at frequencies between 50 Hz for low cycle to 100 Hz for high cycle tests.

4.3.1 As Received Specimens

There is an initial compressive residual stress in As Received specimens due to the extrusion process of AZ31B. Using XRD measurement on a cylindrical specimen in the hourglass zone shows the amount of this compressive stress to be 34 MPa. As Received specimens have been used for fatigue tests to correlate the initial residual stress to fatigue life and to be able to compare results to other groups.

4.3.2 Stress Relieved Specimens

A stress relief process has been applied on the second group of AZ31B specimens. As mentioned in section 2-2, the ASM recommended stress relief process, 500 °F (260 °C) for 15 minutes, has been used for these specimens. The purpose is to evaluate the fatigue strength in absence of any residual stress. XRD measurement on stress relieved cylindrical specimens on hourglass area shows +11 tensile stress on the surface.

4.3.3 Stress Relieved/Coated Specimens

The purpose of selecting this group for fatigue tests is to evaluate the residual stress that is induced due to cold spray coating and its effect on fatigue life of AZ31B. Stress relieved specimens in accordance to section 3.3.2 have been coated using the same parameters of section 2.2. The coating has been applied on the hourglass area only with the thickness of 0.1 mm.

4.3.4 Test Results

Table 13 provides data obtained from fatigue tests and Figure 69 shows the S-N curve for three groups of specimens.

As Received		Stress Relieved		Stress Relieved/Coated	
S (Mpa)	N (Cycles)	S (Mpa)	N (Cycles)	S (Mpa)	N (Cycles)
188	5800	188	9400	188	7300
188	5400	165	26000	165	35000
188	5200	150	48500	165	31200
165	19000	135	63400	150	54500
150	82500	120	139000	135	75000
135	195000	113	192800	128	142800
128	511000	105	314000	120	207000
120	1116400	101	356000	113	203000
118	4519000	100	237000	110	245000
116	>10000000	100	697000	109	312000
		99	>10000000	108	>10000000

Table 13- RBM Test Results

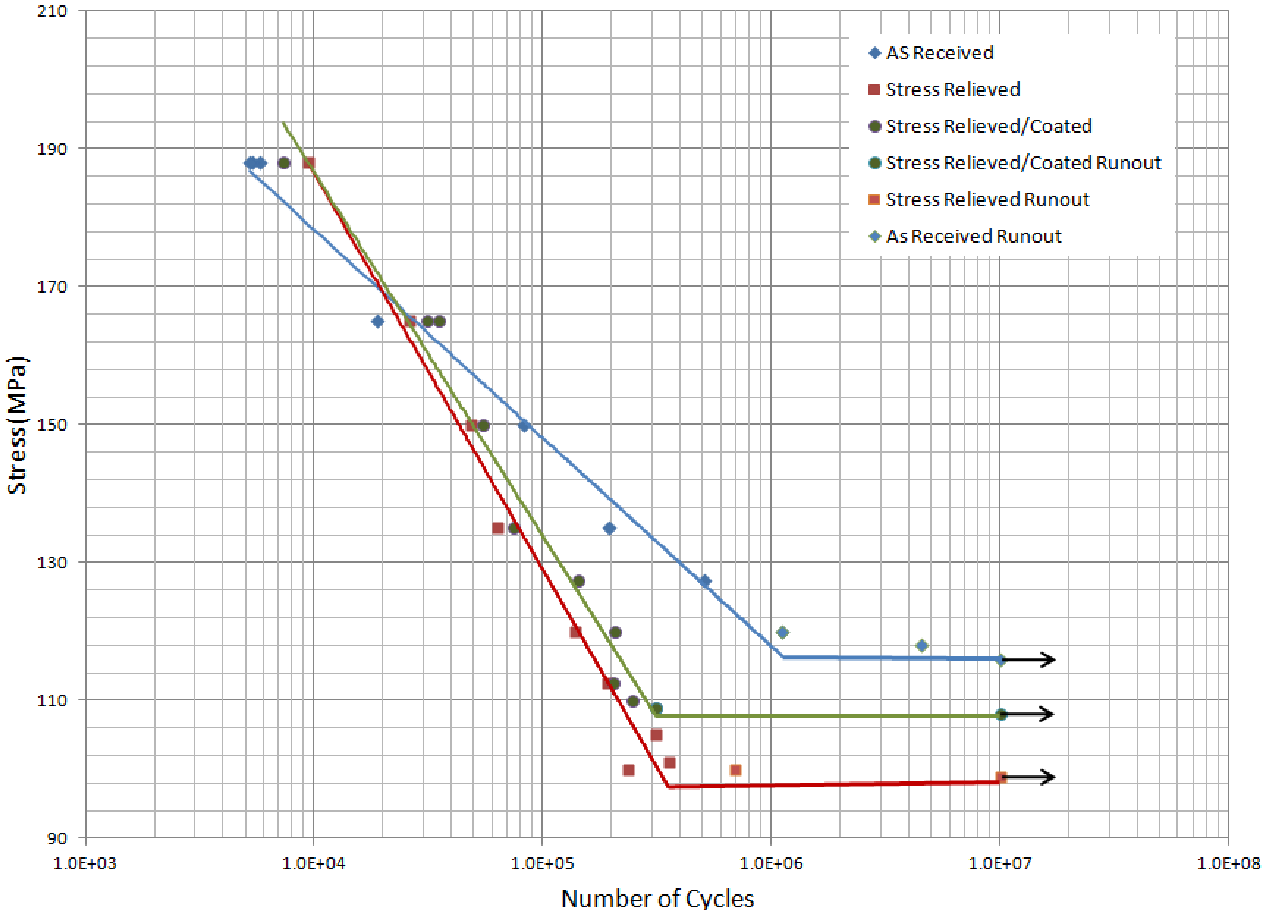

Figure 69- S-N Curves of As Received, Stress Relieved, and Stress Relieved/Coated Specimens of AZ31B

4.3.5 Fracture Surfaces

It is beneficial to study the crack initiation and growth of the tested specimens and to compare them. Figure 70 shows the fracture surfaces of round specimens under different types of loading [50]. The light areas represent the crack growth regions and the dashed areas represent final fracture regions. In our case the specimens are smooth, the loading type is rotating bending, and selected specimens are from high nominal stress tests.

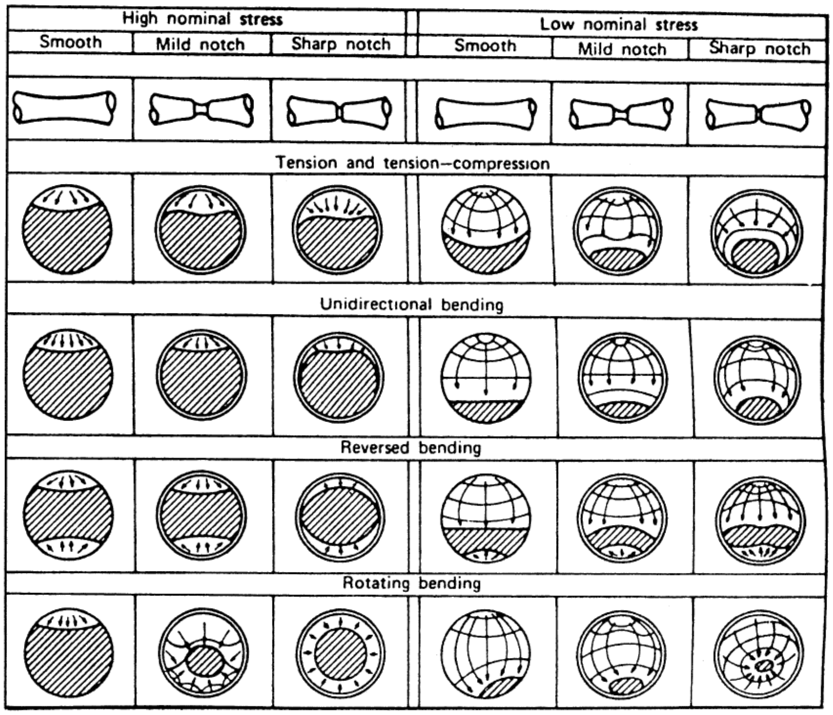

Figure 70- Fatigue Surfaces of round Specimens under Different Types of Loading [50]

To compare the fracture surface of as received, stress relieved and stress relieved/coated specimens, some SEM images have been prepared. Figure 71 and 72 show the prepared images for as received and stress relieved samples.

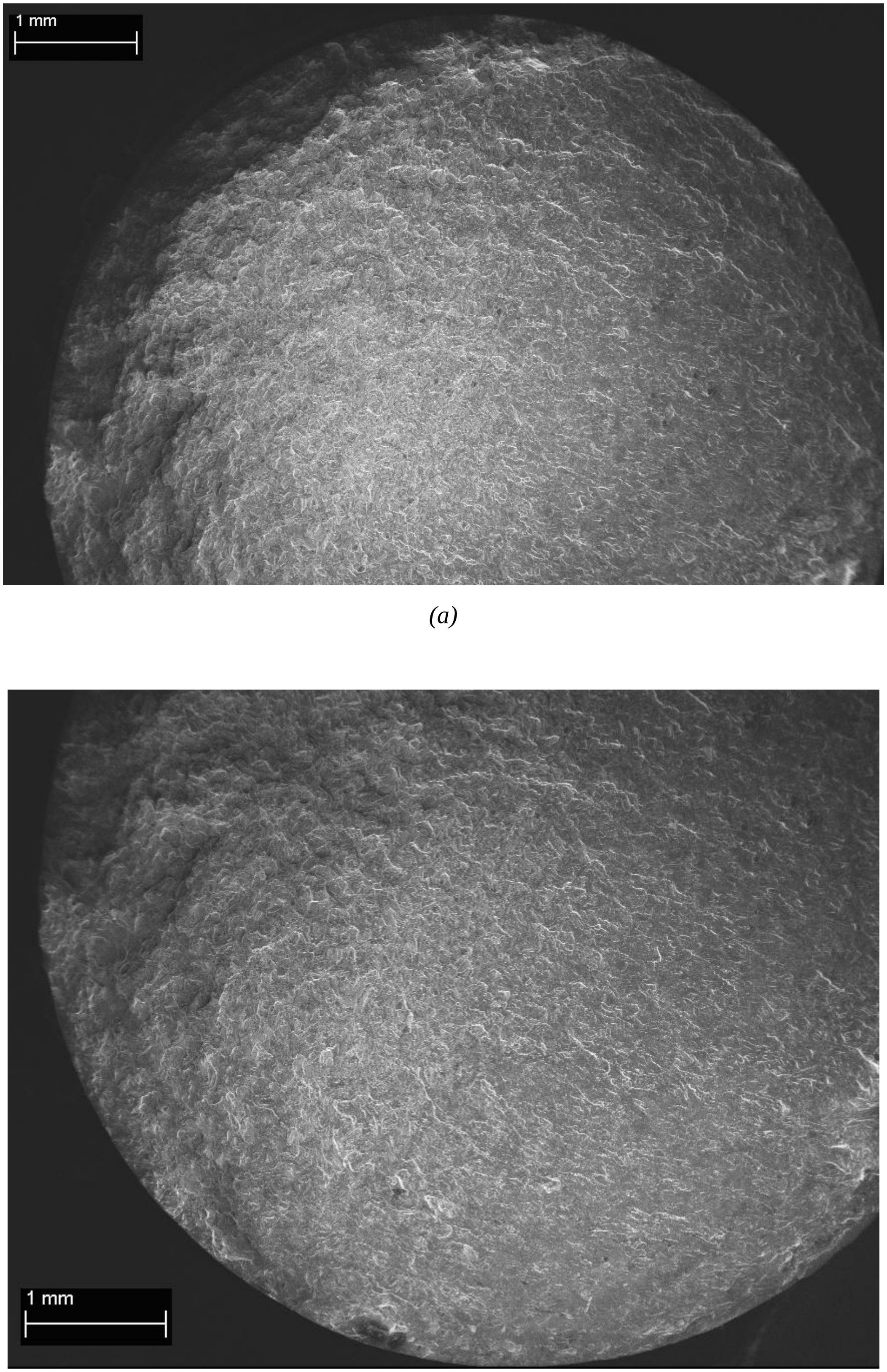

(a)

(b)

Figure 71 a), b)- Fracture Surface of As Received Specimen with the Nominal Stress of 165 MPa

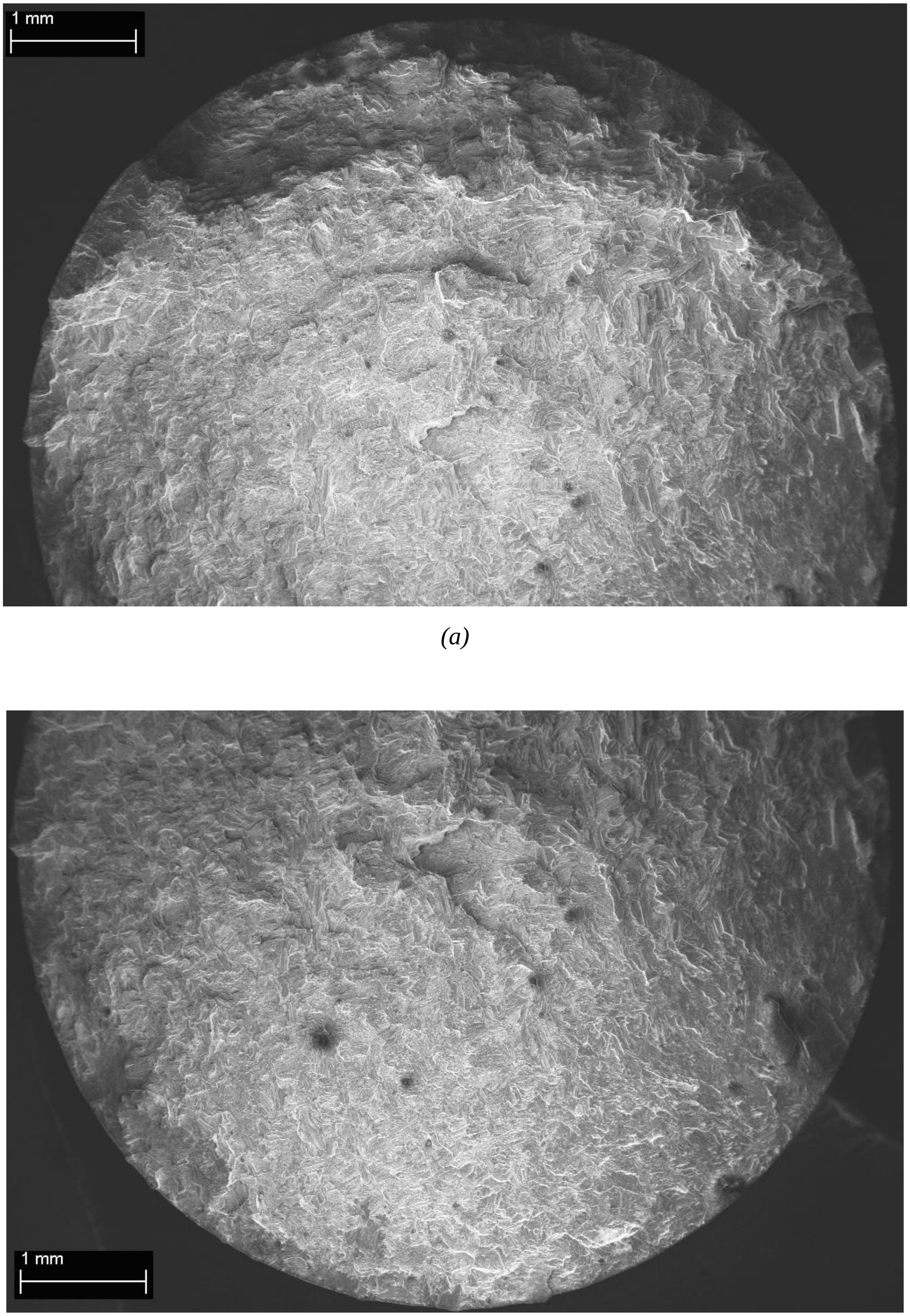

(a)

(b)

Figure 72 a), b)- Fracture Surface of Stress Relieved Specimen with the Nominal Stress of 188 MPa

As Figure 71 shows, the crack growth region for as received specimen is a narrow area extended from top to bottom on the left side of the image. Beyond this relatively rough region, a smooth area is observed which represents the final fracture region. For stress relieved specimen, Figure 72, the crack growth region is a rough area on the top of the image and beyond this region is the smooth area of final fracture. The fracture surfaces of both specimens are similar to the surface shown in Figure 70 for smooth round specimens under high nominal stress. Since the stress relieved specimen is free from surface compressive residual stresses, its crack growth region is wider and rougher than as received specimen. The other point is that the direction of crack growth of as received specimen is parallel to thickness direction while it is perpendicular to thickness direction for stress relieved specimen. It should be reminded that for both cases, the stress has been applied in extrusion direction since the axis of the specimens has been parallel to extrusion direction.

Figure 73 shows the fracture surface of stress relieved/coated specimen that has been tested under nominal stress of 188 MPa. As Figure 73a presents, the crack initiation region is extended from the middle right to middle bottom of the image. Coating layer delamination is visible in the center of this region. Figure 73b shows a closer image of this area. The center of crack nucleation area makes the angle of 45° to the thickness direction. Except for the crack initiation point, no coating layer delamination is observed around the fracture surface of the specimen that proves strong bonding between coating particles and the specimen surface. Figure 73c shows the coating layer and the fracture surface.

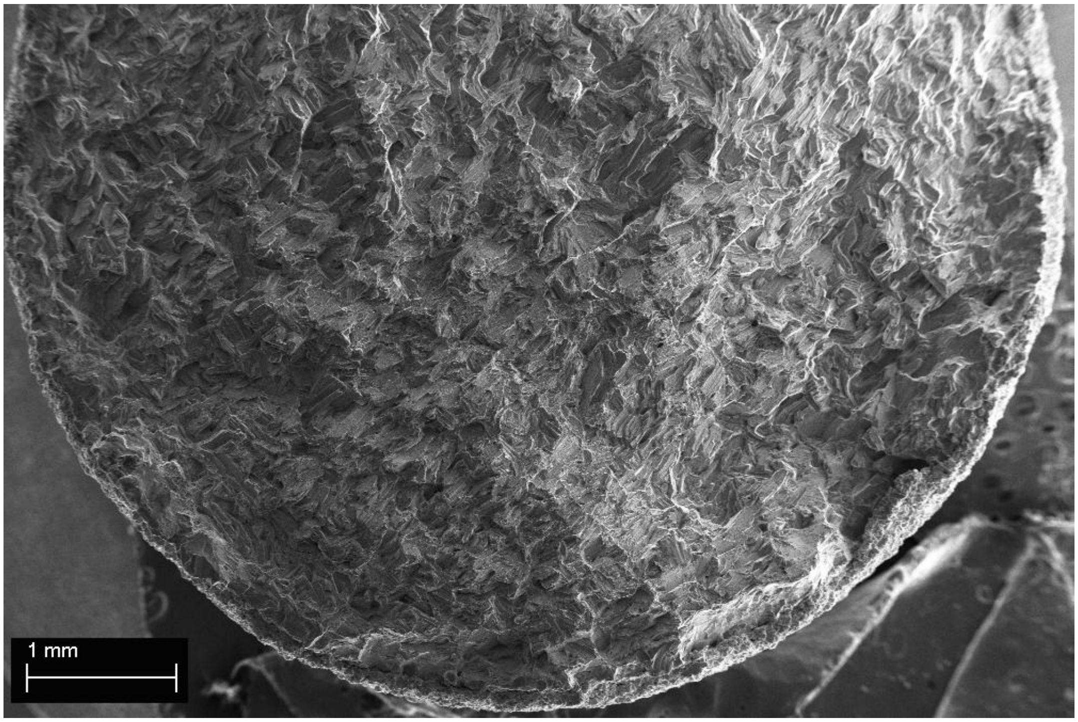

(a)

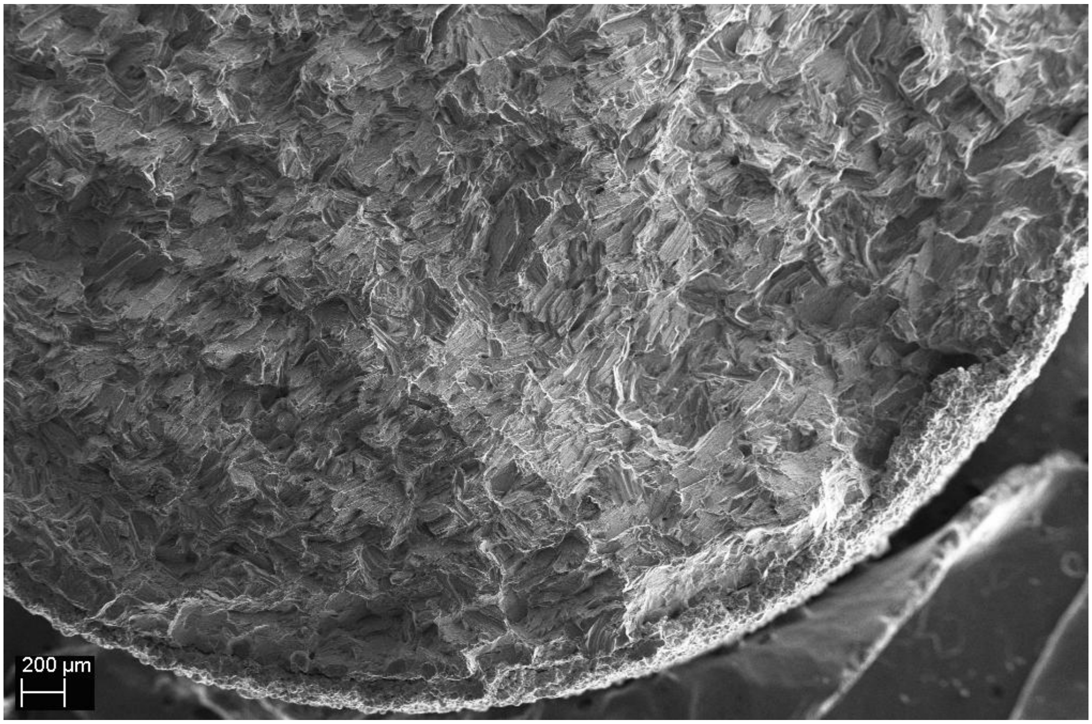

(b)

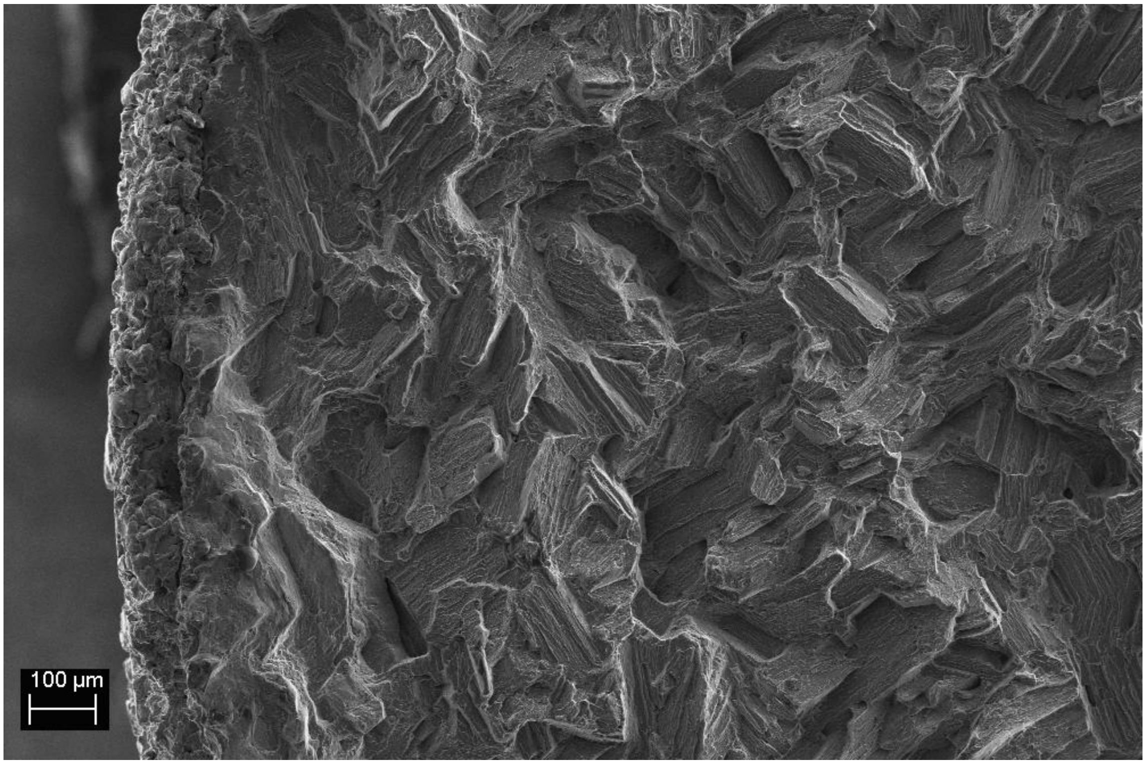

(c)

Figure 73- Fracture Surface of Stress Relieved/Coated Specimen with the Nominal Stress of 188 MPa, a), b) Crack Initiation Region, c) Coating Layer

4.3.6 Test Conclusions

- As expected, there is a correlation between surface residual stress and fatigue strengths. Table 14 shows the values of surface residual stress, measured by XRD, and endurance limit for the three groups of specimens.

Group	Residual Stress on Surface (MPa)	Endurance Limit (MPa)	Remarks
As Received	-43	116	Measured on hourglass area
Stress Relieved	+11	99	Measured on hourglass area
Stress Relieved/Coated	-22	108	Measured on coated flat sample

Table 14- XRD Results on Cylindrical Specimens

- In low cycle fatigue, there is a considerable drop in fatigue life after stress relief. This is due to considerable loss of compressive residual stress. Cold spray coating process improves the fatigue strength slightly. This means that residual stress induced by cold spray coating is much lower than the residual stress induced by the initial extrusion process forming the as received specimens.

- The As received specimens show better fatigue strength among the three groups. The S-N curve for this group has a smooth transition to the endurance limit while the S-N curves of the stress relieved and stress relieved/coated specimens have sharp transitions to the endurance limit.
- Table 15 compares the life cycles of stress relieved and stress relieved/coated under equal loads and provides the percentage of life improvement after coating the stress relieved specimens.

	Stress Relieved	Stress Relieved/Coated	
S (Mpa)	N (Cycles)	N (Cycles)	Life Change (%)
188	9400	7300	-22.3
165	26000	35000	34.6
150	48500	54500	12.4
135	63400	75000	18.3
120	139000	207000	48.9
113	192800	203000	5.3

Table 15- Life Improvement after Coating the Stress Relieved Sspecimens

As Table 15 shows, except for the load of 118 MPa that a drop in life cycles is observed, for all other loads the fatigue life of the stress relieved specimens has improved after coating with the maximum of 48.9% for the load of 120 Mpa.

- Stress relief process lowers the endurance limit of as received specimens from 116 MPa to 99 MPa, equal to 14.6%. Coating process improves the fatigue strength of stress relieved specimens and increases their endurance limit from 99 MPa to 108 MPa, equal to 9%.

Chapter 5 Conclusion

Wrought magnesium alloys are the lightest alloys used as structural members in automotive and aerospace industries. There is an outlook of more demand for these alloys in the future due to their high specific strength. Since these alloys show low resistance against corrosion when used in aggressive environments, some protection processes are applied for corrosion protection. Cold spray coating, a modern protection process, is one of these methods. Considering the bombardment of the surface of component by micro particles of supersonic velocity, the question arises whether this process improves fatigue strength of the component in addition to providing corrosion protection. This was the main purpose of this work. In this research the effect of cold spray coating on fatigue life of magnesium alloy AZ31B was investigated. The result of this work is discussed in the following two sections.

5.1 Residual Stress Evaluation

Residual stress induced by cold spray coating was investigated by two methods; finite element analysis and XRD stress measurement. For the finite element analysis, ANSYS classic code, an implicit analysis package with an anisotropic material model was used. Material properties of AZ31B were used from Albinmousa et al. [3] and results of their experiments. Missing data was obtained from the complimentary tests, the ANSYS consistency equation, and assumptions. This material data was from monotonic tests. In the absence of high rate material properties in the literature, the applied data was the best available data that could be used. Simulation was performed for single and multiple particle models. During the simulation there were some convergence issues that made it necessary to decrease the minimum time step to 0.01e-9 s during the impact phase. Because of this, simulation time increased considerably. As an example, the run time of single particle model was 5 hours for impact phase and 20 hours for stress wave dissipation, working with a computer with 2.4 GHz processor. In spite of all the challenges, the simulations completed. In general, the results from FEA and XRD are not in expected agreement. However, there are some agreements that can be considered. Comparing results from the 41 particle simulation, SX from Figure 56, and the XRD result from Figure 64, shows that both methods are in agreement in the magnitude and depth of maximum compressive stress which are important characteristics of induced residual stress. Also both methods show a decrease of compressive residual stress at a depth of 20 µm. This is more visible in the FEA results and can be considered as a characteristic of residual stress for anisotropic materials. To answer why other data obtained from FEA and XRD are not in agreement, the following reasons can be offered. Using monotonic material properties in the simulation instead of high strain rate material data can be a reason that affects FEA results. Also there are some factors that may have caused errors in the XRD results. In depth stress measurement is a process that includes some errors due to layer removal and redistribution of residual stress. In spite of the efforts of the XRD service provider to correct this error, the error modification can be incomplete since the original stress distribution is not known. Also the limitation of repeating the XRD analysis is another issue. Since in house facilities for stress measurement were not available, this part of the work was outsourced and considering the high cost of XRD stress measurement, the test was done only once. If the stress measurement could be repeated, it might help to obtain more accurate results. In general stress measurement was a critical part of this research and absence of in house facilities for stress measurement caused delays and inaccuracies in the results. Based on the experience obtained in this research, it is recommended that for similar work, the availability of stress measurement equipment in the university is crucial. University owned equipment can save time and cost and can also provide reliability and accuracy based on repeated testing.

The second part of the residual stress evaluation was devoted to the study of particle parameters on the results. First, the yield stress of particles changed for single particle simulation. The results showed that this parameter changes the induced residual stress just slightly. This is reasonable since having more rigid particles just decreases the energy that is absorbed by particle deformation. This energy is a small portion of the kinetic energy of the particle that causes plastic deformation of the substrate and the resulting residual stress. In the second part, the velocity of the particle increased. The results show that this parameter has a bigger effect on the induced residual stress since it directly increases the kinetic energy of the particle.

5.2 Effect of Cold Spray Coating on Fatigue Strength

This part of the project directly addresses the main question of this research. The results obtained from fatigue tests were the S-N curves for as received, stress relieved, and stress relieved/coated specimens and served as criteria for fatigue strength. Comparison of the S-N curves provides a clear answer to the question. After the stress relief thermal process, existing compressive residual stresses are removed. This is why a considerable decrease in life cycle and endurance limit is observed on the stress relieved S-N curve in comparison to the as received specimen. As received AZ31B specimens experience 15% decrease in endurance limit after stress relief, changing from 116 MPa to 99 Mpa. After applying cold spray coating on stress relieved specimens, some improvements are observed. Cold spray coating enhances the endurance limit of stress relieved specimens as much as 9%, changing it from 99 MPa to 108 MPa. The maximum fatigue strength improvement is 49 percent in the load of 120 MPa. The S-N curve of as received specimens show a smooth transition to the endurance limit while stress relieved and stress relieved/coated S-N curves present sharp transition to the endurance limit.

In summary, the tests discussed in chapter 4 show that cold spray coating, with the specifications mentioned, on AZ31B extrusion can create compressive residual stress on stress relieved specimens and improve their endurance limit by 9%.

Chapter 6 Future Work

The following items are considered worthy for future work:

6.1 FEA Simulation Studies

- Using explicit FEA codes with the best available material model that can be used for magnesium alloys to simulate cold spray coating process. Comparing the results to the results provided in this work from FEA and XRD to check the accuracy of the material model
- Extending the study of the effect of cold spray parameters on the induced residual stress by FEA. One objective can be finding the ways of increasing the residual stress. The following parameters can be investigated in this study:
    - Higher velocities up to 1000 m/s, for single and multiple particle models. In this research the velocity of 400 m/s was used for single and multiple particles and the velocities of 500 m/s and 600 m/s were applied on single particle model only.
    - Increasing of the number of particles and particle layers. In this study 13 particle model with 3 layers and 41 particle model with 5 layers investigated. Because of using implicit FEA code, increasing the number of particles and layers beyond this demanded long simulation time. In case of using an explicit FEA code, it will be easier to increase the number of the particles and layers to check its effect on the accuracy of the results.
    - Applying multi material coating, using heavy particles such as Fe powder for first layer, and coating with Al powder
    - Changing the size of the particles up to 100 μm along with the change of the shape
    - Applying nano-sized particle and studying their effect on the induced residual stress
    - Applying a combination of shot peening and cold spray coating. First simulating shot peening and then applying cold spray coating.
- Stress-strain response in RBM test for Mg specimen
    - Modeling RBM specimen under 4 point bending and finding the strain/stress responses by using anisotropic model of ANSYS

  - Extending the modeling/calculations to cyclic behaviour
  - Developing a simple model using Variable Material Properties (VMP) method [51] for pure bending of Mg round specimen. Note that loading is purely one dimensional and hence yielding is defined by one point. Cyclic stress-strain curves should be used. This will then be used to check the merits of energy-based fatigue model for Mg alloys.

6.2 Experimental Studies

- Applying more in depth stress measurements to correlate the fatigue life to the residual stress, including:
  - Applying in depth stress measurement on as received, stress relieved and stress relieved/coated round specimens
  - Comparing the stress measurement results to fatigue life of each group
- Study of the effect of corrosion on the fatigue life of AZ31B. This includes:
  - Applying fatigue tests on as received/salt sprayed AZ31B specimens to investigate the effect of corrosion on fatigue strength
  - Applying fatigue tests on as received/coated/salt sprayed and stress relieved/coated/salt sprayed AZ31B specimens to investigate the effect of corrosion on fatigue strength
- Applying fatigue tests on as received/coated AZ31B specimens and preparing S-N curves to check the effect of cold spray coating on the initially existing residual stress
- The case studies of FEA simulation, mentioned in section 6-1, can be checked with experimental works as well.

References

[1] Kainer K.U., Magnesium Alloys and Technologies, WILEY-VCH, 2003

[2] Friedrich, H. E., and Mordike, B. L., Magnesium Technology, Metallurgy, Design Data, Applications, Springer, 2006

[3] Albinmousa J., Jahed H., and Lambert S., “Cyclic Behaviour of Wrought Magnesium Alloy under Multiaxial Load”. International Journal of Fatigue, 33 (8) (2011)1127-1139

[4] Kainer K. U., Magnesium Alloys and their Applications, WILEY-VCH, 2000

[5] Ferrando W.A., Review of Corrosion and Corrosion Control of Magnesium Alloys and Composites, J. Mater. Eng. 11 (1998) 299-313

[6] Champagne, V. K., The Cold Spray Materials Deposition Process, Fundamentals and Applications, Woodhead Publishing Limited, 2007

[7] Papyrin A. N., Cold Spray Technology, Elsevier, 2007

[8] Grujicic M., Saylor J.R., Beasley D.E., DeRosset W.S., and Helfritch D., Computational Analysis of the Interfacial Bonding Between Feed-Powder Particles and the Substrate in the Cold-Gas Dynamic-Spray Process, Applied Surface Science 219 (2003) 211–227

[9] Xian-Jin Ning, Jae-Hoon Jang, Hyung-Jun Kim, Chang-Jiu Li, and Changhee Lee, Cold Spraying of Al–Sn Binary Alloy: Coating Characteristics and Particle Bonding Features, Surface & Coatings Technology 202 (2008) 1681–1687

[10] C.-J. Li, W.-Y. Li, and Y.-Y. Wang, Effect of Spray Angle on Deposition Characteristics in Cold Spraying, ASM International, Material Park, Ohio, 2003

[11] Assadi H., Gartner F., Stoltenhoff T., and Kreye H., Bonding Mechanism in Cold Gas Spraying, Acta Materialia 51 (2003) 4379–4394

[12] Wen-Ya Li, and Wei Gao, Some Aspects on 3D Numerical Modeling of High Velocity Impact of Particles in Cold Spraying by Explicit Finite Element Analysis, Applied Surface Science 255 (2009) 7878–7892

[13] KeeHyun Kim, Makoto Watanabe, and Seiji Kuroda, Bonding Mechanisms of Thermally Softened Metallic Powder Particles and Substrates Impacted at High Velocity, Surface & Coatings Technology 204 (2010) 2175–2180

[14] Morgan R., Fox P., Pattison J., Sutcliffe C., and O’Neill W., Analysis of Cold Gas Dynamically Sprayed Aluminum Deposits, Materials Letters 58 (2004) 1317– 1320

[15] Zhang D., Shipway P.H., and McCartney D.G., Cold Gas Dynamic Spraying of Aluminum: The Role of Substrate Characteristics in Deposit Formation, ASM International, 2004

[16] S Kumar, Gyuyeol Bae, Kicheol Kang, Sanghoon Yoon and Changhee Lee, Effect of Powder State on the Deposition Behaviour and Coating Development in Kinetic Spray Process, JOURNAL OF PHYSICS D: APPLIED PHYSICS 42 (2009) 075305 (8pp)

[17] Peter C. King, and Mahnaz Jahedi, Relationship between Particle Size and Deformation in the Cold Spray Process, Applied Surface Science 256 (2010) 1735–1738

[18] Xian-Jin Ning, Jae-Hoon Jang, and Hyung-Jun Kim, The Effects of Powder Properties on In-Flight Particle Velocity and Deposition Process During Low Pressure Cold Spray Process, Applied Surface Science 253 (2007) 7449–7455

[19] Guechichi H., These de doctoral, ENSAM Paris, 1986

[20] Khabou M. T., Castex L., and Inglebert G., The Effect of Material Behaviour Law on the Theoretical Shot Peening Results, European Journal of Mechanics, Eur. J. Mech., A/Solids 9: 537-549.

[21] Fathallah R., Inglebert G., and Castex L., Modelling of Shot Peening Residual Stresses and Plastic Deformation Induced in Metallic Parts, Ecole National Superieure d'Art et Metiers, 1996

[22] Al-Hassani, S. T. S., An Engineering Approach to Shot Peening Mechanics, Proc. Of the second Int. Conf. On Shot Peening, ICSP-2 (H. O. Fuchs ed.). Paramus, NJ: ASPS, p275.

[23] Meguid S.A., Shagal G., Stranart J.C., and Daly J., Three-Dimensional Dynamic Finite Element Analysis of Shot-Peening Induced Residual Stresses, Finite Elements in Analysis and Design 31 (1999) 179-191

[24] Schwarzer J., Schulze V., and Vohringer O., Finite Element Simulation of Shot Peening - A Method to Evaluate the Influence of Peening Parameters on Surface Characteristics, Institut fur Werkstoffkunde I, Univessity of Karlsruhe (TH), Karlsruhe, Germany

[25] Majzoobi G.H., Azizi R., and Alavi Nia A., A Three-Dimensional Simulation of Shot Peening Process Using Multiple Shot Impacts, Journal of Materials Processing Technology 164–165 (2005) 1226–1234

[26] Meo M., and Vignjevic R., Finite Element Analysis of Residual Stress Induced by Shot Peening Process, Advances in Engineering Software 34 (2003) 569–575

[27] Frija M., Hassine T., Fathallah R., Bouraoui C., and Dogui A., Finite Element Modelling of Shot Peening Process: Prediction of the Compressive Residual Stresses, the Plastic Deformations and the Surface Integrity, Materials Science and Engineering A 426 (2006) 173–180

[28] K. Schiffner, C. Droste gen. Helling, Simulation of Residual Stresses by Shot Peening, Computers and Structures 72 (1999) 329-340

[29] Guagliano M., Relating Almen Intensity to Residual Stresses Induced by Shot Peening: A Numerical Approach, Journal of Materials Processing Technology 110 (2001) 277-286

[30] Kobayashi M., Matsui T., and Murakami Y., Mechanism of Creation of Compressive Residual Stress by Shot Peening, Int. J. Fatigue Vol. 20, No. 5 (1998) 351–357

[31] Thanh-Duoc Phan, Syed Masood, Mahnaz Jahedi, and Saden Zahiri, Residual Stresses in Cold Spray Process Using Finite Element Analysis, Trans Tech Publications, Switzerland, 2010

[32] Choi W.B., Li L., Luzin V., Neiser R., Gna¨upel-Herold T., Prask H.J., Sampath S., and Gouldstone A., Integrated Characterization of Cold Sprayed Aluminum Coatings, Acta Materialia 55 (2007) 857–866

[33] McCune R.C., Donlon W.T., Popoola O.O., and Cartwright E.L., Characterization of Copper Layers Produced by Cold Gas-Dynamic Spraying, ASM International, 1999

[34] Zhang P., and Lindemann J., Influence of Shot Peening on High Cycle Fatigue Properties of the High-Strength Wrought Magnesium Alloy AZ80, Scripta Materialia 52 (2005) 485–490

[35] Dorr T., Hilpert M., Beckmerhagen P., Kiefer A., and Wagner L., Influence of Shot Peening on Fatigue Performance of High Strength Aluminum and Magnesium Alloys, The 7th International Conference on Shot Peening, Institute of Precision Mechanics, Warsaw, Poland, 1999

[36] Wagner L., Mechanical Surface Treatments on Titanium, Aluminum and Magnesium Alloys, Materials Science and Engineering A263 (1999) 210–216

[37] Hilpert M., and Wagner L., Effect of Mechanical Surface Treatment and Environment on Fatigue of Wrought Magnesium Alloys, Magnesium Alloys and their Applications. Edited by K. U. Kainer, WILEY-VCH, 2000, pg 463-468

[38] Zinn W., and Scholtes B., Mechanical Surface Treatments of Lightweight Materials-Effects on Fatigue Strength and Near-Surface Microstructures, ASM International, JMEPEG (1999) 8:145-151

[39] Price T.S., Shipway P.H., and McCartney D.G., Effect of Cold Spray Deposition of a Titanium Coating on Fatigue Behaviour of a Titanium Alloy, ASM International, JTTEE5 15 (2006) 507-512

[40] Sansoucy E., Kim G.E., Moran A.L., and Jodoin B., Mechanical Characteristics of Al-Co-Ce Coatings Introduced by the Cold Spray Process, ASM International, JTTEE5 16 (2007) 651–660

[41] Jeong C. Y., and Ha S., Fatigue properties of Al–Si Casting Alloy with Cold Sprayed Al/SiC Coating, International Journal of Cast Metals Research,VOL 21 NO 1–4, 2008

[42] Dindorf C., and Müller C., Corrosion and Fatigue Behaviour of the Magnesium Die-Cast Alloy AZ91 hp after Surface Treatment, Proceedings of the 6th International Conference Magnesium Alloys and Their Applications, Edited by K.U. Kainer, WILEY-VCH, 2004, pg. 574-579

[43] Mayer H., Stich A., Zettl B., and Haldenwanger H.G., High Cycle Fatigue of Magnesium Alloys, Proceedings of the 6th International Conference Magnesium Alloys and Their Applications, Edited by K.U. Kainer, WILEY-VCH, 2004, pg. 444-449

[44] ANSYS User's Guide, Version 11.0, ANSYS Inc.

[45] ASM Metals Handbook, 9th Edition, 1989, Vol. 2

[46] Abaqus Analysis User's Manual, Vol. III, Version 6.7, Dassault Systems, 2007

[47] LS-DYNA Theory Manual, Livermore Software Technology Corporation, 2006

[48[J. Almen, J.P.H. Black, Residual Stresses and Fatigue in Metals, McGraw-Hill, Toronto, 1963, pp. 64-69

[49] Anon., Shot Peening of Metal Parts, Military Speci®cation Mil-S-13165c, 1989

[50] Stephens R. I., Fatemi A., Stephens R. R., Fuchs H. O., Metal Fatigue In Engineering John Wiley & Sons Inc., 2001

[51] Jahed, H., and Dubey, R. N., 1997, ‘‘An Axisymmetric Method of Elastic-Plastic Analysis Capable of Predicting Residual Stress Field,’’ ASME J. Pressure Vessel Technol., 119, pp. 264–273

[52] Instron User's manual